BIOMEDICAL AND ATMOSPHERIC APPLICATIONS OF OPTICAL SPECTROSCOPY IN SCATTERING MEDIA

Johannes Swartling

Doctoral Thesis
Department of Physics
Lund Institute of Technology
November 2002

Printed at KFS AB, Lund, Sweden

November 2002

Lund Report on Atomic Physcs, LRAP-290

ISSN 0281-2162

LUTD2(TFAF-1050)1-113(2002)

ISBN 91-628-5486-0

Till Anette

Contents

Abstract

Spectroscopic analysis of scattering media is difficult because the effective path length of the light is non-trivial to predict when photons are scattered many times. The main area of research for such conditions is biological tissues, which scatter light because of variations of the refractive index on the cellular level. In order to analyze tissues to diagnose diseases, or predict doses during, for example, laser treatment, it is necessary to be able to model light propagation in the tissue, as well as quantify the scattering and absorption properties. Problems of this type occur in many other areas as well, for example in material science, and atmospheric and ocean-water optics.

This thesis deals with light propagation models in scattering media, primarily based on radiative transport theory. Special attention has been directed to the Monte Carlo model to solve the Boltzmann radiative transport equation, and to develop faster and more efficient computer methods. A Monte Carlo model was applied to solve a spectroscopic problem in monitoring the emission of gases in smoke plumes. An important theme in the thesis deals with measurement of the optical properties, with emphasis on biomedical applications. Several different measurement techniques based on a wide range of instruments have been developed or improved upon, and the strengths and weaknesses of these methods have been evaluated.

The measurement techniques have been applied to analyze the scattering and absorption properties of some biological tissues. Much devotion has been directed to optical characterization of blood, which is an important tissue from a health-care perspective. At present, the complex scattering properties of blood prevents detailed optical analysis of whole blood. The work presented here is also aimed at acquiring a better understanding of the fundamental scattering processes at a cellular level.

List of papers

This thesis is based on the following papers:

Paper I. J. Swartling, A. Pifferi, A. M. K. Enejder, and S. Andersson-Engels, "Accelerated Monte Carlo model to simulate fluorescence spectra from layered tissues," Journal of the Optical Society of America A, in press (2002).

Paper II. J. Swartling, J. S. Dam, and S. Andersson-Engels, "Comparison of spatially and temporally resolved diffuse reflectance measurement systems for determination of biomedical optical properties," submitted to Applied Optics (2002).

Paper III. J. Swartling, A. Pifferi, E. Giambattistelli, E. Chikoidze, A. Torricelli, P. Taroni, M. Andersson, A. Nilsson, and S. Andersson-Engels, "Measurements of absorption and scattering properties using time-resolved diffuse spectroscopy – Instrument characterization and impact of heterogeneity in breast tissue," manuscript (2002).

Paper IV. J. Swartling, S. Pålsson, P. Platonov, S. B. Olsson, and S. Andersson-Engels, "Changes in tissue optical properties due to radio-frequency ablation of myocardium," submitted to Medical & Biological Engineering & Computing (2002).

Paper V. A. M. K. Enejder, J. Swartling, P. Aruna, and S. Andersson-Engels, "Influence of cell shape and aggregate formation on the optical properties of flowing whole blood," Applied Optics, returned after minor revisions (2002).

Paper VI. J. Swartling, A. M. K. Enejder, P. Aruna, and S. Andersson-Engels, "Polarization-dependent scattering properties of flowing whole blood," manuscript for Applied Optics (2002).

Paper VII. P. Weibring, J. Swartling, H. Edner, S. Svanberg, T. Caltabiano, D. Condarelli, G. Cecchi, and L. Pantani, "Optical monitoring of volanic sulphur dioxide emissions – Comparison between four different remote-sensing spectroscopic techniques," Optics and Lasers in Engineering 37, 267-284 (2002).

Additional material has been presented in:

1. S. Andersson-Engels, A. M. K. Enejder, J. Swartling, and A. Pifferi, "Accelerated Monte Carlo models to simulate fluorescence of layered tissue," *Photon Migration, Diffuse Spectroscopy, and Optical Coherence Tomography: Imaging and Functional Assessment*, S. Andersson-Engels, J.G. Fujimoto, Eds. Proceedings of SPIE Vol. 4160, 14-15 (2000).

2. J. Swartling, P. Aruna, A. M. K. Enejder, and S. Andersson-Engels, "Optical properties of flowing bovine blood in vitro," *Optical Techniques and Instrumentation for the Measurement of Blood Composition, Structure and Dynamics In vitro and In vivo*. CLEO/Europe 2000, Conference Digest p. 354 (2000).

3. J. Swartling, C. af Klinteberg, J. S. Dam, and S. Andersson-Engels, "Comparison of three systems for determination of optical properties of tissue at 785 nm," European Conferences on Biomedical Optics (2001).

4. J. Swartling and S. Andersson-Engels, "Optical mammography - a new method for breast cancer detection using ultra-short laser pulses," DOPS-NYT 4, 19-21 (2001).

5. J. Swartling, S. Andersson-Engels, A. M. K. Enejder, and A. Pifferi, "Accelerated reverse-path Monte Carlo model to simulate fluorescence in layered tissue," in OSA Biomedical Topical Meetings, OSA Technical Digest, 615-617 (2002).

6. J. Swartling, S. Pålsson, and S. Andersson-Engels, "Analysis of the spectral shape of the optical properties of heart tissue in connection with myocardial RF ablation therapy in the visible and NIR region," in OSA Biomedical Topical Meetings, OSA Technical Digest, 607-609 (2002).

7. M. Ozolinsh, I. Lacis, R. Paeglis, A. Sternberg, S. Svanberg, S. Andersson-Engels, and J. Swartling, "Electrooptic PLZT ceramics devices for vision science applications," Ferroelectrics 273**,** 131-136 (2002).

8. M. Soto Thompson, J. Swartling, S. Andersson-Engels, S. Pålsson, X. Zhao, “Dosimetry and fluence rate calculations for fiber-guided interstitial photodynamic therapy: tissue phantom measurements and theoretical modeling,” BiOS 2003, San Jose (Accepted).

1. Introduction

The concept of spectroscopic analysis of materials is of profound importance in science and technology. In traditional spectroscopy, the presence of a substance can be detected and quantified by means of its spectral signature – wavelength bands in which light is absorbed (or emitted), defined by the electronic energy levels of the atoms and molecules that constitute the substance. Measurements of this kind are performed routinely in thousands every day, to the benefit of the medical services, to industry and as a tool in basic research to promote the advancement of our understanding of nature.

The conventional spectroscopic measurement requires that the material is optically clear. A simple definition of a clear material is that the refractive index is constant on spatial scales ranging from microscopic, in the order of the wavelength of the light, up to macroscopic. Any spatial variation in the refractive index within this range will scatter light in a beam into new directions. To obtain quantitative information from spectroscopy, it is necessary to know the path-length of the light beam through the medium. If the scattering of light is severe, the path-length no longer represents the shortest distance from the light source to the spectrometer through the medium, but a longer one, which is not trivial to predict. Light scatters to some extent in all media, but in many cases the effect is so small that it may be neglected. In an intermediate regime, the scattering may be significant, but still small enough so that the assumption of a clear medium can be used with suitable corrections. One of the main objectives of this thesis is to deal with the prediction of the light path-length through media where the scattering is so strong that such corrections are no longer valid.

There is no clear delineation where the weakly scattering regime stops and the strongly scattering regime starts – it depends on the problem. Often, one talks about multiple scattering. If light is regarded as photons, multiple scattering occurs when there is a large probability that any given photon in a beam will scatter more than once. Then it is evident that a strongly scattering medium is characterized by two things: the probability of scattering, and the dimensions of the medium. For example, a piece of paper has a very high probability of scattering, and scatters light strongly even though its physical dimensions are small. On the other hand, the probability of scattering in the atmosphere is comparably low, but taken over several kilometers, the scattering of a light beam may still be significant. Another objective of this thesis is to show that the same models and principles may be applied to very small geometries, such as sheets of paper, and very large ones, such as atmospheric measurements.

Examples of strongly scattering media that are interesting from a spectroscopic point of view include the already mentioned paper and atmosphere, ocean water, a

large number of solid materials around us, and most biological tissues. Since the invention of the laser in the 1960s, and its rapid adoption by the medical community, tissue optics has been the major field of research where strongly scattering media have been studied. In the study of tissue optics, the third main objective of this thesis becomes clear: the scattering of a material is not only a nuisance in spectroscopic measurements. By analyzing the scattering properties, important information of the material may be obtained. Thus, the scattering itself becomes an object of analysis rather than just a parameter to be controlled.

Although research in tissue optics took off during the 1970s, it is of historical interest to note that much of the fundamental theory was developed earlier, in other branches of physics. As will be described in this thesis, light scattering is usually modeled from a starting point of either of two theories: wave theory (Maxwell's equations) or transport theory. Much of the theory of scattering from single particles using wave theory was developed in the early years of the 20th century. Transport theory originates from the late 19th century, but the development was accelerated with the need to model neutron transport in nuclear reactors. Much of the relevant literature and computer code used for light propagation was inherited by research in neutron transport.

In medical applications of light and lasers, the whole range of important issues of light propagation in scattering media is demonstrated. A fundamental categorization is the forward problem and the inverse problem. The forward problem is, given that the optical properties of the medium are known, to predict how light will propagate through the medium. The practical importance of this in medical applications is mainly in therapy, for example to calculate the dose in a laser treatment. The inverse problem is, given that light that has penetrated the tissue is measured, to deduce what the optical properties inside the medium are. The practical importance here is mainly in diagnostics, since both the absorption properties – the traditional spectroscopic signal – and the scattering properties carry information on the state of the tissue. The other important aspect of the inverse problem is to provide input data for calculations of the forward problem. However, as will be seen, it is not possible to solve the inverse problem without first solving the forward problem.

This thesis concerns models of light propagation in scattering media, with the emphasis on transport theory. Specifically, the Monte Carlo method was used extensively in Papers I and VII. Measurement of the optical properties is another major part of the thesis, and Papers II – VI are devoted to this problem. Most work has been done within the framework of potential practical applications, primarily in medicine (Papers I – VI) but also in environmental monitoring (Paper VII).

2. Formulation of the problems

From a very general perspective, consider Fig. 2.1. A turbid medium, delineated by a boundary, is illuminated from the outside, or by light sources from inside, with light $X_{in}(\mathbf{r},\mathbf{s},t)$. The denotation X represents some suitable radiometric quantity, $\mathbf{r}$ represents the spatial coordinates, $\mathbf{s}$ is a direction and t time. For simplicity the light is assumed monochromatic. The medium has optical properties denoted $\mathbf{p}(\mathbf{r})$, for the moment disregarding their physical origin. It is usually assumed that $\mathbf{p}(\mathbf{r})$ is quasi-constant in time, i.e., any changes in the optical properties occur on a longer time scale than the propagation of light. Light that either propagates through the medium or has emerged is denoted $X_{prop}(\mathbf{r},\mathbf{s},t)$.

The Forward Problem

The first task is to find a way to predict $X_{prop}(\mathbf{r},\mathbf{s},t)$, given that we know $\mathbf{p}(\mathbf{r})$. Thus, we want to find the transfer function f:

$$\mathrm{f}[X_{in}(\mathbf{r},\mathbf{s},t);\mathbf{p}(\mathbf{r})] \rightarrow X_{prop}(\mathbf{r},\mathbf{s},t) \tag{2.1}$$

The Inverse Problem

The next task is to find a way to deduce $\mathbf{p}(\mathbf{r})$, given that we have measured $X_{prop}(\mathbf{r},\mathbf{s},t)$, or some part of it. This means finding the inverse to the above:

$$\mathrm{f}^{-1}[X_{in}(\mathbf{r},\mathbf{s},t);X_{prop}(\mathbf{r},\mathbf{s},t)] \rightarrow \mathbf{p}(\mathbf{r}) \tag{2.2}$$

These problems comprise the fundamental questions posed in this thesis. In order to solve the forward and the inverse problem for a turbid medium, a number of physical theories, assumptions and approximations are needed. In the next chapter, the forward problem will be discussed, followed by the inverse problem in Chapter 4. To conclude, some practical aspects concerning tissue optics, instrumentation issues, and applications are discussed in Chapter 5.

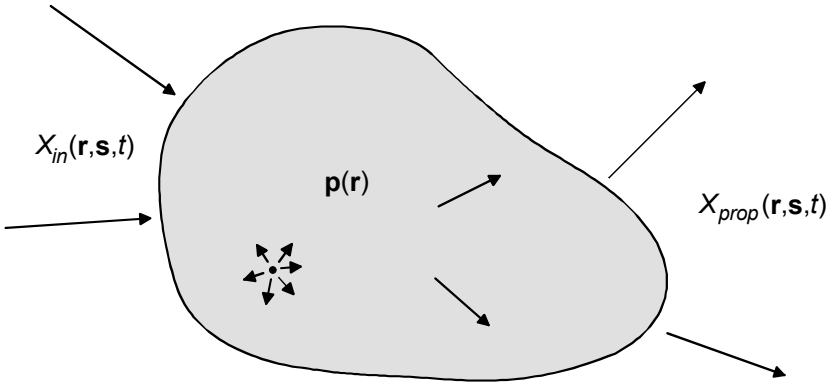

Fig. 2.1 The geometry of light propagation in a turbid medium, in general terms. The medium is delineated by a boundary, and it is illuminated by light represented by $X_{in}(\mathbf{r},\mathbf{s},t)$. The light that propagates through the medium, or has emerged, is denoted $X_{prop}(\mathbf{r},\mathbf{s},t)$. The optical properties are denoted $\mathbf{p}(\mathbf{r})$.

3. The forward problem – light propagation models

The definition of the optical properties $\mathbf{p}(\mathbf{r})$ in Fig. 2.1 depends on the physical theory one chooses to describe the light propagation. As mentioned in the introduction, either of two physical theories of light is considered: wave theory or transport theory. Wave theory, or electromagnetic wave theory, relies on solutions of the Maxwell equations. In this context, the optical properties are defined by the complex dielectric constant, $\varepsilon(\mathbf{r})$. The variation in $\mathrm{Re}\{\varepsilon(\mathbf{r})\}$ describes the scattering, while $\mathrm{Im}\{\varepsilon(\mathbf{r})\}$ represents the absorption properties. Only in special cases is it possible to solve the wave equation for large macroscopic problems, as will be discussed later. In most problems, especially those related to tissue optics, it is intractable both to solve the wave equation and to cope with the vast complexity of the variation of $\varepsilon(\mathbf{r})$ on a microscopic level. To deal with such problems, the transport theory of radiative transfer is better suited. In transport theory, light is heuristically regarded as energy propagating according to the rules defined by the transport equation, a conceptually simple equation of conservation. The optical properties $\mathbf{p}(\mathbf{r})$ are defined by means of a scattering coefficient, an absorption coefficient and a scattering phase function which relates to the probability of scattering in different directions.

In the next sections, some relevant parts of electromagnetic wave theory, transport theory and their relation will be described. Because of the vast number of publications on the basic theory of these subjects already available, the following treatment will focus on the use of the models rather than full theoretical derivations.

3.1 Electromagnetic wave theory

Maxwell's equations form the starting point of the description of light propagation as electromagnetic waves propagating through a dielectric medium. The fields are classically described by:

$$\nabla \times \mathbf{E} = -\frac{\partial \mathbf{B}}{\partial t} \tag{3.1}$$

$$\nabla \times \mathbf{H} = \frac{\partial \mathbf{D}}{\partial t} + \mathbf{F} \tag{3.2}$$

$$\nabla \cdot \mathbf{D} = \rho \tag{3.3}$$

$$\nabla \cdot \mathbf{B} = 0 \tag{3.4}$$

where **E** [Vm^{-1}] and **H** [Am^{-1}] are electric and magnetic field vectors, **B** [Vsm^{-2}] is the magnetic flux density vector, **D** [Asm^{-2}] is the electric displacement vector, **F** [Am^{-2}] is the current density vector (the conventional notation **J** is in this thesis reserved for the radiometric quantity radiant flux density, see Eq. (3.8) – (3.11)), and ρ [Asm^{-3}] is the volume charge density. The electric and magnetic fields can be related to the displacement field and flux density fields by constitutive relations, depending on the properties of the medium. In a non-dispersive isotropic medium, which we are interested in here, the relations are $\mathbf{D} = \varepsilon\mathbf{E}$ and $\mathbf{B} = \mu\mathbf{H}$, where ε [$AsV^{-1}m^{-1}$] is the permittivity and μ [$VsA^{-1}m^{-1}$] is the permeability. The current density and the electric field are also coupled by $\mathbf{F} = \sigma\mathbf{E}$, where σ [$AV^{-1}m^{-1}$] is the conductivity.

The Maxwell equations can be solved directly using numerical methods, which will be discussed below. The computations for large problems are daunting, however, and clever use of expansion methods and approximations can greatly reduce the calculations needed for some problems. Typically, it is assumed that the medium is nonconductive, and one can then derive the vector wave equations (or Helmholtz equations)[1]:

$$\nabla^2\mathbf{E} + k^2\mathbf{E} = 0 \tag{3.5}$$

$$\nabla^2\mathbf{H} + k^2\mathbf{H} = 0 \tag{3.6}$$

where $k = 2\pi/\lambda$ is the wavenumber (λ is the wavelength).

Often, one is interested in prediction of the scattering from single particles, both because many scattering media in fact consist of ensembles of particles, and also because sometimes it is possible to assume that a scattering medium may be approximated by scattering particles. Scattering from particles can be described in terms of diffraction[2,3] or approximations such as those presented by Rayleigh-Gans-Debye[2-4], but more general approaches are given by Mie theory and T-matrix theory. Mie theory deals with spherical particles, while T-matrix theory is applicable to particles of arbitrary shape, although in practice only particles of spheroidal symmetry are useful. The general idea in Mie and T-matrix theory is to expand the fields in vector spherical functions.

3.1.1 Models for single scattering based on electromagnetic wave theory

Mie theory (or Lorenz-Mie theory) provides a quick and relatively simple way of calculating light scattering[2,3]. The relevant input parameters to a Mie calculation are the ratio of the refractive index inside the particle to that in the surrounding medium, $m = n_{particle}/n_{medium}$, and the size parameter $x = 2\pi a/\lambda$, where a is the

radius of the particle. The result of a Mie calculation is a map of the scattered field from an incident plane wave. Usually, one is interested in the extinction cross section C_{ext} [m^2], scattering cross section C_{sca} [m^2], and the absorption cross section C_{abs} [m^2] of the particle. These can be obtained through integration of the scattered field, and are related as $C_{ext} = C_{sca} + C_{abs}$. It is also convenient to define relative extinction, scattering and absorption cross sections, Q_{ext}, Q_{sca} and Q_{abs} (dimensionless). The relative scattering cross section is defined as $Q_{sca} = C_{sca}/\pi a^2$, and the others analogously. Another property of interest is the scattering anisotropy factor, $g = \langle\cos\theta\rangle$, where θ is the scattering angle. The anisotropy factor is a measure of how close to isotropic the scattering is. For entirely isotropic scattering, such as Rayleigh scattering, $g = 0$. In this context it can also be noted that Mie theory collapses to the classical Rayleigh expression for scattering when $x \to 0$ (cf. Eq. 5.6).

The applicability of Mie theory on a problem depends on several factors. Particles that are spherical by nature are of course prime candidates. Examples of this kind are liquid aerosols such as water droplets. Particles of irregular shape can also be modeled successfully using Mie theory under certain conditions. Several studies have shown that in an ensemble of randomly oriented particles of nonspherical shape, the average scattering can often be represented by Mie theory of spheres of equivalent size. However, this is not always the case, as some authors have pointed out[5]. Mie theory is also important for validation purposes. Instruments designed to measure the scattering of a medium can be tested on samples with microspheres with known size and refractive index, to serve as a verification against theory. This is discussed in more detail in Sect. 5.2. Finally, Mie calculations are useful to provide quick and approximate results when only order-of-magnitude numbers are needed for media that consist of irregular scattering structures.

Mie calculation is not entirely trivial, and the computations are susceptible to round-off errors in the numerical routines. New Mie codes therefore have to be tested thoroughly. For this reason, it is usually best to try to find an existing, well-tested program. In this thesis, all Mie calculations were performed using the program by Bohren and Huffman, BHMIE[3]. Mie programs are available on the Internet, also as interactive web scripts[6].

T-matrix theory presents a more general method to calculate scattering from particles of other shapes than spherical[5,7]. In principle, any shape is possible, but due to the fact that the field vector expansion is based on vector spherical functions, spheroidal particles are best suited. The calculations are even more sensitive to round-off errors than Mie theory, especially as the size parameter increases. For practical purposes, only particles of some spherical symmetry are possible because of this. T-matrix calculations were performed to study the scattering from red blood cells in Paper V. A modified version of the code by

Barber and Hill was used[8,9]. Single-precision (16 digits) T-matrix computations are possible for size parameters $x < 25$, but with extended precision (32 digits) size parameters up to around $x = 65$ are possible with good accuracy[10].

3.1.2 Models for multiple scattering based on electromagnetic wave theory

Ensembles of particles are possible to model using Mie or T-matrix theory, as long as the distances between the particles are large. The total scattering coefficient can then easily be calculated, because the individual particles are in the scattering far-field with respect to their neighbors. When the interparticle distances become small, the particles start to influence each other in their near-field, and the assumption of single, independent scatterers breaks down. In some cases, aggregates of a small number of particles are possible to model using Mie or T-matrix theory using a superposition approach[7,11], but for more complicated geometries more general methods are required. The perhaps most straightforward method of solving a wave problem for an arbitrary geometry is by discretizing Maxwell's equations, the spatial coordinates and time. This method is called Finite Difference Time Domain (FDTD), and can in principle solve any problem. However, due to the computational requirements, FDTD is limited to rather small problems. As a rule of thumb, the spatial discretization must be $\lambda/15$ or smaller, which means about 10^6 points for a problem of size 5λ. For each time step, one operation is required for every point in space. More information on FDTD can be found in Refs. 12 and 13. Calculation of light scattering from single biological cells using FDTD has been demonstrated[14-16].

An alternative approach to FDTD is to use the Finite Element Method (FEM) to solve Maxwell's equations. In general, FEM is best suited to solve partial differential equations on closed domains, i.e., boundary value problems. FEM requires the medium to be represented by a mesh, and one of the principal advantages of the method is the versatility of the mesh design and flexibility of representing complicated shapes and variations in dielectric constant. Another advantage of FEM is that the matrices are typically sparse, so that the numerical machinery that pertains to sparse matrix computation can be utilized. A drawback of the method is that special care has to be taken when modeling unbounded domains, to terminate the mesh using the proper boundary conditions. Several commercial and free FEM codes are available, ranging from very simple 2D representations to advanced packages. Examples of free codes are EMAP[17] and Student's QuickField[18], while commercial software packages include FEMLAB (a Matlab toolbox)[19] and EMFLex[20].

A slightly less direct approach is presented by the Method of Moments (MoM). In this method, the problem is reduced to smaller domains, where the Maxwell equations are formulated as integral equations[21]. An example of a free MoM code is PCB-MoM[22].

The methods mentioned so far suffer from being restricted by the computational resources required for problems larger than a few wavelengths. Larger problems, up to a few hundred wavelengths, can be solved using the Fast Multipole Method (FMM)[23]. FMM utilizes an efficient method for numerical convolution of the Green's function for the vector wave equation, which leads to a reduction of the numerical complexity. The method does not inherently involve any approximations, but by utilizing problem-specific properties the computation can be made even more efficient. One such assumption may be that the variation in refractive index in the medium is small. This condition is fulfilled in human blood, which renders FMM a possible candidate for modeling the complex scattering properties of blood (see also Sect. 5.1.9; Optical properties of blood).

To solve even larger problems, approximation methods can be used. The approximation methods are sometimes denoted asymptotic methods, which in turn can be categorized into four classes: approximations of partial differential equations and integrals, geometrical optics, physical optics, and other methods. As an example from the first area, the vector wave equation, which is elliptic, may be approximated by a paraxial equation, which renders the parabolic equation method[24]. This method is suitable for large problems with a clear, preferred direction of propagation. A closely related approach is the Bremmer series method[25].

Geometrical optics is valid when the curvature of the object is large compared with the wavelength, i.e., typically for large objects. The ray trajectories are given by the famous Fermat's principle, stating that the path of a ray is always such that the optical path length is minimized. Geometrical optics problems can be solved using ray tracing software. Physical optics depends on integral representations of the far field, for scatterers that are perfectly conducting. The requirement of large objects holds for physical optics as well. The two methods can be combined with other methods, such as MoM, if smaller objects are involved in the problem. The last category, other methods, includes simple optical models such as ray tracing without a phase front, and Fraunhofer and Fresnel diffraction.

The results from the wave equation can also be used as a starting point for a rigorous, analytical derivation of statistical quantities relevant for multiple scattering problems. This leads to differential or integral equations that, in principle, include all wave effects. However, the solutions are complicated and in practice various approximations are employed. Examples of methods include

Twersky's theory, the diagram method, and the Dyson and Bethe-Salpeter equations. An overview of analytical theory is given by Ishimaru[26]. Twersky's theory has been applied on the problem of light scattering in human blood[27,28] (cf. Sect. 5.1.9; Optical properties of blood). However, the result of Twersky's theory is equations with parametric dependence, where the parameters cannot be easily deduced from considerations of the fundamental geometrical and dielectric properties of the medium. In terms of practicality, the theory is therefore more similar to transport theory, which is the topic of next section.

3.2 Transport theory of radiative transfer

The radiative transport equation (RTE) (or Boltzmann equation) can be stated as

$$\begin{aligned} &\frac{1}{c}\frac{\partial L(\mathbf{r},\mathbf{s},t)}{\partial t} = \\ &= -\mathbf{s}\cdot\nabla L(\mathbf{r},\mathbf{s},t) - (\mu_a + \mu_s)L(\mathbf{r},\mathbf{s},t) + \mu_s \int_{4\pi} L(\mathbf{r},\mathbf{s},t)\,\mathrm{p}(\mathbf{s},\mathbf{s}')\,\mathrm{d}\,\omega(\mathbf{s}) + \mathrm{q}(\mathbf{r},\mathbf{s},t) \end{aligned} \tag{3.7}$$

The RTE is an equation of conservation, describing the change in radiance L in the direction **s** inside a small volume element dV. Thus, the first term on the right hand side describes the losses over the boundary of dV, the next term the losses due to absorption and scattering, the third term the gains due to scattering from other directions into **s**, and the last term gains due to any source q inside dV[29,30]. Defining the remaining designations introduced, starting from the left, we have the light speed in the medium c [m/s], the absorption coefficient μ_a [m^{-1}], the scattering coefficient μ_s [m^{-1}], and the scattering phase function p(**s**,**s**') [-]. The scattering phase function gives the probability of scattering from direction **s**' into direction **s**. In the integral, dω(**s**) denotes an infinitesimal solid angle in the direction **s**.

Classical, and still essential, references on transport theory include the works by Chandrasekhar[31], Case and Zweifel[29], and Ishimaru[26]. A recent treatment, oriented toward tissue optics, is given in Ref. 30.

3.2.1 Radiometric quantities

Before discussing the RTE further, it is useful to define some radiometric quantities and their relationships. The radiant flux density **J** [W/m^2] is defined as the power P transferred through a surface area A:

$$P = \int_A \mathbf{J} \cdot \mathbf{n} \, \mathrm{d}A \,, \tag{3.8}$$

where **n** denotes the normal vector to the surface element dA. The scalar quantity inside the integral, i.e., the power per unit area, is called the irradiance $E(\mathbf{r},t)$ [W/m^2]:

$$E(\mathbf{r},t) = \mathbf{J}(\mathbf{r},t) \cdot \mathbf{n}(\mathbf{r}) \tag{3.9}$$

The intensity $I(\mathbf{r},\mathbf{s},t)$ [W/sr] is defined as the power per unit solid angle. The radiance $L(\mathbf{r},\mathbf{s},t)$ [W/m^{2}sr] is defined as the power per unit solid angle and area. The relationship between **J** and L is given by

$$\mathbf{J}(\mathbf{r},t) = \int_{4\pi} L(\mathbf{r},\mathbf{s},t)\mathbf{s} \, \mathrm{d}\,\omega(\mathbf{s}) \,. \tag{3.10}$$

The hemispherical flux, which is the flux through the area element dA in either direction, is a useful quantity. It is defined as

$$J_{n+}(\mathbf{r},t) = \int_{2\pi} L(\mathbf{r},\mathbf{s},t)(\mathbf{s} \cdot \mathbf{n}) \, \mathrm{d}\,\omega(\mathbf{s}) \,. \tag{3.11}$$

If the hemispherical flux is measured from a surface, it is called the radiant exitance or emittance [W/m^2].

In transport theory, light transport is often regarded as a transport of photons, interpreted as classical particles. Although the RTE does not inherently specify the nature of the transported energy as particles, there are several reasons for this interpretation. Historically, neutron transport was the major field where methods in transport theory were developed. The context is thus suited for a particle interpretation. In addition, in the Monte Carlo method, as will be apparent in Sect. 3.2.10, the particle representation is natural. For these reasons it is convenient to define a photon distribution function N(r,s,t) [m^{-3}sr^{-1}], which is the volume density of photons per unit solid angle. The relationship between the radiometric quantity L and the photon density N is then

$$L(\mathbf{r},\mathbf{s},t) = N(\mathbf{r},\mathbf{s},t)\frac{hc^2}{\lambda}, \tag{3.12}$$

where h is Planck's constant.

Another important quantity is the fluence rate ϕ [W/m^2], which describes the power incident on a volume element per surface area:

$$\phi(\mathbf{r},t) = \int_{4\pi} L(\mathbf{r},\mathbf{s},t)\,\mathrm{d}\,\omega(\mathbf{s})\,. \tag{3.13}$$

The fluence rate is useful since by knowing the absorption in the medium, the absorbed energy W [J/m^3] can be calculated as

$$W(\mathbf{r}) = \mu_a(\mathbf{r})\int \phi(\mathbf{r},t)\,\mathrm{d}\,t\,. \tag{3.14}$$

This equation is important, since it couples the deposited energy – dose – in a medium, to the radiometric quantity fluence rate.

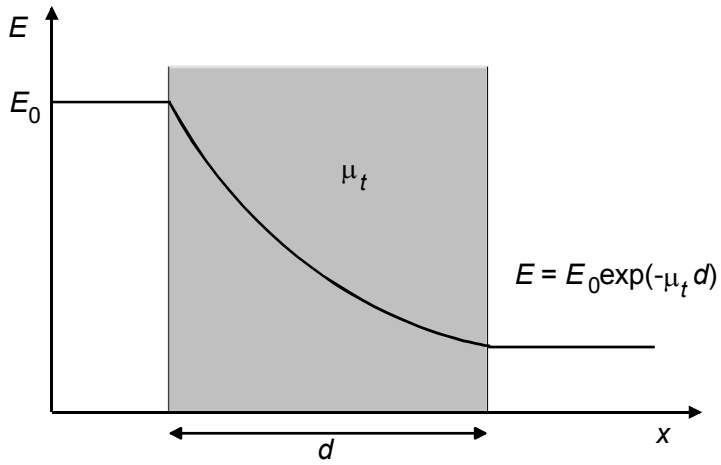

Fig. 3.1 Illustration of Beer-Lambert's law.

3.2.2 Transport properties

Returning to the discussion about the RTE, one identifies four medium-dependent parameters: the light speed c – determined by the refractive index, the absorption and scattering coefficients μ_a and μ_s, and the scattering phase function $p(\mathbf{s},\mathbf{s}')$. The coefficients μ_a and μ_s should be interpreted as the probability of absorption and scattering per unit path length, respectively. Their meaning is clear when considering the generalized Beer-Lambert law,

$$E = E_0 \exp\left[-(\mu_a + \mu_s)d\right], \tag{3.15}$$

which describes the attenuation of a collimated beam (plane wave) of initial irradiance E_0 through a medium of thickness d (see Fig. 3.1). Within the framework of the particle interpretation, the reciprocal of $\mu_a + \mu_s$, $1/(\mu_a + \mu_s)$, is interpreted as the mean free path length between photon interactions with the medium. The quantity $\mu_t \equiv \mu_a + \mu_s$ is called the total attenuation coefficient.

3.2.3 Scattering phase function

The scattering phase function $p(\mathbf{s},\mathbf{s}')$ describes the angular probability of scattering from direction $\mathbf{s}'$ to $\mathbf{s}$. The phase function is sometimes written as $p(\cos\theta)$ to emphasize the angular dependency, and although this is only possible when there is no absolute directional dependency, physically realistic phase functions virtually always only exhibit relative angular dependency. It is usually assumed that the scattering probability is symmetric for the azimuthal angle ψ, although this is not a strict requirement. The phase function is normalized:

$$\int_{-1}^{1} p(\cos\theta)\, d(\cos\theta) = 1 . \tag{3.16}$$

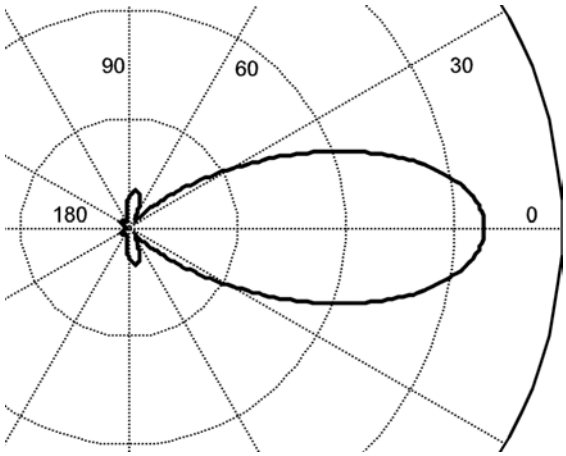

Fig. 3.2 Scattered field from spherical particle calculated with Mie theory. In the calculation, $m = 1.5$, and $x = 2\pi$. The anisotropy factor is $g = 0.58$.

To exemplify the importance of the phase function, consider the scattering from a microscopic sphere, as described by Mie theory (see Fig. 3.2). As a general rule, as the diameter increases the scattering gets increasingly forward-favored. Lobes are

visible in certain angles due to interference effects. In a polydisperse ensemble of particles, the lobes average out and the phase function becomes more or less smooth. The most widely used phase function to approximate this shape is the Henyey-Greenstein phase function[32], which has the functional form

$$p(\cos\theta) = \frac{(1-g^2)}{2(1+g^2-2g\cos\theta)^{3/2}}, \tag{3.17}$$

where g is called the scattering aniostropy factor or simply "g-factor," and is defined as $g = \langle\cos\theta\rangle$. The shape of the Henyey-Greenstein function is shown in Fig. 3.3 for three values of g. The g-factor can be calculated for any phase function, and is a measure of how forward-favored the scattering in the medium is. Other phase functions have also been used in the literature, such as the Reynolds-McCormick phase function (also called Gegenbauer-kernel phase function)[33]. It is also possible to directly incorporate phase functions from Mie or T-matrix computations, which will be discussed more in connection with Monte Carlo simulations (Sect. 3.2.10).

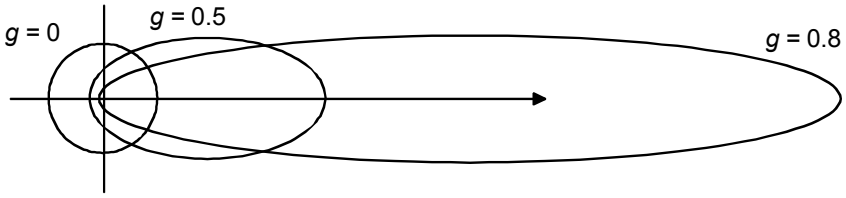

Fig. 3.3 The Henyey-Greenstein phase function for three different values of the scattering anisotropy factor g.

3.2.4 Reciprocity

Before going into the various methods of solving the transport equation, the concept of reciprocity within transport theory will be discussed. Let us, for now, only recognize the fact that many numerical solutions to transport problems start with point-like light sources, and the solution evolves during the computation as a point spreading process. Real light sources are spatially finite, and it may be necessary to convolve this "Dirac response" with the actual spatial shape of the source. In a large class of problems, however, the light source is distributed over a volume, and the detector is almost point-like and may also be directional. This kind of problem may be computationally very inefficient to model in a straightforward

way. The reciprocal situation could then be a much more efficient model, provided that one can show that the two situations are equivalent.

Reciprocity was used in both Papers I and VII, and therefore a more detailed derivation of the reciprocity theorem within transport theory will be presented here. The derivation essentially follows that in Ref. 29. Consider the RTE, Eq. (3.7). The time-dependent RTE can always formally be reduced to a time-independent equation through a Laplace transform[29]. Therefore, we only have to derive the reciprocity theorem for the time-independent RTE:

$$\mathbf{s}\cdot\nabla L(\mathbf{r},\mathbf{s})+(\mu_a+\mu_s)L(\mathbf{r},\mathbf{s})=\mu_s\int_{4\pi}L(\mathbf{r},\mathbf{s}')\,\mathrm{p}(\mathbf{s},\mathbf{s}')\,\mathrm{d}\,\omega(\mathbf{s})+Q(\mathbf{r},\mathbf{s})\,. \tag{3.18}$$

Let $L_1(\mathbf{r},\mathbf{s})$ be the unique solution to Eq. (3.18) for a given source $Q_1(\mathbf{r},\mathbf{s})$ and incident distribution $L_{inc,1}(\rho,\mathbf{s})$ on the surface S of the volume V:

$$\begin{aligned}&\mathbf{s}\cdot\nabla L_1(\mathbf{r},\mathbf{s})+(\mu_a+\mu_s)L_1(\mathbf{r},\mathbf{s})=\mu_s\int_{4\pi}L_1(\mathbf{r},\mathbf{s}')\,\mathrm{p}(\mathbf{s},\mathbf{s}')\,\mathrm{d}\,\omega(\mathbf{s})+Q_1(\mathbf{r},\mathbf{s}),\\ &L_1(\rho,\mathbf{s})=L_{inc,1}(\rho,\mathbf{s}),\ \mathbf{s}\cdot\mathbf{n}<0\,.\end{aligned} \tag{3.19}$$

A unique solution always exists if $\mu_a > 0$. Let $\widetilde{L}_1(\mathbf{r},\mathbf{s})$ be the solution to an RTE identical to (3), except that

$$\mathrm{p}(\mathbf{s},\mathbf{s}')\rightarrow\mathrm{p}(-\mathbf{s}',-\mathbf{s})\,, \tag{3.20}$$

i.e.,

$$\begin{aligned}&\mathbf{s}\cdot\nabla\widetilde{L}_1(\mathbf{r},\mathbf{s})+(\mu_a+\mu_s)\widetilde{L}_1(\mathbf{r},\mathbf{s})=\mu_s\int_{4\pi}\widetilde{L}_1(\mathbf{r},\mathbf{s}')\,\mathrm{p}(-\mathbf{s}',-\mathbf{s})\,\mathrm{d}\,\omega(\mathbf{s})+Q_1(\mathbf{r},\mathbf{s}),\\ &\widetilde{L}_1(\rho,\mathbf{s})=L_{inc,1}(\rho,\mathbf{s}),\ \mathbf{s}\cdot\mathbf{n}<0\,.\end{aligned} \tag{3.21}$$

Now, if the phase function p is invariant under time reversal, we have

$$\mathrm{p}(-\mathbf{s}',-\mathbf{s})=\mathrm{p}(\mathbf{s},\mathbf{s}')\,, \tag{3.22}$$

and it is clear that $\widetilde{L}_1(\mathbf{r},\mathbf{s})=L_1(\mathbf{r},\mathbf{s})$ since they are both unique solutions to the same equation with the same boundary conditions. Furthermore, we can define two solutions $L_2(\mathbf{r},\mathbf{s})$ and $\widetilde{L}_2(\mathbf{r},\mathbf{s})$ in a similar way. Since we are deriving an expression for reciprocity, the quantity we are interested in is $\widetilde{L}_2(\mathbf{r},-\mathbf{s})$. This gives the equation

$$-\mathbf{s}\cdot\nabla\widetilde{L}_2(\mathbf{r},-\mathbf{s})+(\mu_a+\mu_s)\widetilde{L}_2(\mathbf{r},-\mathbf{s})=\mu_s\int_{4\pi}\widetilde{L}_2(\mathbf{r},-\mathbf{s}')\,\mathrm{p}(\mathbf{s}',\mathbf{s})\,\mathrm{d}\,\omega(\mathbf{s})+Q_1(\mathbf{r},-\mathbf{s}),$$
$$\widetilde{L}_2(\rho,-\mathbf{s})=L_{inc,2}(\rho,\mathbf{s}),\ \mathbf{s}\cdot\mathbf{n}>0\,. \tag{3.23}$$

Now, multiply Eq. (3.19) by $\widetilde{L}_2(\mathbf{r},-\mathbf{s})$, and integrate over V and $\mathbf{s}$:

$$\int_V\int_{4\pi}\mathbf{s}\cdot\nabla L_1(\mathbf{r},\mathbf{s})\widetilde{L}_2(\mathbf{r},-\mathbf{s})\,\mathrm{d}\,\omega(\mathbf{s})\,\mathrm{d}V+\int_V\int_{4\pi}(\mu_a+\mu_s)L_1(\mathbf{r},\mathbf{s})\widetilde{L}_2(\mathbf{r},-\mathbf{s})\,\mathrm{d}\,\omega(\mathbf{s})\,\mathrm{d}V=$$
$$\int_V\int_{4\pi}\mu_s\widetilde{L}_2(\mathbf{r},-\mathbf{s})\int_{4\pi}L_1(\mathbf{r},\mathbf{s}')\,\mathrm{p}(\mathbf{s},\mathbf{s}')\,\mathrm{d}\,\omega(\mathbf{s}')\,\mathrm{d}\,\omega(\mathbf{s})\,\mathrm{d}V+\int_V\int_{4\pi}Q_1(\mathbf{r},\mathbf{s})\widetilde{L}_2(\mathbf{r},-\mathbf{s})\,\mathrm{d}\,\omega(\mathbf{s})\,\mathrm{d}V \tag{3.24}$$

Similarly, multiply Eq. (3.23) by $L_1(\mathbf{r},\mathbf{s})$ and integrate over V and $\mathbf{s}$, and subtract from Eq. (3.24). The divergence term can be simplified to a surface integral using Gauss' theorem, and we obtain:

$$2\int_S\int_{4\pi}(\mathbf{s}\cdot\mathbf{n})L_1(\mathbf{r},\mathbf{s})\widetilde{L}_2(\mathbf{r},-\mathbf{s})\,\mathrm{d}\,\omega(\mathbf{s})\,\mathrm{d}S=$$
$$\int_V\int_{4\pi}\left\{Q_1(\mathbf{r},\mathbf{s})\widetilde{L}_2(\mathbf{r},-\mathbf{s})-Q_2(\mathbf{r},-\mathbf{s})L_1(\mathbf{r},\mathbf{s})\right\}\mathrm{d}\,\omega(\mathbf{s})\,\mathrm{d}V+$$
$$\mu_s\int_V\int_{4\pi}\int_{4\pi}\left\{\widetilde{L}_2(\mathbf{r},-\mathbf{s})L_1(\mathbf{r},\mathbf{s}')\,\mathrm{p}(\mathbf{s},\mathbf{s}')-L_1(\mathbf{r},\mathbf{s}')\widetilde{L}_2(\mathbf{r},-\mathbf{s})\,\mathrm{p}(\mathbf{s}',\mathbf{s})\right\}\mathrm{d}\,\omega(\mathbf{s}')\,\mathrm{d}\,\omega(\mathbf{s})dV \tag{3.25}$$

The last term vanishes because we can make the variable transformation $\mathbf{s}\leftrightarrow\mathbf{s}'$. Since we had assumed that p(**s**,**s**') was invariant under time reversal, and thus that $\widetilde{L}_2(\mathbf{r},\mathbf{s})=L_2(\mathbf{r},\mathbf{s})$, we finally obtain

$$2\int_S\int_{4\pi}(\mathbf{s}\cdot\mathbf{n})L_1(\mathbf{r},\mathbf{s})L_2(\mathbf{r},-\mathbf{s})\,\mathrm{d}\,\omega\,\mathrm{d}S=$$
$$\int_V\int_{4\pi}\left\{Q_1(\mathbf{r},\mathbf{s})L_2(\mathbf{r},-\mathbf{s})-Q_2(\mathbf{r},-\mathbf{s})L_1(\mathbf{r},\mathbf{s})\right\}\mathrm{d}\,\omega\,\mathrm{d}V \tag{3.26}$$

Equation (3.26) expresses the reciprocity theorem on integral form.

Proceeding to derive the reciprocity theorem in the case usually encountered in tissue optics, consider the geometry in Fig 3.4. It is clear that Q_1 is an isotropic source inside the volume V:

$$Q_1(\mathbf{r},\mathbf{s})=\frac{P_1}{4\pi}\delta(\mathbf{r}-\mathbf{r}_1)\,. \tag{3.27}$$

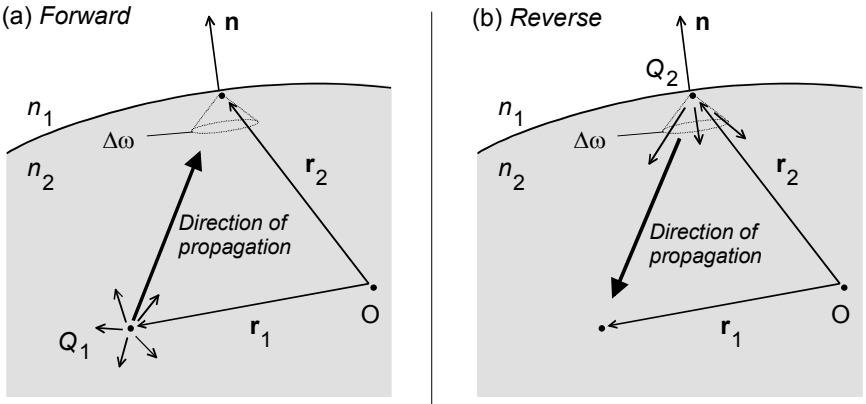

Fig. 3.4 Reciprocity used in tissue optics. The refractive indices outside and inside the medium are denoted n_1 and n_2, respectively. The normal vector at the surface is denoted **n**. In (a), the forward case, we have an isotropic light source Q_1 at $\mathbf{r}_1$ that gives rise to a flux over the boundary at $\mathbf{r}_2$. The radiance at $\mathbf{r}_2$ is integrated over the solid angle $\Delta\omega$, which may be determined by the condition for total reflection, or by the collection angle of a detector at $\mathbf{r}_2$. In (b), the reverse case, a surface source Q_2 at $\mathbf{r}_2$ gives rise to a fluence rate at $\mathbf{r}_1$. The source Q_2 emits in the solid angle $\Delta\omega$.

where P_1 is the power emitted by the source. For the reciprocal case, the definition of the light source is less obvious. Apparently, we could define an incident light on the boundary $L_{inc,1}(\rho,\mathbf{s})$ and let Q_2 be zero. However, it turns out that it is always possible to replace an incident light distribution with an equivalent surface source[29]. This means that the left-hand side of Eq. (3.26) vanishes, and we can define a surface source Q_2 as

$$Q_2(\mathbf{r},\mathbf{s}) = \begin{cases} \dfrac{P_2}{\Delta\omega}(\mathbf{s}\cdot -\mathbf{n})\delta(\mathbf{r}-\mathbf{r}_2)r_F & \text{if } \mathbf{s} \text{ is inside } \Delta\omega \\ 0 & \text{if } \mathbf{s} \text{ is not inside } \Delta\omega \end{cases} \tag{3.28}$$

where P_2 is the emitted power, r_F is a factor that accounts for Fresnel reflection at the interface, and the solid angle $\Delta\omega$ is defined by the critical angle for total reflection at the boundary (or the collection angle of a detector at $\mathbf{r}_2$). In case the refractive indices are equal, $\Delta\omega = 2\pi$. Hence, we get:

$$\frac{P_1}{4\pi}\int_{4\pi} L_2(\mathbf{r}_1,\mathbf{s})\,\mathrm{d}\,\omega(\mathbf{s}) = \frac{P_2}{\Delta\omega}\int_{\Delta\omega} L_1(\mathbf{r}_2,-\mathbf{s})(\mathbf{s}\cdot -\mathbf{n})r_F\,\mathrm{d}\,\omega(\mathbf{s})\,. \tag{3.29}$$

The integral on the left-hand side is exactly the fluence rate at $\mathbf{r}_1$ due to the surface source $Q_2(\mathbf{r},\mathbf{s})$, while the integral on the right-hand side is exactly the radiant flux density at the surface at $\mathbf{r}_2$ due to the isotropic source $Q_1(\mathbf{r},\mathbf{s})$. In practice, we are interested in the case when these two quantities are equal, and we get

$$P_2 = \frac{\Delta\omega}{4\pi} P_1 . \tag{3.30}$$

Thus, to get the same result from two reciprocal computations, the powers of the two reciprocal sources should be scaled according to Eq. (3.30). A more detailed derivation of Eqs. (3.27) – (3.30) is given in Paper I.

As we have seen, the reciprocity theorem is valid under the assumption that the phase function is invariant under time-reversal,

$$\mathrm{p}(-\mathbf{s}',-\mathbf{s}) = \mathrm{p}(\mathbf{s},\mathbf{s}') . \tag{3.31}$$

A natural question is whether there are any physically relevant phase functions that do not exhibit this kind of invariance. Starting with the Henyey-Greenstein phase function, Eq. (3.17), we see that there is no dependence on the direction **s** and thus we are free to make the variable substitution in Eq. (3.31) without violating the equality. The same is true for any phase function computed from Mie theory, which is clear because of the symmetry of spherical particles. For any normal scattering conditions it seems that we can assume that the time-reversal invariance of the phase function holds.

3.2.5 Solving the transport equation

A range of different techniques to solve the RTE are available, each with its advantages and drawbacks. First, we note that no analytical solutions to the RTE are available in 3D, for any geometry other than such that can be represented in one or two dimensions. Full solutions of the RTE are only possible using numerical methods, e.g. by discretization of the equation. The most widely used discretization method is the discrete ordinates method, which will be described in Sect. 3.2.7. The other option is the use of Monte Carlo simulations, a method that has been widely adopted by the tissue optics community.

Instead of attempting a full solution, various methods based on simplifications or approximations are available. Sometimes, the dimensionality of the problem can be reduced. For a few, special, but important geometries, polynomial approximations have been developed. Perhaps the most important approximation is the diffusion

approximation, which is based on the first terms in a spherical harmonics expansion.

In the next few sections, emphasis will be turned to the Monte Carlo simulation method, but most of the other important methods for solving the transport equation will be reviewed or at least be given reference to. As before, the treatment focuses on the practical aspects of the methods rather than derivations, which can be found in the references.

3.2.6 Polynomial approximations

Polynomial approximations have no physical meaning and are not solutions to the RTE *per se*, but they may be useful tools for quick calculations. The idea is to find a polynomial expression describing the optics of the medium using one parameter. A useful example is the total reflectance from a semi-infinite medium, illuminated with diffuse light. This has been found to follow[34]

$$R = \frac{(1-s)(1-0.139s)}{1+1.17s}, \tag{3.32}$$

where

$$s = \sqrt{\frac{1-a}{1-ag}} \tag{3.33}$$

and a is the albedo, $a = \mu_s/(\mu_a+\mu_s)$. The error of prediction has been shown to be less than 0.003 for any combination of μ_s, μ_a and g. More on polynomial approximations can be found in Ref. 34. Approximations for collimated incident light, also for index mismatch between the semi-infinite media, can be found in Ref. 35.

3.2.7 Discretization methods; Adding-Doubling method; Discrete ordinates

As already discussed in connection with the vector wave equations, the most straightforward way of solving complex equations is by direct discretization and subsequent numerical computations. A first step in discretization of the RTE is to discretize the radiance in angular components, $\mathbf{s}_1$, $\mathbf{s}_2$, ...$\mathbf{s}_N$. The equation can then be written as

$$\mathbf{s_i} \cdot \nabla L(\mathbf{r}, \mathbf{s_i}) + \mu_t L(\mathbf{r}, \mathbf{s_i}) = \mu_s \sum_{j=1}^{N} w_j L(\mathbf{r}, \mathbf{s_j}) \, \mathrm{p}(\mathbf{s_i}, \mathbf{s_j}) + Q(\mathbf{r}, \mathbf{s_i}) \,, \tag{3.34}$$

where w_j are weighting factors used in the quadrature. This general approach is called the discrete ordinates method or the *N*-flux method. The simplest way of dealing with this equation is to include only one angular component, the forward direction. In this context the radiance is not a useful quantity since it is defined by means of solid angles. Instead, one must use the irradiance. The RTE is then reduced to

$$\frac{dE(x)}{dx} = -\mu_t E(x) \,, \tag{3.35}$$

which has the solution

$$E(x) = E(x = 0) \exp(-x\mu_t) \tag{3.36}$$

recognized as Beer-Lambert's law.

Increasing complexity slightly, we include two angular components, the forward and the reverse directions. This is the 2-flux, or one-dimensional, transport theory. The one-dimensional transport equation is a set of coupled differential equations:

$$\frac{dE_+(x)}{dx} = -(\mu_{a1} + \sigma) E_+(x) + \sigma E_-(x) \tag{3.37}$$

$$-\frac{dE_-(x)}{dx} = -(\mu_{a1} + \sigma) E_-(x) + \sigma E_+(x) \,. \tag{3.38}$$

Here, $E_+(x)$ propagates in the positive x direction, and $E_-(x)$ in the negative. μ_{a1} is the one-dimensional absorption coefficient, and $\sigma = \mu_{s1}\mathrm{p}(-x,x) = \mu_{s1}\mathrm{p}(x, -x)$, where μ_{s1} is the one-dimensional scattering coefficient. A full derivation of Eqs. (3.37) and (3.38) can be found in Ref. 30. A historically important version of one-dimensional transport theory is given by the Kubelka-Munk theory[36], which assumes diffuse light flux. If the scattering dominates over absorption, one can show that the one-dimensional properties are related to their three-dimensional counterparts by

$$\mu_a = \frac{\mu_{a1}}{2} \,, \tag{3.39}$$

$$\mu_a + \mu_s(1-g) = \frac{2}{3}(\mu_{a1} + 2\sigma)\,. \tag{3.40}$$

Kubelka-Munk theory was used extensively in the early days of tissue optics, and still finds applications. A modern example where Kubelka-Munk theory is used is for rendering skin and other scattering surfaces in computer graphics, such as video games and special effects in motion pictures[37]. Publications of later date testify that the method may still be useful for some applications in tissue optics[38].

The solution to Eqs. (3.37) and (3.38) depends on the boundary conditions. Solutions for various geometries can be found in Refs. 30 and 39.

The next step in complexity for solutions of the RTE is presented by the adding-doubling method, which assumes cylindrical symmetry. The radiance is discretized in terms of cones, defined by $\nu_i = \cos\theta_i$ and $\psi = [0, 2\pi]$. The phase function is rewritten as a redistribution function on matrix form, $\mathbf{h}(\nu_i,\nu_j)$, which describes the probability of scattering from cone ν_i to cone ν_j. The adding-doubling method first assumes that the reflectance $\mathbf{R}(\nu_i,\nu_j)$ and transmittance $\mathbf{T}(\nu_i,\nu_j)$ from a thin, homogeneous, layer of infinite extension are known. By juxtaposing two identical layers and summing the contributions from each, the reflectance and transmittance from a layer twice as thick can be obtained. In this fashion, the reflection and transmission properties of a slab of arbitrary thickness can be calculated. In a similar way, layers of different optical properties can be added together, hence the name adding-doubling.

The adding-doubling scheme consists of integrating discrete reflection and transmission functions. The numerical integration, quadrature, is therefore an important part. Different quadrature schemes are discussed in Ref. 40. Typically between 4 and 32 cones, equal to the number of quadrature points, are used in adding-doubling calculations.

The reflectance and transmittance from the first layer can be calculated in several ways. The most widely used method is diamond initialization, which assumes that the radiance can be approximated by the average of the radiances at the top and bottom of the layer. The requirement for this approximation to be valid is that the layer is optically thin. Furthermore, the RTE is written as time-independent, one-dimensional, and with the angular components discretized according to the cone approach:

$$\nu_i \frac{\partial L(x,\nu_i)}{\partial x} + \mu_t L(x,\nu_i) = \mu_s \sum_{j=1}^{N} w_j \left[h(\nu_i,\nu_j) L(x,\nu_j) + h(\nu_i,-\nu_j) L(x,-\nu_j) \right] \tag{3.41}$$

Solutions of **R** and **T** for diamond initialization can be found in Refs. 40 and 41.

The advantage of the adding-doubling method is that the solutions are accurate for any combination of μ_a, μ_s and g. Index mismatch between layers is also handled correctly. The limitations of the method are that it is restricted to layered geometries and uniform irradiation, that it does not readily give light fluences inside the media, that each layer must be homogeneous, and that the method is not time-resolved. Computer code for adding-doubling calculations, by Prahl, is available for download[42].

Continuing with the discretization approach, the next step would be to solve the RTE for a full 3D geometry with N angular components. A seven-flux method has been used in tissue optics[43]. In this method, the six directions along the axes of a Cartesian coordinate system are used, and a seventh flux along the direction of the incident light beam is introduced. Using only seven angular components is not optimal in terms of obtaining accurate results, and higher numbers of N are needed for truly versatile discrete ordinates models. Extensive development in discrete ordinates has been performed to model neutron transport, but surprisingly little of these results have spilled over to light propagation. One reason for this may be that discrete ordinates computations, up until recently, have required the use of supercomputers to perform within reasonable time limits. Light propagation problems are actually simpler than neutron propagation, because all photons move at a constant speed, which is not the case for neutrons.

The principle of the discrete ordinates method will be sketched briefly. To solve the RTE in a full 3D geometry, the spatial coordinates need to be discretized in addition to the angular directions. The spatial discretization can be done, e.g., using the Crank-Nicolson method[44]. A large number of strategies for discretization have been investigated (see the review in Ref. 45). With these discretizations, the RTE is transformed into a set of coupled integro-differential equations. The next step is to expand the phase function in a series of Legendre polynomials $P_l(\cos\theta)$,

$$\mathrm{p}(\cos\theta) = \sum_{l=0}^{L} \frac{2l+1}{4\pi} b_l P_l(\cos\theta) \,. \tag{3.42}$$

The reader should note that this step is identical to the procedure used when deriving the diffusion approximation, as will be described in Sect. 3.2.8. In general terms, the RTE has now been converted to an equation system that can be written on the form[46]

$$(\mathbf{A} - \mathbf{B})\mathbf{L} = \mathbf{Q} \,, \tag{3.43}$$

where **A** and **B** are discretized versions of the linear operators

$$A = \mathbf{s} \cdot \nabla + \mu_t(\mathbf{r}) , \tag{3.44}$$

$$B = \mu_s \int_{4\pi} p(\mathbf{s}, \mathbf{s}') \, d\omega(\mathbf{s}) \tag{3.45}$$

and **Q** is a source function (cf. Eq. (3.7)). In principle, this can be solved by matrix inversion:

$$\mathbf{L} = (\mathbf{A} - \mathbf{B})^{-1} \mathbf{Q} . \tag{3.46}$$

However, the matrix (**A** – **B**) is computationally very costly to invert, while **A** can be inverted much faster on its own. The discrete ordinates method therefore makes use of an iterative solution strategy:

$$\mathbf{A}\mathbf{L}^{l+1} - \mathbf{B}\mathbf{L}^{l} = \mathbf{Q} . \tag{3.47}$$

Solving for $\mathbf{L}^{l+1}$ we get:

$$\mathbf{L}^{l+1} = \mathbf{A}^{-1}\mathbf{B}\mathbf{L}^{l} + \mathbf{A}^{-1}\mathbf{Q} . \tag{3.48}$$

The operator $\mathbf{A}^{-1}\mathbf{B}$ is known as the iteration operator. Equation (3.48) can be used directly to iterate to the discrete ordinates solution, but for tissue optics problems the so called method of diffusion synthetic acceleration has been employed to accelerate the convergence of the iterations[46,47]. For the n^{th} iteration, the RTE can then be written as

$$\mathbf{s} \cdot \nabla L_n(\mathbf{r}, \mathbf{s}) + \mu_t(\mathbf{r}) L_n(\mathbf{r}, \mathbf{s}) = Q(\mathbf{r}, \mathbf{s}) + \mu_s(\mathbf{r}) \phi_{n-1}(\mathbf{r}) . \tag{3.49}$$

A corrected diffusion equation (cf. Sect. 3.2.8) is introduced as

$$-\nabla \cdot D(\mathbf{r}) \nabla \phi_n(\mathbf{r}) + \mu_a(\mathbf{r}) \phi_n(\mathbf{r}) = Q'(\mathbf{r}) - R_n(\mathbf{r}) , \tag{3.50}$$

where $D = [3(\mu_a + \mu_s(1 - g)]^{-1}$ is the diffusion coefficient, and the correction term R is defined as

$$R_n(\mathbf{r}) = \nabla \cdot \tilde{\mathbf{J}}_n(\mathbf{r}) + \nabla \cdot D(\mathbf{r}) \nabla \tilde{\phi}_n(\mathbf{r}) , \tag{3.51}$$

where $\tilde{\mathbf{J}}_n(\mathbf{r})$ and $\tilde{\phi}_n(\mathbf{r})$ are calculated from L_n using Eqs. (3.10) and (3.13), respectively. The idea behind synthetic acceleration is to split the iteration into two parts, where the corrected diffusion equation, Eq. (3.50), is the inner part. The acceleration is obtained from the fact that the diffusion equation is faster to solve than the entire discretized RTE[46].

The method works as follows: by using ϕ_{n-1} from the previous iteration, Eq. (3.49) is solved for L_n. The correction term R can then be calculated from Eq. (3.51). Next, ϕ_n is calculated using Eq. (3.50), and one cycle is completed. For the first iteration, R is set to zero, and the solution of Eq. (3.50) is identical to the diffusion solution. Thus, after the first iteration, the discrete ordinates method with diffusion synthetic acceleration yields the same result as a Crank-Nicolson (finite difference) solution of the diffusion equation (cf. Eq. (3.54)). The subsequent iterations are improvements of the diffusion solution, which converge toward the full transport solution.

Hielscher *et al*. used the computer code DANTSYS (diffusion accelerated neutral particle transport code system) to perform discrete ordinates computations for light propagation problems[47]. The number of angular components was 168 in these calculations. The model has been further developed for use in optical tomography[48,49]. The computation time of the discrete ordinates method depends on the size of the spatial grid and the number of angular components.

3.2.8 Expansion methods; The diffusion approximation; The P_N-approximation

The next major approach for solving the RTE is by expansion of the radiance in some suitable function series. One way of attacking this problem is by finding the solution, in terms of eigenfunctions, of the homogeneous part of the RTE:

$$\mathbf{s}\cdot\nabla L(\mathbf{r},\mathbf{s})+\mu_t L(\mathbf{r},\mathbf{s})=\mu_s\int_{4\pi}L(\mathbf{r},\mathbf{s})\,\mathrm{p}(\mathbf{s},\mathbf{s}')\,\mathrm{d}\,\mathbf{s}'. \tag{3.52}$$

After finding the eigenfunctions of Eq. (3.52), one can attempt to expand the general solution of the RTE in this function space. This approach has been followed by Case and Zweifel[29], but no practical method based on it seems to have emerged. The reason may be the complexity of the mathematics; the function space turns out not to be a conventional Hilbert space, and the eigenfunctions are distributions in the Schwarz sense. Instead, the expansion method that is almost always used is based on spherical harmonics. This expansion leads to the diffusion approximation, which has several attractive properties, as we will see. The expansion of L is written as

$$L(\mathbf{r},\mathbf{s},t)=\sum_{l=0}^{\infty}\sum_{m=-l}^{l}\sqrt{\frac{2l+1}{4\pi}}L_{lm}(\mathbf{r},t)Y_{lm}(\mathbf{s})\,. \tag{3.53}$$

As always with expansion methods, we have gained an advantage if the quantity of interest, in this case radiance, is well approximated by as few components in the

expansion as possible. Spherical harmonics form a complete orthogonal set of functions on the unit sphere, and are thus suited for problems with spherical symmetry. We can expect that the expansion is very efficient in problems where the radiance propagates more or less uniformly in all directions, i.e., in a diffuse manner. The phase function is handled by expansion in Legendre polynomials (cf. Sect. 3.2.7; The discrete ordinates method). For practical use, the expansion is truncated after N terms. The resulting approximation is called the P_N-approximation. If only the 0th and 1st terms are used, the result is the P_1-approximation. Next, two approximations are assumed: that the light source is isotropic, and that the flux vector **J** is constant in time, and we arrive at the diffusion approximation. The time-resolved diffusion equation is written as

$$\frac{1}{c}\frac{\partial \phi(\mathbf{r},t)}{\partial t} = \nabla D(\mathbf{r})\nabla\phi(\mathbf{r},t) - \mu_a\phi(\mathbf{r},t) + Q(\mathbf{r},t)\,. \tag{3.54}$$

Note that the relevant quantity here is the fluence rate, ϕ. D is called the diffusion coefficient, and is defined as

$$D \equiv \frac{1}{3\left[\mu_a + \mu_s(1-g)\right]} \tag{3.55}$$

The property $\mu_s' \equiv \mu_s(1-g)$ is called the reduced scattering coefficient. Its meaning is schematically illustrated in Fig. 3.5. The diffusion equation generally describes

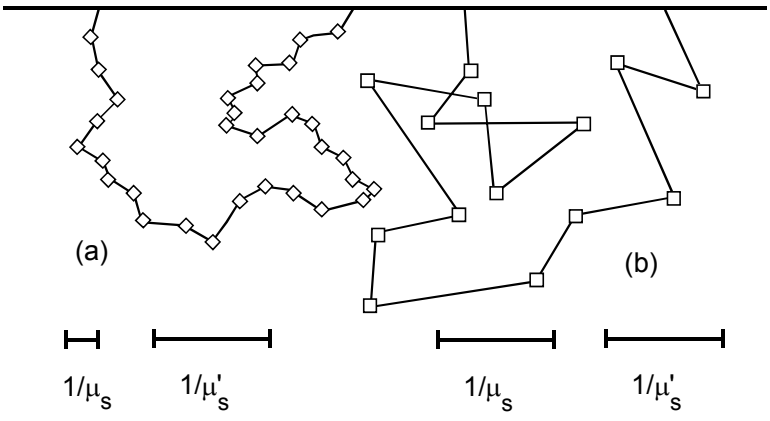

Fig. 3.5 The significance of the reduced scattering coefficient μ_s', illustrated by two photon paths. Path (a) represents a forward-scattering case where $g \approx 0.8$, while in (b) $g = 0$ (isotropic scattering). The reduced scattering coefficients are the same in (a) and (b), since in (a), the scattering can be regarded as isotropic on the scale defined by $1/\mu_s'$.

diffusive processes, and similar equations can be found in various branches of physics, e.g., particle diffusion and heat conduction. The validity of the diffusion equation is restricted by the assumption that the light propagates diffusely, i.e., almost isotropically. This means that the reduced scattering coefficient, μ_s', must be much larger than μ_a, and that ϕ is calculated far away from the light source. These requirements justify the assumption of a time-constant flux vector **J**, which otherwise is clearly erroneous. Instead of assuming that **J** is constant in time, one can assume that **J** is dominated by an exponentially decaying term,

$$\mathbf{J}(\mathbf{r},t) = \exp(-c\lambda t)\,. \tag{3.56}$$

This leads to a different definition of the diffusion coefficient[50]:

$$D' \equiv \frac{1}{3\left[\mu_a + \mu_s' - \lambda\right]} \tag{3.57}$$

The value of λ has been debated in the literature. Yamada[51] and Durduran *et al.*[52] argue that $\lambda = \mu_a$, which means that D' should be independent of the absorption. This was supported by comparison with Monte Carlo simulations. Hielscher *et al.* compared the diffusion solution with the transport solution using the discrete ordinates method[47], and tested various values of λ. The conclusion was that for every combination of μ_s' and μ_a, there is a value of λ that best fits the transport solution, but no single definition of D' fits all situations. In general, however, it seems that Eq. (3.57) with $\lambda = \mu_a$ is more appropriate than Eq. (3.55).

Analytical solutions to the diffusion equation are calculated by means of Green's functions. The solutions obtained are due to point sources, which may seem like an overly simplistic approximation for any real situation. However, since the solutions are only accurate far from the source, and many real light sources illuminate the medium at a small spot, Green's functions directly yield useful results for many practical problems. The boundary conditions must also be considered. If the refractive indices are matched, a physical requirement is that there should be no photon flux back into the turbid medium at the surface, i.e., $J_{n\text{-}}(\rho) = 0$. A good approximation is to introduce a virtual, or extrapolated, boundary, at some distance z_e outside the physical boundary, and there apply the condition $\phi = 0$. For index matching, one can derive the value $z_e = 3 \cdot 0.7104D \approx 2D$ [26]. An index mismatch will change this distance, because of the internal reflection at the boundary[53,54]. For $n = 1.4$, an extrapolated boundary at $z_e \approx 5.5D$ is appropriate. Using this approach, relatively complicated geometries can be handled by the method of images, as exemplified in Fig. 3.6.

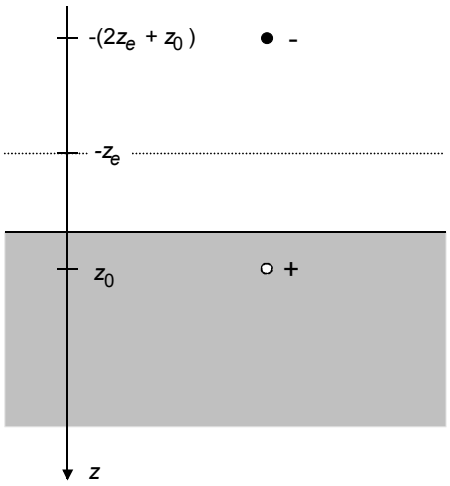

Fig. 3.6 Schematic picture showing the principle of an extrapolated boundary at $-z_e$, where the fluence rate is zero. A dipole source is placed symmetrically around the extrapolated boundary, with the positive part at the point z_0 inside the medium.

Simple solutions for the important case of a semi-infinite homogeneous geometry are easily derived. The time-resolved fluence rate is written as

$$\phi(r,z,t) = \\ = \frac{c}{(4\pi Dct)^{3/2}} \exp(-\mu_a ct)\left\{\exp\left[-\frac{(z-z_0)^2 + r^2}{4Dct}\right] - \exp\left[-\frac{(z+z_0+2z_e)^2 + r^2}{4Dct}\right]\right\} \tag{3.58}$$

where z_0 is the position of the source. For an incident pencil beam, an approximation for the source of $z_0 = 1/\mu_s'$ was proposed by Patterson *et al*[55]. The steady-state solution is

$$\phi(r,z) = \frac{1}{4\pi D}\left(\frac{\exp\left\{-\mu_{eff}\left[(z-z_0)^2 + r^2\right]^{1/2}\right\}}{\left[(z-z_0)^2 + r^2\right]^{1/2}} - \frac{\exp\left\{-\mu_{eff}\left[(z+z_0+2z_e)^2 + r^2\right]^{1/2}\right\}}{\left[(z+z_0+2z_e)^2 + r^2\right]^{1/2}}\right) \tag{3.59}$$

where $\mu_{eff} = [3\mu_a(\mu_a + \mu_s')]^{1/2}$. The reflectance is traditionally calculated by considering the flux across the boundary,

$$R(r,t) = J_{n+}(r, z=0, t) = -D\nabla\phi(r,z,t)\cdot(-\hat{\mathbf{z}})\big|_{z=0} \tag{3.60}$$

which yields

$$R(r,t) = \\ = \frac{1}{2}(4\pi Dc)^{-3/2} t^{-5/2} \exp(-\mu_a ct)\left[z_0 \exp\left(-\frac{r_1^2}{4Dct}\right) + (z_0 + 2z_e)\exp\left(-\frac{r_2^2}{4Dct}\right)\right] \tag{3.61}$$

where $r_1^2 = z_0^2 + r^2$ and $r_2^2 = (z_0 + 2z_e)^2 + r^2$ for the time-resolved case. The corresponding steady-state reflectance is written

$$R(r) = \frac{1}{4\pi}\left[z_0\left(\mu_{eff} + \frac{1}{r_1}\right)\frac{\exp(-\mu_{eff} r_1)}{r_1^2} + (z_0 + 2z_e)\left(\mu_{eff} + \frac{1}{r_2}\right)\frac{\exp(-\mu_{eff} r_2)}{r_2^2}\right] \tag{3.62}$$

Improved expressions for the reflectance can be obtained by instead taking the integral of the radiance over the backward hemisphere. For $n = 1.4$, this leads to the, more accurate, expression for the reflectance[56]:

$$R_{improved}(r,t) = 0.118\phi(r, z=0, t) + 0.306R(r,t) \tag{3.63}$$

Kienle *et al*. have derived a solution for a two-layer geometry, where the upper layer has a finite extension, while the lower layer is infinite[57,58]. Analytical solutions for embedded spheres have also been derived[59]. A comprehensive treatment on various analytical solutions of the diffusion equation is also presented in Ref. 30.

For more complicated geometries, numerical methods are required to solve the diffusion equation. Two methods have been widely used: a finite-differencing method and a finite element method. Finite differencing (cf. Sect. 3.1.1) is a straightforward method, based on discretization of the diffusion equation and the medium. Usually, the Crank-Nicolson method is applied[44]. In three dimensions, the method is called alternating direction implicit (ADI). This method is made efficient by iterating along one spatial coordinate at a time ("operator splitting"), which makes the inversion of the matrices simpler[44,60,61]. The drawback of the ADI method is that the spatial grid is uniformly discretized, which is not optimal for geometries that involve both large homogeneous regions and small complicated inhomogeneities. This problem is solved by FEM, where the mesh spacing can be adapted to be crude for large structures and fine for small structures. General-purpose commercial FEM-packages like the FEMLAB toolbox for Matlab can be

used to solve the diffusion equation. FEM is well suited as a forward model for inverse problems, for other reasons in addition to the versatile mesh, as will be discussed in Sect. 4.5; Optical tomography. Treating boundary conditions is usually not a problem for FEM since the computations always take place on closed domains. FEM has been used by several researchers[62-68].

As an alternative to deriving the diffusion equation for the P_1-approximation, one can derive the telegraph equation in the P_1-approximation[50,69]. The flux **J** is then allowed to vary in time, and the equation includes a second derivative in time. If D is constant, the dependence of **J** vanishes and we have the homogeneous telegraph equation:

$$\frac{3D}{c^2}\frac{\partial^2\phi(\mathbf{r},t)}{\partial t^2}+\frac{1}{c}(3D\mu_a+1)\frac{\partial\phi(\mathbf{r},t)}{\partial t}+\mu_a\phi(\mathbf{r},t)-D\nabla^2\phi(\mathbf{r},t)=S(\mathbf{r},t) \qquad (3.64)$$

The addition from the second derivative term is numerically small, and the result of Eq. (3.64) is very close to the ordinary diffusion equation, Eq. (3.54). A physical interpretation of this is that for diffusive propagation, the variation in **J** is slow compared with the variation in ϕ, which is why one can assume that $\partial\mathbf{J}/\partial t = 0$ when deriving Eq. (3.54).

The P_N-approximation is discussed in Ref. 30 for higher values of N.

3.2.9 Probabilistic methods; Photon migration; Path integrals

A random-walk type approach to treat light propagation in turbid tissue was presented by Bonner *et al.*[70,71]. This model, like the diffusion approximation, assumes isotropic scattering. The method calculates the path-length distributions of photons re-emitted at arbitrary points on the surface. Following the ideas behind this approach, the method of path integrals was introduced[72-74]. This method is based on reformulation of the RTE, to solve for the path probabilities of photon trajectories in a non-absorbing medium. The usual radiometric quantities, such as the radiance, can then be calculated using path integrals along the trajectories.

The term ‘photon migration’ is sometimes used to denote either, or both, of the methods just described, but often it just refers to light propagation in turbid media in general.

3.2.10 The Monte Carlo method

Monte Carlo simulation owes its name to the famous casino, because the method is based on, figuratively speaking, "throwing the dice." The method relies on tracing individual photon trajectories in a random walk fashion, where the scattering and absorption events are governed by the probabilities given by μ_s and μ_a, as well as the phase function $p(\mathbf{s},\mathbf{s}')$. The key decisions to be made in a simulation are the mean free path between scattering events, and the scattering angle. In addition, the absorption of photons must be handled. The method is statistical and requires a large number of photon histories to be computed. The number of photons needed depends on the problem and the wanted accuracy.

Sampling random variables from non-uniform probability distributions is the core of a Monte Carlo simulation. Let us denote a random variable x, which may be the step size s to the next scattering event, or the scattering deflection angle θ. The distribution of x is described by a probability density function $p_p(x)$ over the interval $a \le x \le b$:

$$\int_a^b p_p(x)\,\mathrm{d}x = 1 \tag{3.65}$$

The cumulative distribution function $F_x(x_1)$ describes the probability that $a \le x \le x_1$:

$$F_x(x_1) = \int_a^{x_1} p_p(x)\,\mathrm{d}x \tag{3.66}$$

Computers generate random numbers, here denoted ζ, in the interval [0,1], which are uniformly distributed: $p_p(\zeta) = 1$. The distribution function in this case becomes

$$F_\zeta(\zeta_1) = \int_a^{\zeta_1} p_p(\zeta)\,\mathrm{d}\zeta = \zeta_1 . \tag{3.67}$$

By letting a computer draw ζ, the method of sampling the variable x is to set $F_x(x_1)$ equal to $F_\zeta(\zeta_1)$. The principle is illustrated in Fig. 3.7. This results in the important equation

$$\zeta_1 = \int_a^{x_1} p_p(x)\,\mathrm{d}x , \tag{3.68}$$

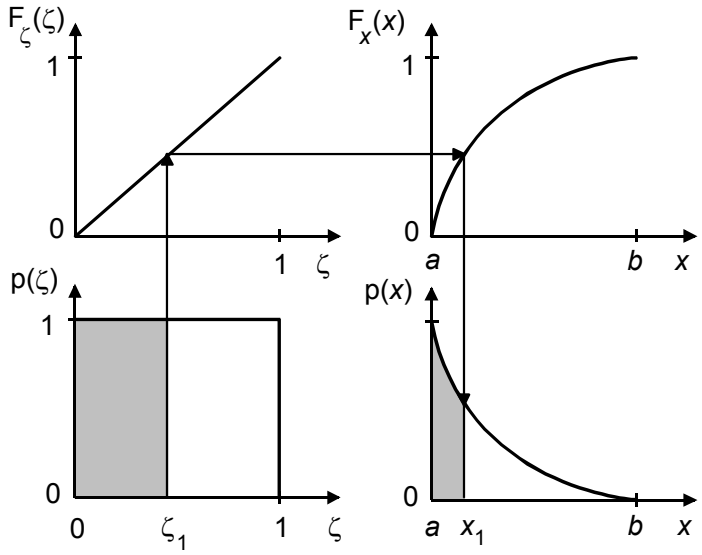

Fig. 3.7 Sampling of a random variable from a non-uniform distribution. The arrows show the mapping from the probability density function p(ζ), via the distribution functions $F_\zeta(\zeta)$ and $F_x(x)$, to the probability density function p(x). The shaded areas are equal, but shown in different scale.

which is the basic equation for sampling random variables from non-uniform distributions using uniformly distributed random numbers. Now, using Eq. (3.68), we are ready to derive how the random variables for step size s, scattering deflection angle θ, and scattering azimuthal angle ψ are sampled. According to the definition of μ_s and μ_a, the probability of interaction per unit pathlength in the medium between s_1 and $s_1 + \mathrm{d}s_1$, is $\mu_t \mathrm{d}s_1$. This can also be expressed in terms of the probabilities:

$$\mu_t \, \mathrm{d}\, s_1 = \frac{-\,\mathrm{d}\, P(s \geq s_1)}{P(s \geq s_1)} . \tag{3.69}$$

Integration of Eq. (3.69) yields

$$P(s \geq s_1) = \exp(-\mu_t s_1) . \tag{3.70}$$

In order for this result to be useful, we need the probability density function used in Eq. (3.68), and we start by rearranging:

$$P(s < s_1) = 1 - \exp(-\mu_t s_1)\,. \tag{3.71}$$

We can directly identify this equation with the result of the integral in Eq. (3.68), so we disregard the step of differentiating Eq. (3.71) to get the probability density function and then integrating back again. Thus, we have

$$\zeta_1 = \int_0^{s_1} \mathrm{p}_p(s)\,\mathrm{d}\,s = 1 - \exp(-\mu_t s_1) \tag{3.72}$$

(we now drop the subscript 1:s for simplicity). Solving for s gives

$$s = \frac{-\ln(1-\zeta)}{\mu_t}\,. \tag{3.73}$$

Lastly, we substitute $1 - \zeta \rightarrow \zeta$, motivated by the fact that ζ is a random number in the interval [0,1], and obtain

$$s = \frac{-\ln(\zeta)}{\mu_t}\,. \tag{3.74}$$

Note that Eq. (3.74) also shows that $1/\mu_t$ can be interpreted as the mean free path between photon interactions, since the statistical average of $-\ln(\zeta)$, with this distribution of ζ, is equal to unity.

The scattering deflection angle θ is sampled from the Henyey-Greenstein distribution, Eq. (3.17). Inserting Eq. (3.17) in Eq. (3.68), and solving for $\cos\theta$, yields

$$\cos\theta = \frac{1}{2g}\left[1 + g^2 - \left(\frac{1-g^2}{1-g+2g\zeta}\right)^2\right]. \tag{3.75}$$

Equation (3.75) is undefined for $g = 0$, so in the limit another expression is needed. $g = 0$ represents isotropic scattering, so $\mathrm{p}(\cos\theta) = ½$ and the correct expression becomes

$$\cos\theta = 2\zeta - 1\,. \tag{3.76}$$

Other phase functions are seldom used in Monte Carlo simulations within the field of tissue optics, but, e.g., the more general Reynolds-McCormick phase function[33] can easily be incorporated with only slightly increased complexity:

$$\cos\theta = \frac{1}{2g}\left\{1 + g^2 - \left[\frac{2\alpha g\zeta}{K} + (1+g)^{-2\alpha}\right]^{-\frac{1}{\alpha}}\right\}, \tag{3.77}$$

where α is an additional parameter and

$$K = \frac{2\alpha g(1-g^2)^{2\alpha}}{(1+g)^{2\alpha} - (1-g)^{2\alpha}}. \tag{3.78}$$

For $\alpha = 0.5$ the Reynolds-McCormick function is equal to the Henyey-Greenstein function. Note that in general, $g \neq \langle\cos\theta\rangle$ for the Reynolds-McCormick phase function.

The azimuthal scattering angle is uniformly distributed in the interval $0 < \psi < 2\pi$, so we get

$$\psi = 2\pi\zeta. \tag{3.79}$$

Following from the definitions of μ_s and μ_a, the probability of absorption at any photon interaction site is $\mu_a/(\mu_s + \mu_a)$. Unless μ_a is very low, this implies that the probability that a photon will survive more than a few scattering events is low. This leads to a problem in photon economy, in that a very large number of photons have to be traced to yield acceptable accuracy at large distances from the source. To improve the accuracy for smaller number of photons, a variance reduction method is used. Instead of terminating a photon at absorption, photon packets are launched, with initial weights W that can take on any number $< W$. This, effectively, is the equivalent of tracing a bunch of photons, which is reduced in number at every scattering event. The weight should then be decreased by the amount

$$W\frac{\mu_a}{\mu_t} \tag{3.80}$$

at every interaction point. Using this technique, the photon packet would be traced forever (or until it escapes a boundary) unless there was some procedure for terminating the trajectory. The termination method is called the roulette. At some point, W is so low that the photon packet contributes little to the simulation. When the weight falls below this threshold value, e.g., 1:1000, there is a one in m chance that the photon packet will survive the roulette procedure. In case it survives, its weight is increased m times, otherwise it is terminated. In this way, the total amount of launched energy in the simulation is conserved.

The number of photon packets needed for a simulation depends on the geometry and the quantity of interest in the problem. For example, to compute the total reflection from a semi-infinite medium, only about 5000 photons may suffice, and the simulation takes less than a second on a PC. To compute the spatial distribution at different radial distances from the source, at least an order of magnitude more photons are needed. Time-resolved data at distances more than 1 cm from the source (for optical properties typical of tissue) needs tens of millions of photons to yield acceptable statistics.

Computer code for Monte Carlo simulations is easy to write using the guidelines above, however, since speed is imperative, a good knowledge of programming at both machine and programming language level is necessary to write efficient code. The finished code should also be validated thoroughly. An important point is the random number generator, which, in computers, usually is in the form of a pseudo-random number generator. Since very long sequences of random numbers are needed, it is essential that the pseudo-random numbers are sufficiently random in a statistical sense, and that the sequence does not repeat itself. Computer-generated random numbers have been discussed in Refs. 44 and 75. The program Monte Carlo simulation for Multi-Layered media, MCML, by Jacques and Wang[76,77], has become somewhat of a standard in the field of tissue optics. The program was written in C. All simulations performed in this thesis were done using codes based on MCML. An adaptation to time-resolved data and more complex geometries was implemented by Berg[78], but the photon propagation routines are the same for all subsequent versions of the program.

3.2.11 Variations on Monte Carlo simulations

In addition to the extended time-resolved version of MCML mentioned in the previous section, other variations on Monte Carlo simulations have been explored. The phase function, which typically is sampled from the analytical Henyey-Greenstein distribution, can instead be incorporated in the simulations using scattering patterns computed with Mie theory or T-matrix theory. Phase functions taken directly from T-matrix computations have been used with MCML within our group[79].

Another powerful approach is the so-called white Monte Carlo method. The amount of computations needed for Monte Carlo simulations can be reduced by performing only one simulation with $\mu_a = 0$, and then adding the absorption afterwards using the Beer-Lambert law. The number of free parameters is then reduced to two: μ_s and g. In case the medium is homogeneous and infinite or semi-infinite, the method is especially powerful, since then it is possible to rescale μ_s by

rescaling the spatial coordinates. The *g*-factor can often be considered constant, and thus only one single simulation is necessary to yield solutions for all combinations of μ_a and μ_s [80,81].

An important question is whether the white Monte Carlo method is equivalent to the conventional approach. The conventional step size is, on average, $1/\mu_t = 1/(\mu_a+\mu_s)$, while it is $1/\mu_s$ with the white method. This will result in different photon distributions. The photon weights are also handled differently. Using the conventional procedure, the photon weight is decreased according to Eq. (3.80) at each interaction. After N steps, the photon packets have, on average, traveled a distance $d = N/\mu_t$, and the weight is

$$W_d = W\left(1-\frac{\mu_a}{\mu_t}\right)^N, \tag{3.81}$$

where W is the initial weight. After the same distance, for a corresponding white simulation, the weight would be

$$W_d = W\exp\left(-N\frac{\mu_a}{\mu_t}\right) \tag{3.82}$$

(note that N still stands for the number of steps in the conventional simulation – in the white simulation the number of steps would be different).

First, let us consider the extreme cases, and start with when the albedo $a \to 1$. Now, the average step sizes of the two approaches become equal, and Eq. (3.82) is mathematically equivalent with Eq. (3.81). Clearly, the white approach is equivalent with the conventional in this limit. This is the regime usually encountered in tissue optics problems. In the other extreme, $a \to 0$, which means no scattering. Physically, this case is described by Beer-Lambert's law for a purely absorbing medium. In the conventional method, the photon paths are now given by $s = \ln(\zeta)/\mu_a$, and the photons are absorbed at the first interaction site. This is statistically equivalent with Beer-Lambert's law. In the white approach, the step size $s \to \infty$, but the photons are in practice always terminated due to interactions with interfaces or a detector. The weights are then updated according to Beer-Lambert's law, and it is clear that again the conventional and the white approaches are equivalent.

In the intermediate regime, when $\mu_a \approx \mu_s$, equivalence is not guaranteed because of the difference between the functions in Eqs. (3.81) and (3.82). A practical example illustrates this. In Fig. 3.8 (a), the results of simulations, using each method, are shown. The spatially resolved reflectance is depicted as a function of the radial

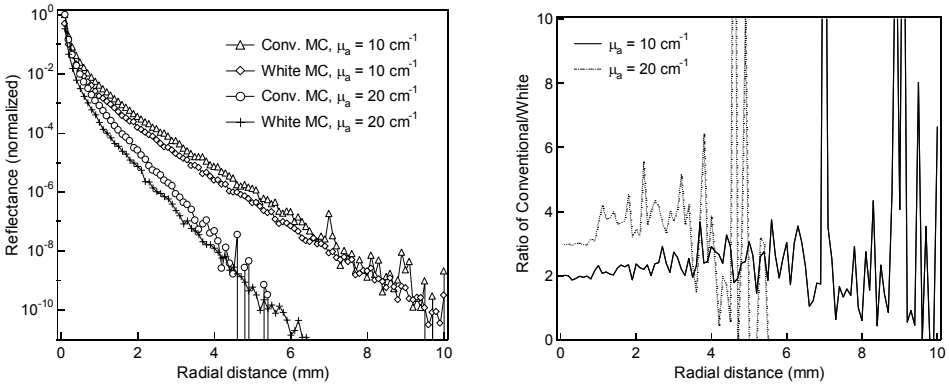

Fig. 3.8 Comparison between the conventional and the white Monte Carlo method. The input parameters were $\mu_a = \mu_s = 10$ cm^{-1} in the first case, and $\mu_s = 10$ cm^{-1}, $\mu_a = 20$ cm^{-1} in the second. The anisotropy factor was $g = 0.5$. A total of 10^6 photon histories were traced for the conventional method, and 10^5 for the white method. In (b), the ratio between the methods is presented.

distance from a point source on the surface of a semi-infinite medium. The optical properties were, in the first case, $\mu_a = \mu_s = 10$ cm^{-1}, $g = 0.5$, and in the second case, $\mu_a = 20$ cm^{-1}, $\mu_s = 10$ cm^{-1}, $g = 0.5$. The ratio between the two methods is also presented in Fig. 3.8 (b), which reveals that the difference is a constant factor, however dependent on the properties μ_a and μ_s.

The white Monte Carlo method has been shown to provide accurate results for tissue optics problems[80-83], and was also used in Paper I.

Transport theory in the form described by the RTE, Eq. (3.7), does not account for any of the wave characteristics of light, such as coherence, interference effects or polarization. It is, however, possible to introduce a description of polarization using the Stokes vector formalism. The scalar radiance must then be replaced by a vector whose components are the Stokes parameters for radiance[26]. This extension is especially well suited for Monte Carlo simulations. The polarization becomes a parameter to be logged for each photon packet, described by the Stokes vector, and the depolarization due to scattering is an additional optical property of the turbid medium, given by the Mueller matrix for each scattering event. A polarization Monte Carlo code has been developed by Wang and co-workers[84], based on the Mueller-Stokes formalism, where the Mueller matrix is calculated from Mie theory. Birefringent media are also possible to simulate[85].

3.2.12 Time-resolved and frequency-resolved calculations

So far in this treatment, frequency-resolved calculations have not been discussed. By frequency-resolved calculations, a procedure where the amplitude of the light source is sinusoidally modulated at a certain frequency is meant, and the detection is performed at the same frequency. From a mathematical perspective, time-resolved and frequency-resolved calculations are equivalent, coupled by the Fourier transform. In some instances, performing the calculation in either domain may be advantageous for numerical reasons, and then the other solution can be obtained by transformation using the Fast Fourier transform (FFT).

In the frequency domain, the propagating light may be conceptually visualized as photon density waves. Care should be taken not to push this picture too far – the photon density is for example always positive and interfering photon density waves can therefore never cancel each other out in the traditional sense, but instead, the modulation becomes zero. The spatial characteristics of photon density waves are also somewhat different from the usual conception of waves, since the fluence rate always obeys $\phi(r_1) > \phi(r_2)$ for all distances from the source $r_1 < r_2$ for diffuse propagation. One may define wavelength, amplitude, and phase properties for photon density waves.

More aspects on frequency-resolved vs. time-resolved measurements are discussed in Sects. 5.3.2 and 5.3.3; Instrumentation.

3.2.13 Fluorescence and inelastic scattering

Fluorescence may be widely defined as a process where light energy is absorbed and re-emitted at a different wavelength than the original light. For the purpose of this thesis, this is as detailed an explanation as is necessary. In a light transport problem, fluorescence phenomena add complexity, but no fundamental new physics. The basic approach to a description of fluorescence within transport theory is to regard the propagation of the excitation light and emission light as two different problems, and find a way to handle the transition of excitation light to fluorescence light. Various Monte Carlo models on this theme were developed in Paper I.

Fluorescence spectroscopy of tissues is a very vivid field of research aiming at developing modalities for diagnostics. Reviews of this research are presented in, e.g., Refs. 86 and 87.

To the level of sophistication of the description presented above, inelastic scattering processes, such as Raman scattering, are treated identically to fluorescence processes. The difference is that while the fluorescence process

usually occur on a time scale of nano- or microseconds, Raman scattering occur on much shorter time scales (femtoseconds).

3.2.14 Photon hitting density and photon measurement density functions

The concept of the photon hitting density describes the expected local time spent by photons traveling from a source to a detector[88]. Another way of expressing this is the probability that any given detected photon at some point has visited a small volume at point **r** in the medium. The photon hitting density is useful to calculate the sampling volume of a measurement, i.e., where the light has been on its way from the source to the detector. This gives rise to the "banana" functions schematically demonstrated in Fig. 3.9 for various measurements. The photon hitting density is time-dependent, which is also illustrated. Schotland *et al*. have derived expressions for time-resolved photon hitting densities in the diffusion approximation[88]. The photon hitting density at **r** can be calculated by considering Fig. 3.10, and using the following equation:

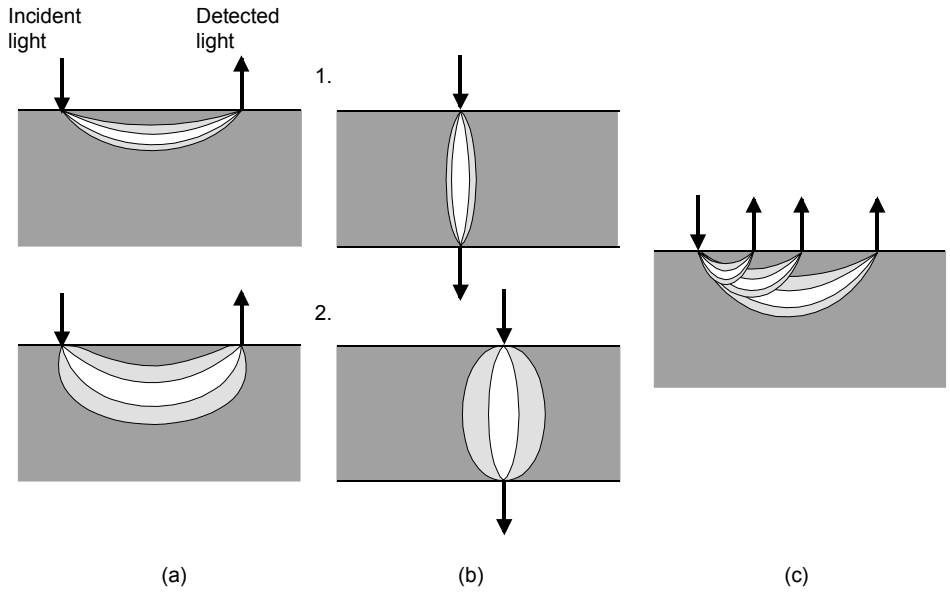

Fig. 3.9 Schematic illustration of sampling volumes (photon hitting densities) of the detected light for various measurements and geometries. In (a), time-resolved reflectance is sketched for early (1) and late (2) light. In (b), similar for a transmission measurement. In (c), the cw reflectance for different source-detector distances is schematically depicted.

$$\nu(\mathbf{r};\mathbf{r}_1,\mathbf{r}_2;t) = \int_{\tau_1}^{t-\tau_2} \phi(\mathbf{r}_1,\mathbf{r};t')E(\mathbf{r},\mathbf{r}_2;t-t')\,\mathrm{d}t', \tag{3.83}$$

where ϕ is the fluence rate at $\mathbf{r}$ due to a source a $\mathbf{r}_1$, and E is the escape function from $\mathbf{r}$ to a detector at $\mathbf{r}_2$. The concept of photon hitting density was generalized to any type of measurement by Arridge, under the name photon measurement density functions[89]. Photon measurement density functions are a measure of the sensitivity of a measurement with respect to small changes in the optical properties[50,89]. As such, they play an important role in reconstruction methods, since they can be used to build the Jacobian matrix in the optimization problem (cf. Sect. 4.5; Optical tomography).

Monte Carlo simulation is a convenient way of obtaining photon hitting densities for arbitrary geometries, since the ensemble of photon trajectories directly yield the photon hitting density. The problem with the Monte Carlo method, however, is its slowness. In Paper I, a variance reduction technique was utilized to improve the efficiency of fluorescence Monte Carlo methods. It was based on separating the computation of the excitation light and the fluorescence light, and furthermore, reversing the computation of the fluorescence light by means of the reciprocity principle. In an analogous fashion, it would be possible to compute the photon hitting density more efficiently by reversing the computation of the escape function E and applying the convolution method in Eq. (3.83). Another option for complex geometries is to use FEM to solve the diffusion equation. Arridge and Schweiger have implemented this in connection with tomographic reconstruction, and utilize the reciprocal computation (they call it the "adjoint" problem) to compute the escape function in their FEM model[50,65].

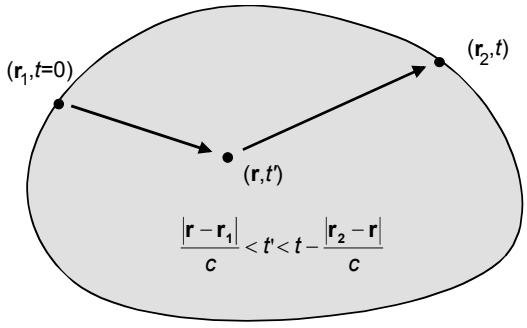

Fig. 3.10 Parameters for the definition of the photon hitting density. The integration limits for t' are also shown, which are defined by the time it takes for the first light to reach $\mathbf{r}$, and the last light to leave $\mathbf{r}$ in order to reach $\mathbf{r}_2$ at time t, respectively.

3.3 Discussion – solving the forward problem

In the previous sections, a map of various methods to solve the forward problem has been presented. The method of choice for a particular problem is sometimes obvious, but, often, tradition and familiarity governs what method people choose, even though it might not be the optimal choice. Here, we will discuss some general properties of the most widely used methods, and compare them with each other. Often, the method is to be used as a means to solve the inverse problem, which is the topic of next chapter. Therefore, this discussion should also be taken as a starting point for the review of inverse methods in the next chapter.

The diffusion approximation is probably the most widely used method in tissue optics. The method has many attractive properties. Analytical solutions exist for several geometries that are useful in practice. Numerical computations using finite-differencing schemes or FEM are conveniently manageable on personal computers. The diffusion equation directly gives the fluence rate everywhere in the medium, which makes it simple to calculate the absorbed dose, by multiplication with the absorption coefficient, Eq. (3.14). Diffusion theory is therefore often used for dose calculations. The obvious drawback of the method is the restricted validity: the requirement $\mu_a << \mu_s'$, and that the solutions are inaccurate close to the source. Many complex media consist of different regions, some with high μ_s' where the diffusion approximation is perfectly valid, but others where the scattering is low. In some cases, high absolute accuracy is not a great concern, and in such situations the method can still be useful. An example is reconstruction in optical tomography, which will be discussed in more detail in Sect. 4.5.

The discrete ordinates method and the Monte Carlo method are similar in the sense that both, in principle, solve the RTE accurately without approximations or limitations. These methods are based on entirely different principles, but both consume large amounts of computer power. The Monte Carlo method is preferred whenever the distance between the light source and detector is small. The number of photons required for acceptable accuracy increases exponentially with the distance, so at distances larger than a few hundred mean free paths (2 – 3 cm in typical tissue), the computation time becomes unrealistic. Discrete ordinates computation time is proportional to the grid size, i.e., to the number of mean free paths cubed, so although the computation requires powerful computers, it may still be realistic to perform a discrete ordinates calculation in situations when the Monte Carlo method is impossible.

The Monte Carlo method, thanks to its high accuracy, has gained a position as a reference method that other methods are measured against. A large number of models based on diffusion theory have been validated by means of Monte Carlo simulations [53,56,90-100]. Several authors have also presented hybrid models, where the

region close to the source is modeled using Monte Carlo simulations, while in the diffusive region far from the source diffusion theory takes over[92,98,99].

3.3.1 Relationship between wave theory and transport theory

The relationship between electromagnetic wave theory and transport theory is a question of fundamental interest. The two theories represent two different views of light propagation on different levels of description. However, a link between these two levels have already been discussed in connection with the phase function, which can be calculated using, e.g., Mie theory, and incorporated into transport models. The relation between wave and transport theory has been discussed by Fante[101] and Ishimaru[26]. Their analysis shows that the quantity radiance, as used in transport theory, can be regarded as a statistical average of the time-varying Poynting vector in wave theory, and thus that there exists a formal link between the two theories.

Links between the wave and transport representations are important for practical reasons as well. In the transport models, the scattering properties can only be measured; there is no way of calculating the scattering coefficient from knowledge of the composition of the medium. The simple example of scattering microspheres shows how the scattering coefficient can be calculated using wave theory, and then be applied in a transport model. In some media, the transport scattering coefficient changes dramatically due to microscopic configurational changes. An example is blood, which was studied in Papers V and VI. The only way to predict the complicated variation of the scattering coefficient in blood under different conditions is by means of applying wave theory on the scattering problem on the microscopic level. Another example is when polarization effects are included in transport models. Within the context of transport theory, depolarization of an incident light beam is a property that can only be measured. On the other hand, using for example Mie theory, it is relatively easy to calculate the depolarization in connection with scattering from spherical particles[84].

4. The inverse problem

Returning to the very general description as posed in the introduction (Fig. 2.1), we repeat the formulation of the inverse problem: find the optical properties $\mathbf{p}(\mathbf{r})$, given that we have measured the propagating light $X_{prop}(\mathbf{r},\mathbf{s},t)$, or some portion of it. A linear representation of the forward problem would be

$$\mathbf{X} = \mathbf{A}\mathbf{p}\,, \tag{4.1}$$

where $\mathbf{A}$ is a matrix describing the forward mapping, and the solution to the inverse problem simply becomes

$$\mathbf{p} = \mathbf{A}^{-1}\mathbf{X}\,. \tag{4.2}$$

This matrix representation implies that we assume that the problem is discretized: we always search for the properties $\mathbf{p}(\mathbf{r})$ in a finite number of regions, each of which is considered homogeneous, and measure $X_{prop}(\mathbf{r},\mathbf{s},t)$ in a finite number of independent measurements (Fig. 4.1). Unfortunately, the forward problem of light propagation in turbid media is not linear, so the inverse problem cannot usually be solved by simple matrix inversion without approximations. Instead, the general

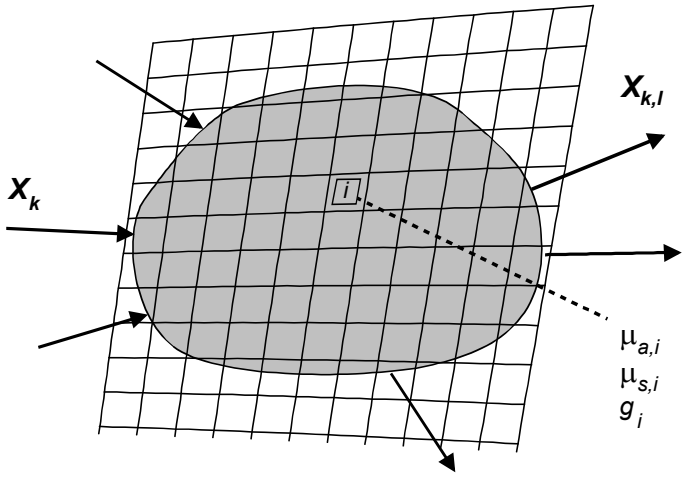

Fig. 4.1 Schematic picture of the general discretized inverse problem. The medium is divided into N voxels, here indexed by i. Each voxel is assumed to have the optical properties $\mu_{a,i}$, $\mu_{s,i}$, and g_i. The medium is illuminated with light denoted X_k, at positions indexed by k. The detected light denoted $X_{k,l}$, where the detection points are indexed by l. The total number of measurements is M, and the total number of unknowns is $3N$.

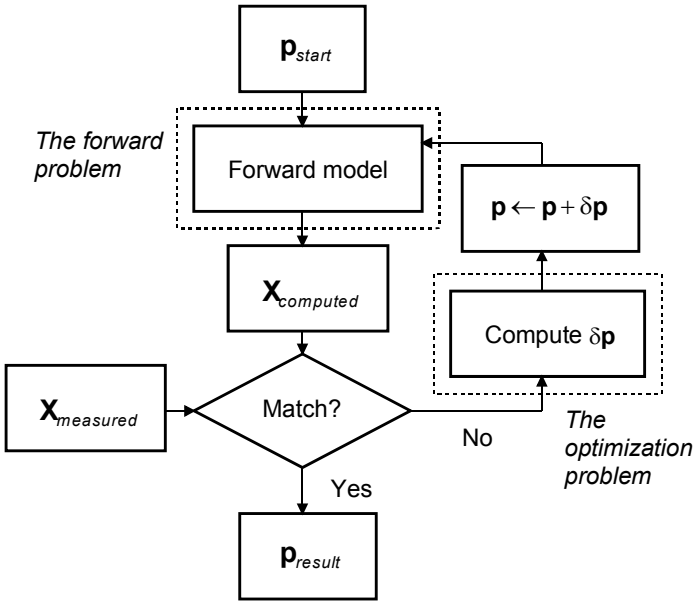

Fig. 4.2 The principle of solving a non-linear inverse problem by means of an iterative algorithm.

approach for non-linear inverse problems is iterative. This procedure is illustrated in Fig. 4.2. The process is started by guessing initial values of $\mathbf{p}(\mathbf{r})$, which are fed to the forward model. The computed values of $X_{prop}(\mathbf{r},\mathbf{s},t)$ are then compared with the measured, and using a suitable minimization algorithm the values of $\mathbf{p}(\mathbf{r})$ are updated. The process is repeated until the computed and the measured values match within required accuracy, at which point the current values of $\mathbf{p}(\mathbf{r})$ are taken as the final result.

In this chapter, we will focus on some of the more important aspects of the inverse problem. The first consideration is the number of unknowns in the problem. This is often the number of spatial regions times the number of optical properties in each region, but sometimes there are also geometrical parameters as unknowns, such as the thickness of a layer. An important special case is when the medium is considered homogeneous, and the number of unknowns is reduced to the number of optical parameters. When the number of spatial regions is large, what we are attempting is effectively three-dimensional mapping, or imaging, of the internal structure of the turbid medium. The ultimate goal of this branch of tissue optics is a method for complete reconstruction of the optical properties at every point in the medium. This topic is covered in the section on optical tomography, Sect. 4.5.

The first choice is which forward model to use. Methods based purely on electromagnetic wave theory have never really been applied to inverse problems in complicated turbid media, due to the computational requirements. Mie theory can be used to characterize the properties of aerosols by measuring the scattering pattern. Determining the geometry of aircraft from radar signals is another inverse problem of this kind, albeit more complicated. In Paper V, an attempt was made to explain the optical response from whole blood by means of T-matrix calculations. However, the comparison was mainly qualitative, and the model cannot at present be used as a forward model for the inverse problem. In the following treatment, only models based on transport theory will be considered.

Next, the type of measurement is an important factor. Ideally, the number of measurements should equal the number of unknowns, and they should all be orthogonal in measurement space. In reality, the inverse problem is often ill conditioned – some measurements are almost parallel in measurement space, and in the case of imaging the number of measurements is smaller than the number of unknowns. In image reconstruction, regularization methods are used to handle these problems. For measurements of homogeneous media, the way to handle ill-conditioned inverse problems is usually by one or several of the following methods: (A) choose the measurement carefully to avoid or minimize the ill-conditioned inverse; (B) minimize noise and errors in the measurement; (C) use appropriate numerical methods to handle ill-conditioned problems.

The third part is the choice of optimization method. Many minimization algorithms use the derivative, or an estimation of the derivative, to calculate the step $\delta\mathbf{p}$ that $\mathbf{p}(\mathbf{r})$ will change in each iteration. Examples of standard algorithms are the downhill simplex method (which does not require the use of the derivative) and the conjugate gradient method (which does use derivatives)[44]. For image reconstruction, efficient minimization routines are even more important because of the high computational cost of evaluating the forward model for complicated geometries; as few iteration steps as possible is desirable. This topic will be discussed more in Sect. 4.5.

4.1 Two-parameter methods

The lowest number of unknowns possible is $N = 1$, meaning that only either the scattering or the absorption is unknown. The other parameter is then assumed known. We will, however, start the discussion with two-parameter methods, where both the reduced scattering μ_s' and the absorption μ_a are unknowns, and the medium is assumed homogeneous. An important fact immediately comes up: it is not possible, using any two-parameter method, to measure μ_s. Either μ_s' is

measured, or both μ_s and g are measured, the latter which renders the method a three-parameter method. Two-parameter methods are based on measurements of the diffuse reflectance or transmittance from the medium, which can be spatially resolved, time-resolved or frequency-resolved. These three methods are depicted in Fig. 4.3. The bulk refractive index of the medium is assumed to be known in these methods.

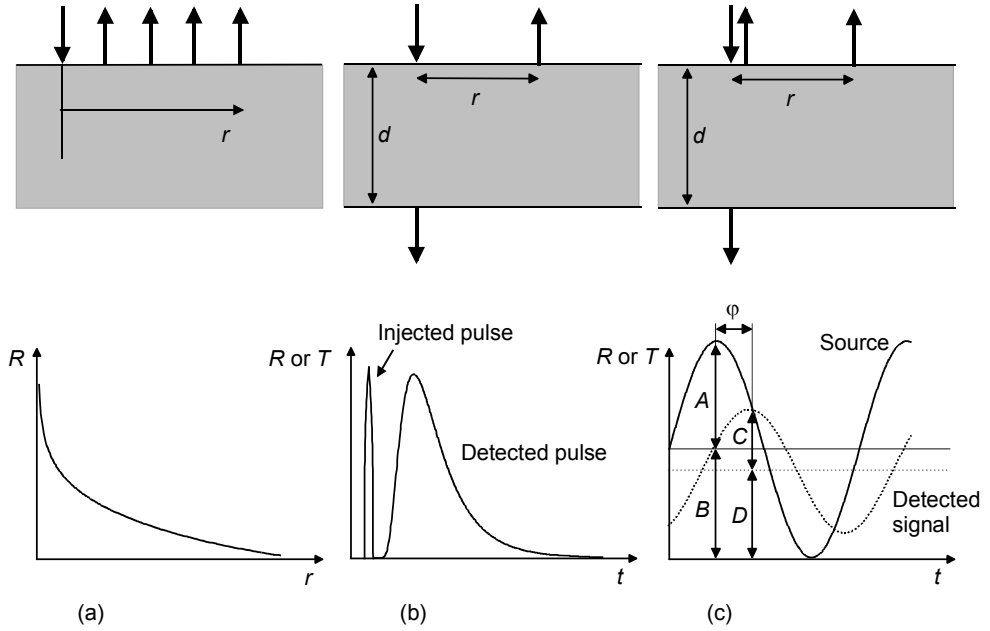

Fig. 4.3 Three types of measurements to obtain the two parameters μ_s' and μ_a. (a) Cw spatially resolved reflectance measurement; (b) time-resolved measurement by injecting a short pulse and measuring the temporal point-spread function (either reflectance or transmittance mode); and (c) frequency-modulated measurement (either reflectance or transmittance mode). In (c), the phase shift φ and the modulation depth = $(C/D)/(A/B)$ are measured.

4.1.1 Spatially resolved diffuse reflectance

Spatially resolved diffuse reflectance measurements based on continuous wave (cw) light can be evaluated by fitting the measurement, $R(r)$, with the diffusion equation, Eq. (3.62). A measurement of $R(r)$ generally leads to an over-determined inverse problem, since only two values, $R(r_1)$ and $R(r_2)$, in principle are necessary. The optimal distances r_1 and r_2, in the sense that the measurements are orthogonal, can be found by considering Fig. 4.4. The "hinge" and "pivot" points indicate the

distances of invariance in terms of μ_a and μ_s', respectively. Typically, for optical properties that are relevant for biological tissue, $r_1 \approx 0$, while $r_2 \approx 3$ mm[102]. In practical situations, measuring at more than two positions is sensible, to make the method more robust with respect to measurement errors or small inhomogeneities at the measurement position. Since measurements close to the light source are necessary to obtain orthogonal measurements, the diffusion equation is not an ideal forward model. Still, several authors have shown good results using the diffusion equation[103-106]. Alternatives to the diffusion equation are to use the Monte Carlo method[107], or simply to calibrate the measurement on phantom samples with known optical properties[102]. The latter method requires the use of a non-linear calibration method (cf. Sect. 4.4).

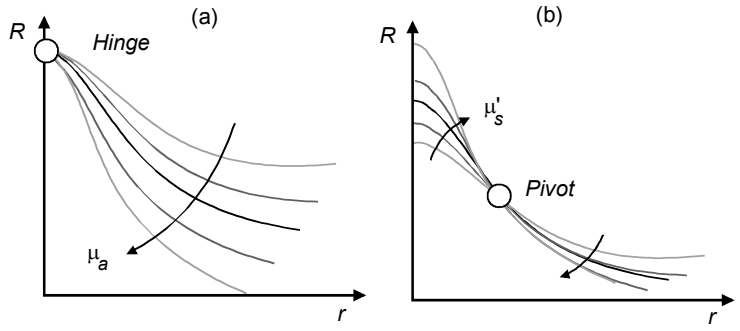

Fig. 4.4 Spatially resolved reflectance $R(r)$. In (a), μ_a is varied and the point of invariance, the "hinge" point, is close to the source. In (b), μ_s' is varied and the "pivot" point marks the point of invariance. Adapted from Dam[129].

Spatially resolved measurements provide several attractive properties: the instrumentation can be made inexpensive, small and portable, and the measurements can be done *in vivo* on patients. A drawback is that the method is fairly sensitive to inhomogeneities in the medium, for two reasons. Firstly, the light probes different volumes, at different depths, depending on the distance from the light source (cf. Fig. 3.9). Secondly, since the cw intensity is measured, the measurement is susceptible to small inhomogeneities, such as an absorbing spot, close to the measurement site. The latter can be partly overcome by measuring at several positions along concentric circles around the light source, and integrating over the angle ψ[102,107]. An additional limitation of spatially resolved measurements is that deep structures inside the medium are inaccessible.

4.1.2 Time-resolved diffuse measurements

Time-resolved measurements are performed by using short light pulses, in the picosecond regime, and measuring the temporal point-spread function (TPSF) at some distance from the injection point. The standard way of evaluating these measurements is by fitting with the diffusion equation, Eq. (3.61). Diffusion theory is well suited for this problem, since the distance between the source and the detection point can be kept rather large. The fitting is performed with a non-linear curve-fitting algorithm, e.g., the Levenberg-Marquardt method[44,108]. In an analogy with the spatially resolved measurements, in principle only two values from the TPSF are necessary to deduce μ_s' and μ_a. In rough terms, the early part of the TPSF curve is invariant with respect to μ_a, while the tail is invariant with respect to μ_s'. In fact, a reasonably good estimation of μ_a can be obtained by simply measuring the slope of the trailing edge in a lin-log graph, as can be seen from the exponential expression in Eq. (3.61).

Although diffusion theory is often adequate as the forward model, sometimes one wishes to measure with short source-detector distances. The Monte Carlo method then useful. The problem is the computation time required when the Monte Carlo method is incorporated in an iterative scheme like in Fig. 4.2. The computation time can be reduced substantially by applying the white Monte Carlo method (Sect. 3.2.11). Only one simulation is then necessary, and the fitting can be performed by rescaling the curve and adding absorption[80,81].

Time-resolved measurements solve some of the problems associated with spatially resolved cw measurements. The method is less sensitive to small inhomogeneities, since only the shape of the TPSF curve and not the absolute intensity is used. A small absorbing spot close to the detection point will thus only act as a gray filter, and reduce the amplitude of the TPSF. The method is also ideal for measurements of large volumes, as long as the intensity of the light is high enough to be detected. The major drawback of the method is the expensive and complicated instrumentation (cf. Sect. 5.3.3; Instrumentation). Like spatially resolved measurements, time-resolved measurements are ideal to perform *in vivo*.

Measurements with sinusoidally amplitude-modulated light are mathematically equivalent with time-resolved measurements. Expressions that directly link the measured phase and modulation from frequency-resolved measurements to μ_s' and μ_a have been developed, based on diffusion theory[109,110].

4.2 Three-parameter techniques; The integrating sphere method

An elegant way of determining all three optical properties – μ_s, μ_a and g – is presented by the integrating sphere method. The technique requires small samples, which may be an advantage in some situations, but usually it is the main limitation of the integrating sphere method, since *in-vivo* measurements of tissue are impossible. An integrating sphere is designed to collect all light flux that enters the sphere, and a portion of it, α, is detected by a detector that is mounted at a position on the sphere wall. The samples are cut into thin slabs (usually around 1 mm for biological tissue), which can be placed either at the entrance port or the exit port of the sphere (see Fig. 4.5). The sample is illuminated by a collimated light beam that is aligned with the optical axis of the two ports of the sphere (other measurement geometries are possible, e.g., diffuse illumination of the sample[111,112]). This set up enables measurement of the transmittance (T) and reflectance (R) of the thin sample. When the transmittance measurement is performed, the exit port is covered with a calibrated plug with known (high) reflectance, R_{ref}. A reference measurement is carried out with no sample, which yields a measure of the

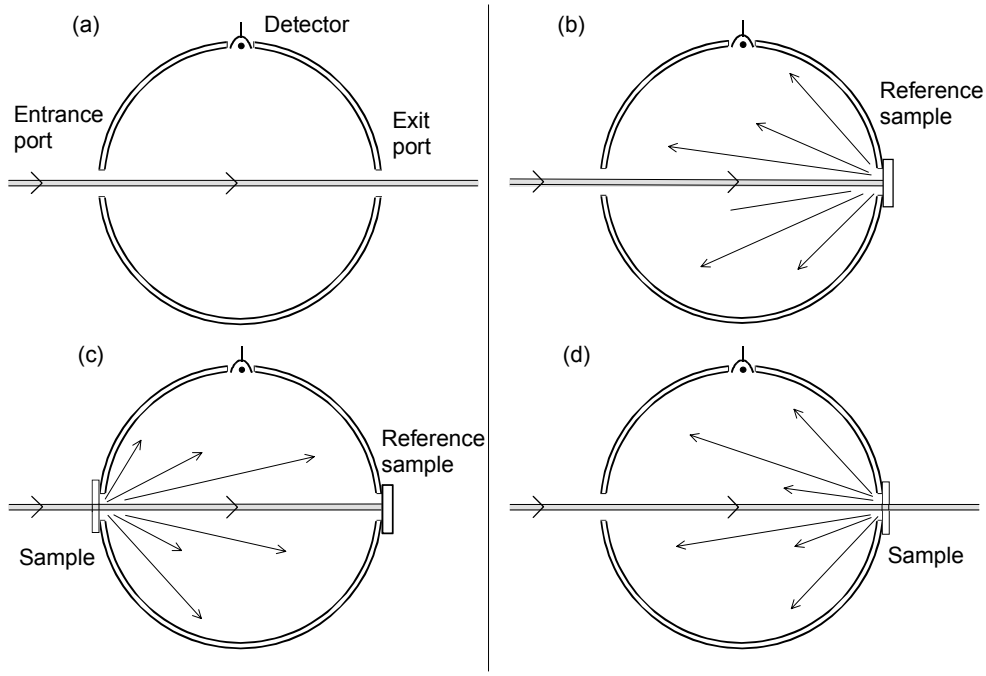

Fig. 4.5 Integrating sphere measurements. (a) shows the basic set-up, with a collimated beam along the port axis of the sphere. This is also used to perform background measurements. In (b), a reference measurement is performed on a calibrated sample which yields αE_0. In (c), the transmitted signal αE_T is measured. Finally, in (d), the reflected signal αE_R is measured.

unattenuated beam, αE_0. From the sample measurements, αE_T and αE_R, the transmittance and reflectance can be calculated as

$$T = \frac{\alpha E_T}{\alpha E_0} = \frac{E_T}{E_0} \tag{4.3}$$

and

$$R = R_{ref} \frac{\alpha E_R}{\alpha E_0} = R_{ref} \frac{E_R}{E_0} . \tag{4.4}$$

So far, the method described is a two-parameter method: knowledge of R and T is sufficient to determine μ_s' and μ_a. In this way, the integrating sphere method was used in Paper V to measure the optical properties of flowing whole blood. To determine the g-factor, and thus separate μ_s' in μ_s and g, a third measurement is necessary. The usual procedure is to measure the collimated transmittance and derive μ_t using Beer-Lambert's law, Eq. (3.36). The three parameters, R, T and μ_t, are sufficient to give a reasonably well-conditioned inverse problem.

To solve the inverse problem, the adding-doubling method has been used extensively as the forward model[112-114]. Adding-doubling provides quick computations, but suffers from an important weakness. In practice, there are always lateral losses of light due to the finite size of the sample and/or integrating sphere ports. Such losses lead to underestimation of R and T compared with the ideal case, which in turn lead to overestimation of the absorption properties of the sample[115,116]. Another approach is to use the Monte Carlo method, where the lateral losses easily can be incorporated in the model. The problem with Monte Carlo simulations is again the long computation time. To overcome this, one can compute a database of values of R and T which spans the region of μ_s, μ_a and g of interest, and then interpolate in this database to find the correct values[117-119]. The solution of the inverse problem is thus transferred to a method of using look-up tables. The interpolation algorithm can be made in different ways, e.g. by using spline interpolation[117-120], which was applied in Papers V and VI, or by means of a polynomial regression technique[121]. The latter method has proved to be superior, and was used in Papers II and IV. The polynomial regression technique is described in more detail in Sect. 4.4.

Several sources of error have to be considered when performing integrating sphere measurements. One type has to do with the sphere itself, and occur because the ratio between the area of the various ports of the sphere and the total area of the sphere is not zero. Fundamental integrating sphere theory has been treated by several authors[111,122-124]. The most influential sphere error occurs in the

measurement of the transmittance. The sphere geometry is affected slightly by introducing the sample at the entrance port, so that the sample itself can reflect some of the light inside the sphere. The reference measurement, taken without sample, should therefore be corrected. An alternative, superior, to Eq. (4.3) for calculating T is given by

$$T = \frac{E_T}{E_0} \frac{(1-\varepsilon_s)R_w\{1-[(1-\varepsilon_s)R_w+\varepsilon_s R]\}}{[(1-\varepsilon_s)R_w+\varepsilon_s R][1-R_w(1-\varepsilon_s)]}, \tag{4.5}$$

where ε_S is the ratio of the sample port to the total sphere area, and R_w is the reflectance of the sphere wall[124]. An example of the correction factor compared with Eq. (4.3), for the sphere used in the experiments in this thesis (Papers II, IV – VI) is shown in Fig. 4.6. The correction in Eq. (4.5) can be improved further by incorporating effects due to the fact that some of the transmitted light is still collimated, but this correction is small compared with Eq. (4.5)[125].

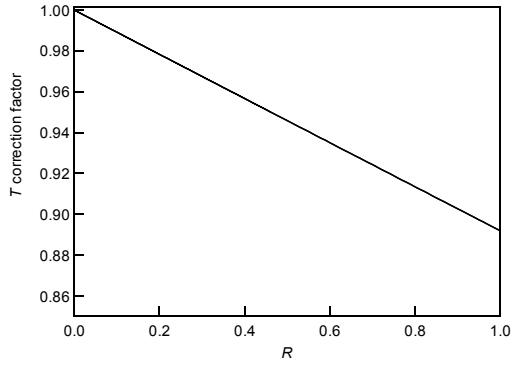

Fig. 4.6 Correction factor for T according to Eq. 4.5, for the sphere used in this thesis. The sphere properties were $\varepsilon_s = 0.0035$ and $R_w = 0.97$.

The correction factors become more important when two integrating spheres are used simultaneously, because of cross talk through the sample between the spheres. The double integrating sphere set up has been used as a means to provide simultaneous measurement of R and T [111,112,114,118]. However, the derived correction factors for the double integrating sphere are dependent on the assumption of diffusely transmitted and reflected light from the sample, and the accuracy is degraded when this requirement is not fulfilled. The double integrating sphere method should therefore be used with caution.

The next important potential source of error has already been mentioned: lateral losses of light due to the finite size of the ports. This leads to overestimated absorption properties for samples with low absorption[115,116]. The losses can easily be 5% for a typical measurement on a sample with low absorption, which means that $R + T \approx 0.95$ instead of the true $R + T \approx 1$. The lateral losses can be corrected when the Monte Carlo method is used for evaluation. Measurement of low absorption coefficients is, in general, a weak point of the integrating sphere technique, even if the above corrections are included. The absolute error in the evaluation of μ_a is directly determined by the error in the measurement of R and T. If μ_a is small, even an error as small as 1% in the measurement will lead to relative errors of several hundred per cents in μ_a.

The collimated-beam measurement has its own potential sources of error. The fundamental idea behind this measurement is to detect only the light that has penetrated the sample without being scattered. Ideally, this implies measuring in a zero collection angle. In practice, the measured signal is proportional to

$$E_{meas} = E_{col} + \varepsilon E_{scattered}\,, \tag{4.6}$$

where ε is the fraction of the scattered light that falls inside the collection angle of detection. Suppressing the scattered light in the set up is imperative, but at some point the fraction of scattered light can no longer be neglected. The error increases linearly with sample thickness and scattering coefficient, quadratically with the collection angle, and is inversely quadratically proportional to $(1 - g)$ and the refractive index of the sample[126]. In practice, the range of possible measurements can be increased either by making the samples thinner, or increasing the radiance of the light source to enable a smaller collection angle of the detector. Before any collimated attenuation measurements can be trusted, a thorough characterization of the experimental set-up must be performed. This is done by recording E_{meas} for a series of samples with known values of μ_t, and then plotting these in a lin-log graph to determine the linear range, and upper threshold value of μ_t for which the measurements are relevant. The dynamic range of the measurement with the sample compared with the reference measurement is also a problem, which can be solved by using neutral density filters for the latter measurement. This was practiced in Papers II and IV.

Using a laser for the collimated beam measurement would seem ideal, because of the high radiance. Unfortunately, the high coherence of most lasers introduce other errors in the measurement. The sample is usually placed in a glass cuvette, or clamped between two glass plates. When using a high coherence light source, interference effects in the glass plates can cause large variations in the detected signal.

The collimated beam measurement can be combined with the double integrating sphere for simultaneous measurement of all three parameters. However, in this situation, some of the scattered light from the sample will reflect off the wall of the second sphere, reflect again off the sample and interfere with the measurement. The problems associated with this kind of measurement have been discussed in Ref. 120. The conclusion was that often only relative measurements of the optical properties are possible using this set up, due to the errors. This can, in some instances, be a price worth paying for the benefit of being able to measure all three properties simultaneously.

The integrating sphere method is ideal for situations where destructive testing can be tolerated. It has been used on paper, plastics, and other materials. One interesting application is transparent PLZT ceramics, which change their scattering characteristics when a voltage is applied[127]. For biological tissues, the situation is more complicated. If *in-vitro* sampling can be tolerated, additional problems arise because the tissue is affected by the handling. The absorption properties *in vivo* depend on both the blood circulation and the oxygen saturation of the tissue. These effects are not present in *in-vitro* measurements, which means that the obtained absorption coefficients do not reflect the *in-vivo* situation. The scattering properties are, however, usually relatively unchanged by *in-vitro* handling, with the exception of fatty tissue if the temperature is allowed to drop to room temperature, which causes crystallization of the fatty acids. Some of these aspects are discussed in Paper IV.

The integrating sphere method, combined with a collimated beam measurement, in practice provides almost the only way to measure all three parameters (μ_a, μ_s, and g) of bulk material accurately. The g-factor can also be measured using a goniometric technique[128], but this method is more complicated, and yield the same problems with *in-vitro* handing as the integrating sphere method. A technique that resembles the integrating sphere method has been proposed by Dam[129], which does not require the use of an integrating sphere. Instead, the method relies on measurements of the scattered light in only a few, well chosen positions and angles from a thin sample. The optical properties can then be determined using an inverse Monte Carlo method, much like for the integrating sphere.

One technique for measurement of the g-factor in moving, scattering liquids (such as blood) has been proposed, based on laser Doppler measurements[130]. The method utilizes the fact that for high values of g, a small change in g is related to a large relative change in the average scattering angle. The Doppler shift is proportional to $\sin(\theta/2)$, which means that the Doppler spectrum is sensitive to small variations in g. The g-factor can be determined by fitting the measured Doppler spectrum with theoretical spectra from Monte Carlo simulations. However, the method requires that μ_s is known, and is thus not a true three-parameter method.

4.3 Layered media and simple embedded inhomogeneities

N-parameter methods where *N* is small and the medium is inhomogeneous, yet still simple, can be generalized from the homogeneous methods. A semi-infinite, two-layered medium is interesting from a tissue optics perspective, since a two-layer geometry, while far from perfect, presents a much more realistic model than a homogeneous in many situations. For example, the skin usually has different optical properties than the underlying tissue (cf. Sect. 5.1; Optical properties of tissue). Here, one can assume that $N = 5$ for the full inverse problem (provided that the bulk refractive index is assumed known): μ_{s1}', μ_{a1}, μ_{s2}', μ_{a2}, and the thickness of the upper layer. At this level of complexity, hope of measuring μ_s and g separately is given up. The problem can be simplified if one or more of these properties are known *a priori*. A natural measurement would be to perform time-resolved detection at two or three distances from the source: at close distances, primarily the top layer is probed, while at longer distances, more of the lower layer will be probed. This two-layered problem has been approached by several investigators[57,96,97,131,132]. Typically, the diffusion approximation is used as the forward model, although a hybrid Monte Carlo-diffusion model has also been presented[99]. The optimal source-detector distances depend on the optical properties and the thickness of the upper medium, so some prior knowledge of the medium greatly helps in the measurement.

A method to solve the inverse problem for many layers has been presented by Hielscher *et al.*[133]. The method is based on tomographic reconstruction techniques, which is the topic of Sect. 4.5. An analytical approach for the multiple-layer problem was adopted by Ripoll *et al.*[132]

Other examples of simple inhomogeneous geometries include spherical inclusions. This geometry has often served as a simple model of a tumor inside the tissue. Analytical solutions for the diffusion equation exist[59], and some investigators have developed inverse models[134-136]. Inverse models for cylindrical inhomogeneities have also been treated[137].

4.4 Polynomial regression

The high computational cost of most forward models is a fundamental problem for the inverse problem. When the number of unknowns is low, as for the two- or three-parameter methods, an alternative to performing the forward computation in an iterative fashion is to approximate the solutions to the forward model with *N*-dimensional polynomials. The inverse problem can then be solved using a fast root

solver. In Papers II and IV, this method was used to evaluate the integrating sphere measurements, where $N = 3$. A pre-computed database of Monte Carlo results was generated, yielding maps of R and T as functions of μ_s, μ_a and g (see Fig. 4.7). The Monte Carlo data were then fitted to an expansion of Chebychev polynomials with least-squares regression, as is shown in Fig. 4.7. Chebychev polynomials form a complete orthogonal function set and are thus suited for this kind of expansion. The result is the polynomials $R_{cheb}(\mu_s,\mu_a,g)$ and $T_{cheb}(\mu_s,\mu_a,g)$. To determine the optical properties from the measured values R_{meas}, T_{meas} and $\mu_{t,meas}$, the new polynomials

$$F(\mu_s,\mu_a,g) = R_{cheb}(\mu_s,\mu_a,g) - R_{meas} \tag{4.7}$$

$$G(\mu_s,\mu_a,g) = T_{cheb}(\mu_s,\mu_a,g) - T_{meas} \tag{4.8}$$

$$H(\mu_s,\mu_a,g) = \mu_s + \mu_a - \mu_{t,meas} \tag{4.9}$$

are formed. The solution is obtained by finding the common roots of the polynomial equations formed by setting these polynomials equal to zero. A Newton-Raphson solver was used for this.

The advantage of the polynomial regression technique over spline interpolation is that the former smoothes the statistical errors in the individual Monte Carlo data points, yielding better accuracy than splines, which tend to follow the small deviations of every data point exactly[121]. The polynomial regression technique is also faster than spline interpolation, although computation time is not, in practice, a problem for either method on a modern computer.

The use of regression methods is also convenient when, instead of a forward model, a calibration is performed to determine the optical properties. The database of Monte Carlo results is then replaced by measurements on samples with known optical properties (phantoms, see Sect. 5.2). This technique was employed in Paper II to calibrate the spatially resolved fiber probe system.

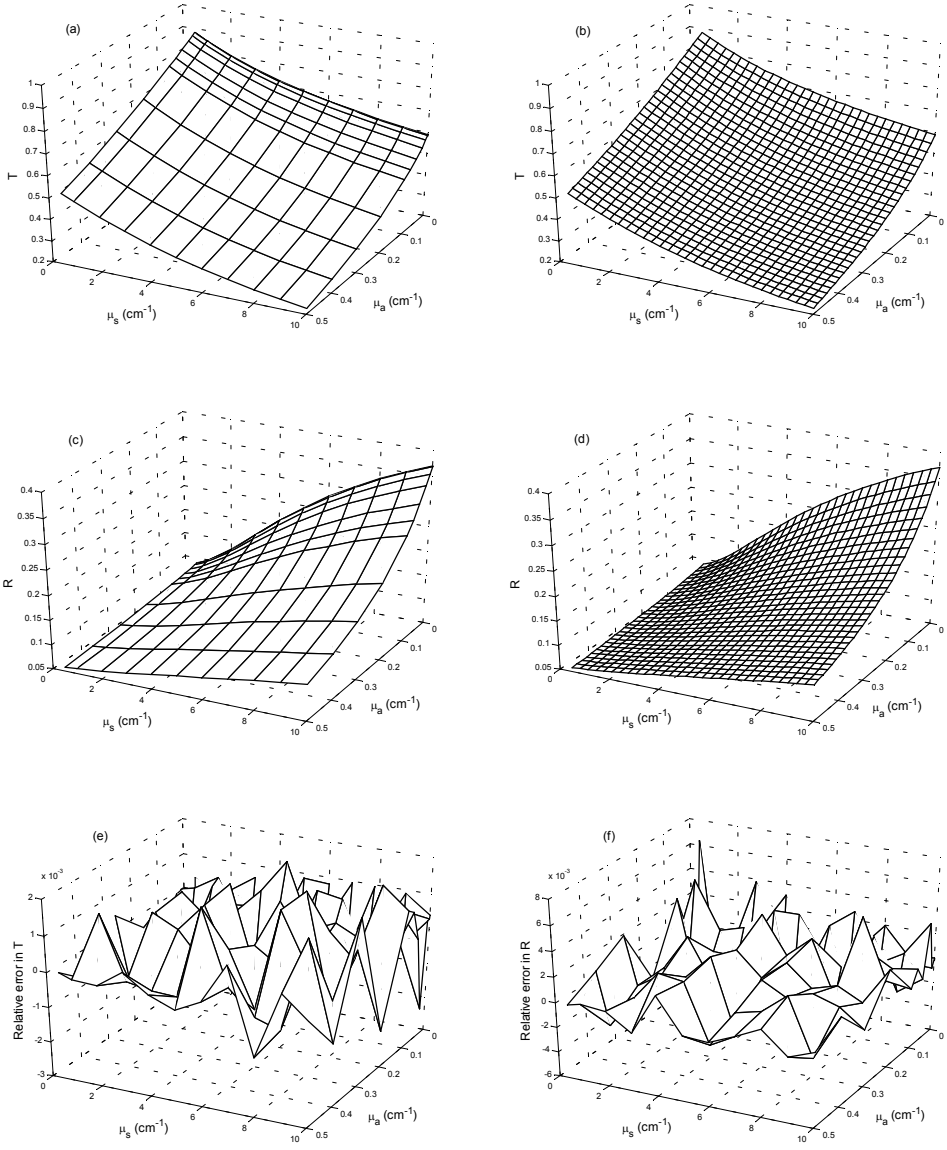

Fig. 4.7 Polynomial regression for Monte Carlo data to solve the inverse problem for integrating sphere measurements. (a) and (c) show the Monte Carlo-computed data for T and R, respectively. (b) and (d) show the corresponding fitted polynomials. (e) and (f) show the relative error between the Monte Carlo data and the polynomials. Data are shown for $g = 0.9$.

4.5 Optical tomography

An initial step toward a full reconstruction of the optical properties at every point in a medium is to perform a series of measurements using one of the methods previously described, either in scanning mode or in parallel. This procedure yields a spatial (topographic) map of the approximate optical properties between the source-detector pairs. An example of this kind of measurement in reflectance mode is monitoring the oxygen saturation state in brain cortex (parallel mode)[138-140]. Transmission mode measurements of this kind have been done through female breasts to detect tumors (scanning mode)[136,141]. The measurements can be either time-resolved or frequency-resolved.

In some instances, recovery of the scattering and absorption properties may not even be necessary. Examples of this are when only a contrasting region is to be detected, or when searching for a dynamic change in a region. In the case of breast cancer detection, the time resolved data (the TPSFs) can be analyzed directly in terms of early or late light time windows[136,142], in order to find the optimal spatial contrast function. Dynamic changes in blood flow in different areas can be detected by direct correlation coefficient analysis[140]. However, finding contrast by using direct methods can be problematic for several reasons. The shape of the sampling volume of the light through a scattering medium implies that most of the contrast will emanate from structures close to either the source or the detector, while deep structures tend to stay unrevealed. In addition, these methods yield little or no information on the functional origin of the contrast, which makes it difficult to optimize the contrast function, and also knowing what one actually sees.

True 3D reconstruction of the optical properties, i.e., μ_s' and μ_a, is often denoted optical tomography (or diffuse optical tomography). The inverse problem is usually denoted reconstruction in this context. An early proposal to solve the reconstruction problem was made by Singer *et al.*[143]. The forward model was in this case a simple six-way flux model, and the inverse problem was solved in the way depicted in Fig. 4.2, using a gradient descent method to minimize the difference between the computed and measured data. During the last decade, extensive research has been conducted within the field, both in terms of instrument development and theory. The difficulties on the theoretic side can be categorized by the need to reduce the amount of computations, and how to best handle the ill-posed nature of the inverse problem.

An issue of fundamental interest is whether a unique solution to the reconstruction problem exists in general. This question has been explored and it can be shown that if only cw measurements are performed, there is no unique solution even in principle[144]; many solutions exist that give identical measurement data. For time-resolved and frequency-resolved measurements, a unique solution exists in

principle, but only in the limit of continuous source distribution and measurements. In practice, therefore, reconstruction problems should be considered non-unique. The implications are that the reconstruction problem is fundamentally ill conditioned, and that reconstruction from cw measurements is even more so. Nevertheless, some authors have reported that reconstruction using cw data is possible in practice[145,146].

The brute-force approach, i.e., incorporating a full-solution forward model and a standard minimization algorithm in an iterative manner, has proven to be computationally intractable. A large variety of proposals for the reconstruction problem has been put forward, starting with simple backprojection methods such as found in x-ray tomography (see the review by Arridge[50]). However, the development has mostly focused on a perturbation approach. Consider the fluence rate $\phi_0(\mathbf{r}_s,\mathbf{r}_d)$ at the detector sites $\mathbf{r}_d$ due to sources at $\mathbf{r}_s$. Provided that a change in the optical properties μ_a and μ_s' is sufficiently small, expressed by $\delta\mathbf{p}$, the problem can be linearized so that the perturbed fluence rate is given by

$$\phi_1 = \phi_0 + \delta\phi \tag{4.10}$$

$$\delta\phi = \int K(\mathbf{r})\delta\mathbf{p}\,\mathrm{d}\,\mathbf{r}\,, \tag{4.11}$$

where K is a kernel defined by the forward problem[147,148]. This is the Born approximation. An alternative way of linearization is the Rytov approximation,

$$\phi_1 = \phi_0 \exp(\delta\phi)\,. \tag{4.12}$$

Thus, in the Rytov approximation, $\log(\phi)$ is linear. In terms of minimizing the ill-conditioned inverse, the Rytov approximation seems to be preferred by most authors[147-149]. The linear method can be used directly to determine changes of the optical properties in a medium, or used when there is a reference medium available with constant optical properties. This approach can also be thought of as taking only the first step in the iterative approach depicted in Fig. 4.2. It has been shown that it is not possible to obtain absolute quantitative information using non-iterative linearized methods[147]. The integral equation can be written on matrix form as

$$\delta\phi = \mathbf{J}\delta\mathbf{p} \tag{4.13}$$

where $\mathbf{J}$ is the Jacobian. The Jacobian can be calculated using the photon measurement density functions discussed in Sect. 3.2.14[65,89].

Equation (4.13) provides the way to calculate the update vector needed in the iterative algorithm in Fig. 4.2, to solve the non-linear problem. Methods where the Jacobian matrix is explicitly created and inverted are called Newton methods, of

which a typical example is the Levenberg-Marquardt method[44]. Rather than explicitly computing and inverting the Jacobian, which is computationally very costly, in some instances it is possible to calculate the gradient of the objective function directly for use in the minimization algorithm[50,61,148,150,151]. Arridge *et al*. have shown that using this gradient method and a FEM representation of the forward problem, the computations can be cut down significantly[50,151]. The limitation of this approach is that the type of measurement is restricted, since the fluence rate ϕ is never explicitly computed. In the FEM representation, the measurements are restricted to moments of the TPSF, i.e.:

$$\phi^{(n)} = \int_{-\infty}^{\infty} t^n \phi(t)\, \mathrm{d}t \,, \tag{4.14}$$

where $\phi^{(n)}$ represents the n^{th} moment. This method has been demonstrated several times, both for simulated and experimental data[50,150-155], and software is available for download[156].

So far in this treatment, the diffusion approximation has been taken for granted in terms of forward model for the reconstruction problem. Other methods have been explored, e.g., a cw discrete ordinates model have been implemented and demonstrated by Klose and Hielscher[48,49,157]. Considering the computational cost even of using diffusion models, however, it will likely take some time before more advanced forward methods become widely used. Inclusions of regions where the absorption is high or scattering is low present a problem for diffusion models. This has been addressed by some investigators, and hybrid models have been developed which deal with regions of low scattering using radiosity theory[158-160].

The ill-posed inverse implies that the solution is unstable with respect to small errors and noise in the measurement data. Also, the problem is usually under-determined. These issues are handled by the use of regularization methods. This is accomplished by adding a penalty term to the objective function to be minimized, which represents some *a priori* information[50]. Expressed in words, prior knowledge is for example information of the behavior of the solution. The nature of diffusive propagation causes all sharp features to be smoothed, so the regularization function forces the solution of μ_s' and μ_a to be smooth functions in space. This effectively introduces dependencies between the unknowns in the problem, and stabilizes the inverse.

5. Practical aspects and applications

5.1 Tissue optical properties

The work this thesis is based upon has mainly focused on tissue optics, and the following sections cover this topic in some detail, with the focus on the scattering structures in tissue on the cellular level, as well as the most important absorbing substances. The cells are the building stones of most biological tissues. From an optics perspective, the important features of the cells are their size, shape, refractive index in the various compartments, possible internal structures, and the abundance and distribution of absorbing substances. Different cell types may have very different properties, as we will see. The discussion will start with a review of the microscopic features of cells that affect scattering properties, and then continue with the absorption properties.

5.1.1 Scattering properties of tissues

The refractive index of tissues varies in a complicated manner on a microscopic level. Within the context of transport theory, a macroscopic, or bulk, refractive index is defined. For tissues, this can be measured by analyzing the Fresnel reflection off a tissue surface. The refractive index of most tissue types measured this way are in the range 1.38 – 1.41 at 633 nm[161]. A slight dispersion of 2 – 4% is present in the visible region.

As stated earlier, a detailed description of the complex refractive index at a microscopic level in tissues is unfeasible. Nevertheless, some important conclusions regarding the scattering characteristics can be drawn by a microscopic consideration. The cells and the intracellular matrix consist mostly of an aqueous solution of electrolytes and proteins. Other solutes such as sugars and alcohols are also present at lower concentrations. The main scattering features in tissues are the mitochondria[162], and in cells where they are present, lipid vesicles (fat droplets). The whole cell structure also contributes, but to a less extent[163]. Blood cells are an important special case, which will be discussed in more detail in Sect. 5.1.9. The cell nuclei add a surprisingly low contribution to the scattering, a fact that may be attributed to the low volume concentration of nucleic membranes and DNA[162,164]. However, Mourant *et al*. have shown that the DNA is a dominating contributor to scattering in large angles from the incident light beam[165]. A detailed review of the microscopic scattering features of tissue can be found in Ref. 120. The scattering properties of tissues are generally regarded to be fairly constant and invariant to physiological changes, as well as handling of tissue samples *in vitro*. One

important exception is fatty tissue, which can change its scattering radically if the fatty acids are allowed to crystallize if the temperature drops.

Many tissue types exhibit anisotropic structures, for example as a consequence of elongated cells that are oriented in a preferred direction. Examples include muscle fibers, bone, teeth[166], epithelial surfaces[167] and flowing blood. Anisotropic structures can induce polarization-altering effects such as birefringence and dichroism. Polarimetry of tissues has emerged as an intense area of research during the last few years, since it is hoped that more information on the tissue can be gathered. The Stokes parameters of several tissue types have been measured[168]. Polarization measurements of flowing blood were performed in Paper VI. Even when the tissue is isotropic, polarimetry can give useful information[169,170].

The spectral shape of the scattering coefficient and the *g*-factor are influenced by the microscopic features of the scattering. This means that by analyzing such spectra, it is possible to deduce information on the scattering structures. From considerations of single scatterers, we know that the scattering cross section increases as the size of the scatterer increases. Larger scatterers also lead to a more forward-favored scattering, i.e., higher *g*-factor. By comparing the shape of the μ_s spectrum with Mie calculations, a Mie equivalent scatterer size can be calculated. This was performed in Paper IV. The Mie equivalent size should not be interpreted as an in any way exact measure of the scatterer size, but it may serve as a rough estimate of the sizes of the scattering structures. Another way to extract information on the scattering structures from tissue surfaces has been explored by Perelman *et al*.[171]. The method relies on spectral measurements of the reflectance off the surface, and analyzing actual spectral oscillations of the Mie scattering from the topmost cell layers.

The recent developments in optical coherence tomography has provided a tool to obtain almost the resolution needed to perform *in-vivo* imaging at the cellular level, down to depths of a few hundred μm[172-175]. Optical coherence tomography is an interferometric technique where the imaging information is provided by comparing the path lengths of light reflected at different depths in the tissue, with that of the reference arm of the interferometer. The depth resolution is then defined by the coherence length of the light.

Knowledge of the details of scattering in tissue is important for the fundamental understanding. In most practical applications, the scattering coefficient is determined on a macroscopic basis, and the microscopic features are usually of less importance. There are, however, some situations where detailed understanding of the microscopic scattering is essential. Optical coherence tomography is one such method. Another typical example is blood, which can alter its scattering coefficient by up to 10% depending on the flowing conditions. This phenomenon cannot be

fully explained nor controlled without insight into the scattering characteristics of the blood cells at a microscopic level. This will be discussed more in Sect. 5.1.9, and is also the topic of Papers V and VI.

5.1.2 Absorption properties of tissues - chromophores

In the visible and NIR region, the main absorbers in soft tissues are water, hemoglobin, and lipids. Structural proteins such as collagen absorb mainly in the UV. In muscle tissue, myoglobin is a strong absorber in the visible. Mitochondrial chromophores, cytochromes, are abundant at lower concentrations, but because of their high extinction coefficients they may have strong a contribution to the absorption. In dark skin, melanin has a high absorption, although this is limited to a rather thin layer. These compounds comprise the main chromophores in soft tissues, and it is usually sufficient to include these in a spectroscopic consideration.

The absorption spectra of tissue chromophores presented in Sects. 5.1.3 – 5.1.7 are

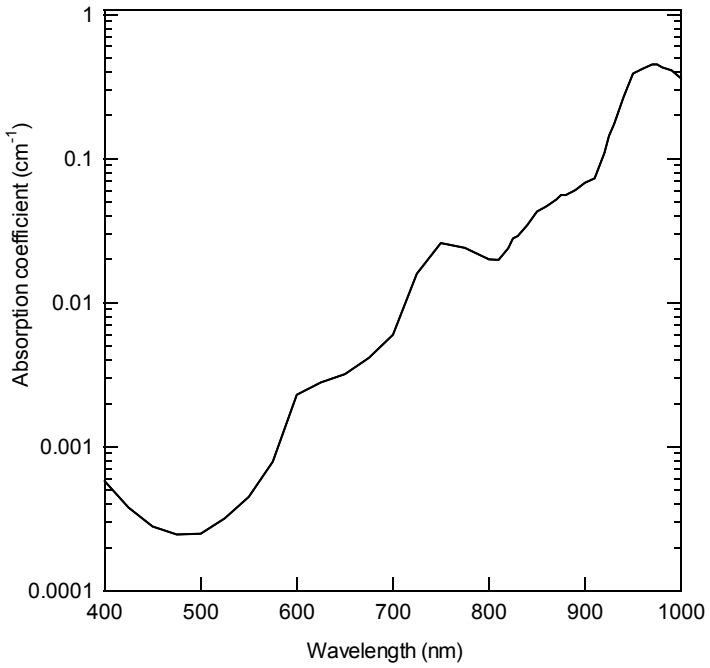

Fig. 5.1 Absorption coefficient of pure water. From Hale and Querry[176].

shown in units of the absorption coefficient, defined using the natural logarithm. To obtain the extinction coefficient, which is defined using $\log_{10}$, one must divide by $\ln(10) \approx 2.3026$.

5.1.3 Water

Water is present in all soft tissues to varying degree. Muscular tissue can consist of up to 3/4 water, while in adipose tissues the water content may only be 1/5. The absorption properties of water are slightly affected by the presence of various solutes, but this effect is typically so small that it can be neglected in tissue optics. An absorption spectrum of pure water is presented in Fig. 5.1. In the visible region, the absorption can be regarded as insignificant, but it becomes a dominant chromophore of most tissues above 900 nm with a peak at around 970 nm.

5.1.4 Hemoglobin and myoglobin

The physiological role of the heme proteins – hemoglobin (Hb) and myoglobin (Mb) – is to transport oxygen to the cells. Hemoglobin is a globular protein to which four heme groups are attached. In the center of each heme group sits an iron atom, which provides the oxygen binding properties. Myoglobin is abundant in muscle cells and act both as an oxygen transporter and as a storage compartment of oxygen for the working muscle cells. The myoglobin molecule is roughly the size one fourth of the hemoglobin molecule and carries only one heme group. The absorption spectra of the heme proteins are very similar, with strong bands in the UV, around 420 nm (the Soret band), and around 550 nm. The absorption bands are slightly shifted between myoglobin and hemoglobin, which allows differentiation of the two chromophores. Furthermore, the absorption differs markedly between the oxygenated and deoxygenated varieties (see Figs. 5.2 and 5.3), allowing measurement of the oxygenation state by means of spectroscopic methods. In the literature one often sees the use of the term “equivalent” with regard to the molar absorption coefficient of hemoglobin. One equivalent is ¼ of the molar absorption, since it refers to the absorption per heme group. In the spectra in Fig. 5.2 the true molar absorption coefficient is presented.

The molecular structure of the heme proteins, and thus both the functionality and absorption properties, are slightly different between species. For example, the Soret band is shifted from 556 nm for sperm whale myoglobin (Fig. 5.3) to 560 nm for the horse derivative[178]. The kinetics of the oxygen binding is also different. Human hemoglobin has a high oxygen affinity, and saturates with oxygen within seconds

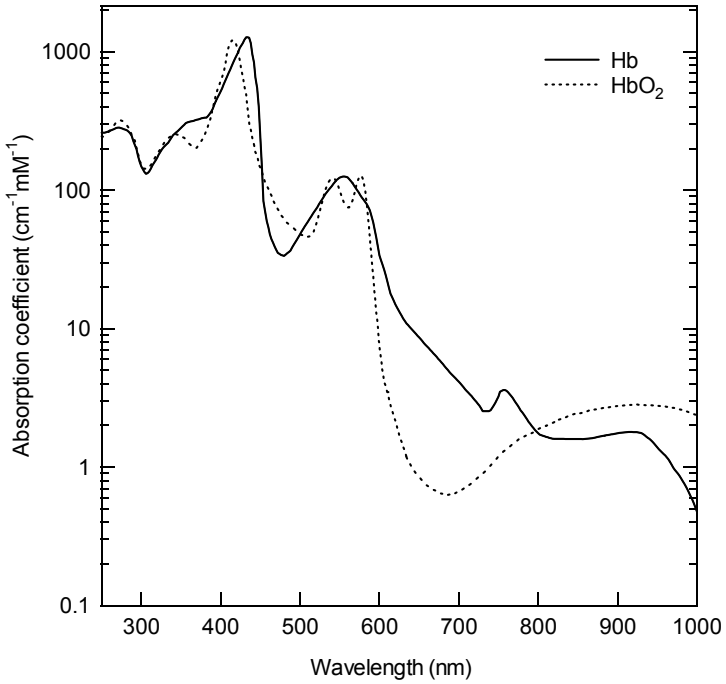

Fig. 5.2 Absorption coefficients of human Hb and HbO_2. Note that the spectra are presented in molar absorption rather than equivalents (see text). Data compiled by Prahl[177] from various sources.

when exposed to air. In comparison, bovine hemoglobin saturates very slowly and can be kept for minutes in air without noticeable effects[179].

In addition to the normal oxy and deoxy states described above, heme proteins may also be oxidized to form methemoglobin and metmyoglobin. In this process, the normal ferrous (Fe^{2+}) state oxidizes to the ferric (Fe^{3+}) state, and the oxygen binding properties are lost. Under normal physiological conditions the amount of oxidized heme proteins is low, around 1-2% for both hemoglobin and myoglobin. Pathological conditions can increase the oxidization, and it was shown in Paper IV that thermal coagulation of muscle tissue will induce the formation of metmyoglobin. The ferric derivatives have different absorption spectra than the ferrous, as shown in Fig. 5.3 for metmyoglobin.

In the red and NIR region, the spectra of hemoglobin and myoglobin are virtually identical. The implication of this is that it is impossible to distinguish between the two using transillumination methods. In such cases, *a priori* knowledge is

necessary to quantify the abundance of hemoglobin and myoglobin in the tissue. Typically, myoglobin is dominant in muscle tissue with a ratio around 10:1 compared with hemoglobin, while hemoglobin is the only heme protein in most other tissue types[178]. In muscle tissue, the concentration of myoglobin is around 5 mg/g[180]. The hemoglobin content depends on the blood perfusion in the tissue. Whole blood normally has a hemoglobin concentration of 7.5 – 10 mM.

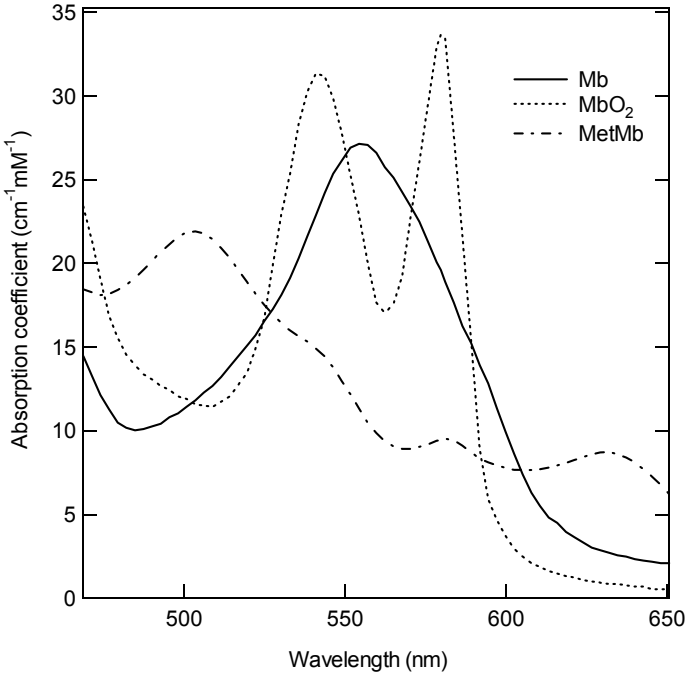

Fig. 5.3 Molar absorption coefficients of Mb, MbO2 and MetMb from sperm whale. Adapted from Antonini and Brunori[178].

5.1.5 Lipids

Lipids are present in adipose tissue, while the content in other tissues is low or non-existent. In adipose tissue the concentration amounts to around 70%. A typical lipid spectrum is shown in Fig. 5.4. Different types of fat have similar spectra. Like water, the lipid absorption can be neglected in the visible, but becomes significant in the NIR with a low peak at 760 nm and a strong peak at around 930 nm. In humans, adipose tissue appears yellowish to the eye due to β-carotene dissolved in the lipids. The absorption spectrum of β-carotene is also shown in Fig. 5.4.

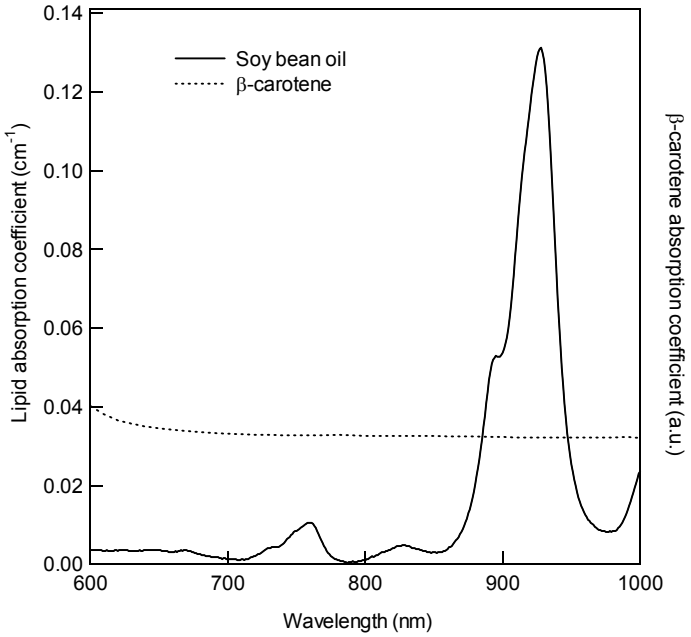

Fig. 5.4 Absorption coefficients of lipid and β-carotene. The β-carotene spectrum is not shown to scale. From Eker[181].

5.1.6 Melanin

Melanin is the dark pigment present in skin, hair, and the iris. It is synthesized by organelles called melanosomes. Melanin cannot be refined in its pure form, since it is insoluble, and the chemical structure becomes altered by extraction. Jacques and McAuliffe have investigated the absorption coefficient of the melanosomes[182], and have presented an approximate empirical formula[183]:

$$\mu_a = 1.70 \cdot 10^{12} \lambda^{-3.48} \ \text{cm}^{-1} \tag{5.1}$$

where λ is in nm. This spectrum is shown in Fig. 5.5. The spectrum presents no sharp features, and since the melanin is present only in a thin layer, it acts as a gray filter when measurements through the skin are performed. This can be a problem when performing measurements on persons with very dark skin. Melanin is also a problem for optical detection of malignant melanoma, often containing melanin in high concentration, since most of the light is then absorbed in the lesion.

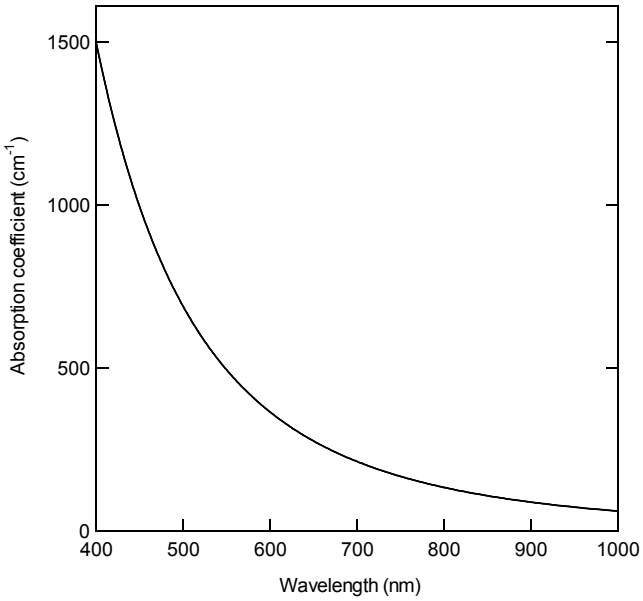

Fig. 5.5 Absorption coefficient of melanosomes in skin tissue. The spectrum is calculated with the emprical formula given by Jacques[183], see text.

5.1.7 Mitochondrial chromophores – cytochromes

In adipose tissue, hemoglobin, lipids and water constitute the relevant chromophores in the NIR region. The same is usually true for tumor tissue. Tissues that have high mitochondrial content may have a significant contribution by other chromophores to the absorption. The respiratory chain in the mitochondria consists of a number of organometallic proteins that have high absorption, called cytochromes. The most important from a spectroscopic point of view are cytochromes *c*, *b* and *c*-oxidase (the latter sometimes denoted aa_3)[184]. The spectral properties of the cytochromes are strongly affected by whether the molecule is in the oxidized or reduced state. Absorption spectra of these cytochromes are shown in Fig. 5.6. *In-vivo* measurements of the absorption of cytochrome *c* have been attempted in the NIR region as a means to monitor the oxygenation state of neonatal brain tissue[184]. Mitochondria are present in most cells, but in some tissue types the abundance is higher. For example, in non-blood perfused liver tissue, 50% of the absorption in the NIR is attributed to cytochromes[185].

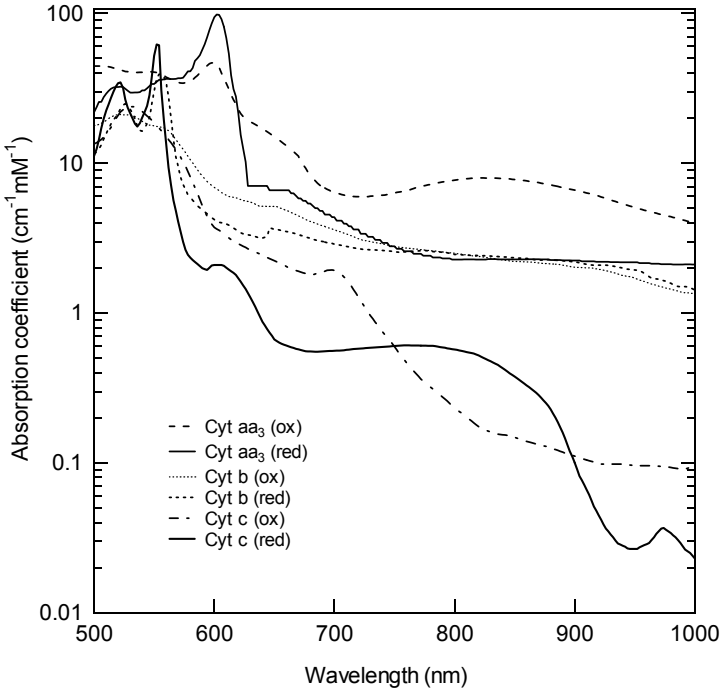

Fig. 5.6 Molar absorption coefficients of cytochromes *b*, *c* and *c*-oxidase (aa_3). From Cope[184].

5.1.8 Discussion – absorption properties of tissue

The region approximately 650 – 1000 nm is sometimes called the optical window of tissue, due to the low overall absorption in this region. The scattering is also lower in this region compared with the UV and visible. Hemoglobin and myoglobin are, in practice, indistinguishable in the region. The oxygen saturation may, however, be determined by using in principle only two wavelengths. This is utilized in pulse oximetry[186,187], and it is a major goal for most proposed modalities for transillumination. The oxygen saturation gives important information of the physiology of the tissue, especially if it can be combined with imaging and/or analysis of dynamic changes in oxygen saturation. For example, it is generally believed that the oxygen saturation differs markedly inside tumors as compared with the surrounding tissue. Various methods to determine the oxygen saturation from spectral measurements have been presented in the literature[105,106,131,188-198].

By adding more wavelengths to the analysis, it is possible to characterize more substances in the tissue. The aim of optical tomography of soft tissues is to quantify the concentrations of the four spectrally relevant chromophores in the optical window: oxy- and deoxyhemoglobin, water, and lipids. To achieve this, in principle four wavelengths are needed, e.g., around 660 nm, 800 nm, 920 nm and 970 nm. It is hoped that the information given by the state of oxygen saturation, together with the concentrations of water and lipids, the tissue morphology, and possible dynamic changes, will provide enough information to diagnose diseases such as malignant lesions.

The distribution of chromophores on a small-scale level can be an important factor for the overall absorption properties. The chromophores are, as we have seen, often confined to discrete compartments on a cellular level. Also, the capillary network of blood vessels is a highly inhomogeneous structure on a microscopic level. When chromophores are accumulated in certain regions, shielding effects occur, resulting in a reduced overall absorption. Since transport theory assumes homogeneous distribution of absorbers on a microscopic level, the deduced absorption coefficient tends to be underestimated. Thus, the same volume concentration of, e.g., hemoglobin in tissue results in different absorption depending on how the substance is distributed. This phenomenon has been studied by several authors, and corrected transport models have also been developed[106,199-202]. As a somewhat simplified explanation, this effect can also describe the increased absorption coefficient of flowing blood, as compared with non-flowing blood, reported in Paper V. In non-flowing blood, the red blood cells tend to form aggregates, and shielding effect thus occur. However, in whole blood, the scattering effects are too complicated for this description to be complete, as is discussed in more detail in Paper V.

5.1.9 Optical properties of blood

At first glance, blood appears to have deceivingly simple optical properties. The scattering and absorption are largely governed by the red blood cells (RBCs): their refractive index in relation to that of the surrounding plasma, and their absorption due to hemoglobin. The RBCs are virtually identical, biconcave discs with the dimensions approximately 2×8 μm. Unlike most other cells, they have no nucleus, so the scattering occurs only at the interface defined by the outer cell membrane. It has been shown that the scattering of the membrane itself is negligible[203,204], meaning that only the size, shape and index mismatch are the relevant parameters. The refractive index of blood plasma has been measured to 1.345[205], and the relative refractive index of the RBC to 1.04 – 1.05 at 633 nm[206].

The complexity of blood optics comes from the fact that it is a moving liquid with a very dense concentration of RBCs. Many studies have concluded that the light transmission through flowing blood can change as much as 30% depending on the flow rate. When attempting quantitative optical measurements of blood, such a large variation is not acceptable unless its mechanisms are understood and can be controlled. The optical properties of blood in motion was investigated in Papers V and VI. The key issue is understanding the microscopic geometry of the RBCs in a flow field, both in terms of deformation and their orientation, and how this relates to the light scattering and absorption. Detailed studies of the behavior of RBCs in flowing blood were performed in the 1960s and 70s, and have revealed several important observations about the morphology of the RBCs. Many experiments were conducted on diluted blood, because of the easier experimental requirements. However, both the rheological and optical properties are very different for whole blood, which has a volume density of about 40% RBCs.

To get reliable data for whole blood, different experimental techniques have been used, e.g., snap freezing blood vessels with liquid nitrogen[207], or microscopic photography of thin layers of blood subjected to shear flow in viscometers[208-212]. The basic assumption made in the latter method is that it is the shearing in the flow field that gives rise to changes in RBC morphology. For a liquid flowing through a duct, the shear rate is the velocity gradient perpendicular to the duct wall. In a circular duct, the velocity profile is parabolic for laminar flow of a Newtonian liquid (Poiseuille flow), and the shear rate varies linearly with the maximum values at the wall. Blood is generally considered a non-Newtonian liquid, however, and propagates with a blunted parabolic profile, which becomes a flat "plug" if the diameter of the duct is small enough[209,213,214]. For ducts with a diameter larger than 100 μm, the velocity profile is fairly well approximated with the parabolic. The shear rate for a duct of circular cross section, with radius R, is given by

$$G = \frac{4Q}{\pi R^2 r} \tag{5.2}$$

where Q is the volumetric flow and r is the radial distance from the central axis. With this assumption of shear rate as the background, by studying the behavior of RBCs in a viscometer one can emulate the shear rate in a duct at different radial distances from the central axis.

Another method to study high concentrations of cells is by preparing ghost cells, which are index matched with the surrounding liquid. These become invisible in the microscope, but retain their mechanical properties. By adding a small amount of tracer cells with the original optical properties, one can study the morphology under a microscope[209]. These methods have revealed that the RBCs behave much like liquid droplets dispersed in the blood plasma, rather than as rigid particles. At

high shear rate, the RBCs tend to elongate and align in the direction of the shear. At low or zero shear rate the situation is also complicated. The RBCs tend to form aggregates in various forms, e.g. the famous rouleaux, in ways that are governed by the biochemistry of the cell membrane surfaces and the composition of the plasma. In Fig. 5.7, sketches of aggregated blood cells are depicted at various shear rates. In normal human blood, almost all aggregates become dispersed at shear rates above 46 s^{-1} [208,210]. However, even at higher shear rates, small roleaux of 4 – 10 cells may resist and tumble along with the single cells. The aggregation properties of blood are the reason for the nonlinear viscosity as the shear rate increases, and thus the fact that blood may be described as thixotropic, i.e., the viscosity is higher at low shear rate. Aggregation also affects the scattering properties strongly, as was seen in Paper V.

The morphology of RBCs can also be studied using indirect methods such as measurements of the angular distribution of scattered light from thin layers – ektacytometry[205]. Several attempts to describe the scattering from individual RBCs have been made. By using T-matrix computations, it is possible to model the effects of both deformation and orientation of single RBCs[9]. However, because the RBCs are so densely packed, single cell models fail to accurately predict the

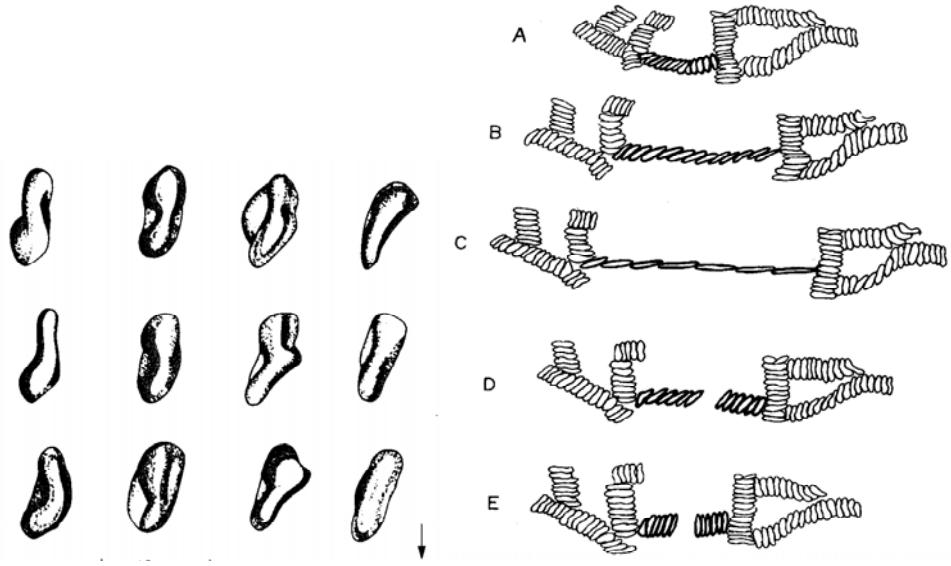

Fig. 5.7 Sketches of RBCs. In (a), tracings of of deformation and orientation are shown at 75 ms intervals. The direction of flow and time axis is downward in the picture; four different RBCs are shown. The shear rate was approximately 7 s^{-1}. From Ref. 209. In (b), aggregation of RBCs in rouleau networks at low, increasing, shear rate are shown. The shear rates are: A, 2.3 s^{-1}; B, 23 s^{-1}; C, 46 s^{-1}; D, E, >46 s^{-1}. From Ref. 208.

scattering of whole blood. In Paper V, it was demonstrated that qualitative predictions of the scattering from whole blood are possible using T-matrix theory, and for the absorption one can almost draw quantitative conclusions.

A full understanding of the scattering properties of blood is of great importance. Such knowledge is a necessary requirement for *in-vivo* spectroscopical measurements of anything else than oxygen saturation. Blood analysis is a cornerstone of modern health care, and more efficient measurement methods would have both benefits for the economy as well as for the patients and medical staff. A long-sought technique is non-invasive monitoring of blood glucose in diabetics, where optical sensors in one proposed method. Although *in-vivo* transillumination measurements of blood may still be unrealistic for some time, hemodialysis machines are an area where the developments have lead to implementation of optical sensors.

5.2 Tissue phantoms

Artificial samples are important for validation of light propagation models and systems for measuring the optical properties, and in some cases also for calibration. The ideal phantom material should mimic the optical properties of tissue in terms of scattering coefficient, anisotropy factor, absorption coefficient and refractive index, over the entire spectral range of interest. It should also be possible to check the optical properties to high accuracy using independent methods, preferably based on fundamental theory such as Mie calculations. Moreover, the material should be easy to make and shape, and be robust and stable.

In the field of tissue optics, most phantoms that have been used have been based on either water or resins such as polyester. In the following two sections these materials will be discussed in more detail, to see how close they come to the ideal phantom material.

5.2.1 Water-based phantoms

Perhaps the simplest and most widely available phantom material is ordinary milk[215]. The scattering in milk comes from fat droplets and proteins suspended in the water. Absorption can be obtained by adding dyes or ink. In pure milk absorption is dominated by the water, which has low absorption in the visible spectrum but becomes increasingly large in the NIR. The relatively large absorption at 970 nm is a problem for water-based phantoms, since the absorption of pure water can actually be higher than that of tissue, especially if the tissue is

low in water content such as fatty tissue or skin. Water phantoms are, for this reason, not ideal for wavelengths above 900 nm.

Milk has obvious disadvantages as a phantom material, since its optical properties are not well defined and are not possible to verify by theory. Similar to milk in terms of composition is Intralipid, which is perhaps the mostly used phantom material in the literature[107,113,121,216-219]. Intralipid is a nutrition liquid which is intended for intravenous use. The quality control is therefore much higher than for milk, and since it is sterile it can be kept longer. Addition of penicillin prevents bacterial growth. It should be noted, though, that it is not intended as an optical product and the optical properties are still not particularly well defined. Van Staveren *et al*. gave approximate formulae for the scattering properties of Intralipid-10%[216]:

$$\mu_s = 0.016\lambda^{-2.4}\,\mathrm{mm^{-1}ml^{-1}l} \tag{5.3}$$

$$g = 1.1 - 0.58\lambda \tag{5.4}$$

where the wavelength λ is in micrometers. Experience shows that the variation can be in the order of 20% from the values predicted with this formula, possibly more. Liquid phantoms may be easy to work with, but make it difficult to introduce inhomogeneities. Solid Intralipid phantoms can be made by adding agar gel[219]. When adding an absorber, one has to be careful not to use one that changes the scattering properties. Generally, acidic dyes can cause the fat emulsion of the Intralipid to split. Food dyes are convenient to work with in the visible region, but the region above 800 nm is more difficult. Carbon-based inks absorb in the NIR, but they also add some scattering, which makes absolute prediction of the absorption difficult[220].

The best water-based phantom is a suspension of monodisperse microspheres, usually of polystyrene. Since the size of the scattering spheres is known, it is possible to use Mie theory of calculate the scattering properties. By choosing the right size, the *g*-factor can be controlled, something that is impossible with Intralipid. Unfortunately, monodisperse microspheres are expensive, and large volume phantoms are not realistic. Microsphere suspensions keep longer than Intralipid, but have a limited shelf life due to settling and aggregation of the spheres (in the order of months).

5.2.2 Resin phantoms

For realistic phantoms in the region above 900 nm, other materials than water are required. In addition to solving the absorption problem, plastics are attractive for

other reasons as well. Plastics are stable and robust, and solid phantoms make for the possibility of complicated shapes and embedded inhomogeneities. The disadvantages are mainly the increased complexity in making them, and that it is not possible to alter the properties of a phantom once it has set. Thermoplastics such as PMMA, although optically good, are not suitable because of the complicated production process. Curing plastics such as polyester and epoxy resins have been used as phantom material, and are easy to work with in the laboratory since the scattering and absorption agents can be mixed with the liquid resin. Polyester and epoxy have similar optical and mechanical properties[221,222], but for large volumes (about 0.5 liter) epoxy is preferred since the heat from the exothermic process in the curing of the polyester can cause cracking.

As scatterers, the most common material is TiO_2. This is an inexpensive and readily available material, suitable where a tissue-like *g*-factor is not necessary or the reduced scattering is the only important parameter. To control the *g*-factor, silica microspheres can be used as scatterers[222], although at a considerably higher cost. Many absorbing dyes are available in the visible region, but in the NIR the situation is different. One dye, Pro Jet 900 NP, has proved compatible with both polyester and epoxy, and is effective up to around 900 nm[222]. Above 900 nm, there is a small selection of commercially available laser and printing dyes[223,224], but the experience is that all of these tend to react with the resin and change their absorption properties, usually by almost complete bleaching. The simplest solution to this problem is to use a broadband absorbing pigment such as carbon black, which is available everywhere in the form of toner for copying machines.

5.2.3 Refractive index

In phantoms with values of μ_s typical to tissues, the bulk material (water or resin) amounts to 99% or more. The refractive index is therefore close to 1.33 in water phantoms and 1.55 in resin phantoms. For validation purposes, the difference in refractive index compared with real tissue may not be of concern, since a model that is accurate for $n = 1.33$ or 1.55 is likely to be so for $n = 1.4$ (typical of tissues) as well. For calibration purposes this can be a matter that has to be taken into consideration, however, especially if time-resolved measurements are performed.

5.3 Instrumentation

The instrumentation needed to measure the optical properties of turbid media depends on the type of measurement. In this section, some of the most common techniques are reviewed. The discussion follows the same structure as in Chapter 4,

The inverse problem. In general, the complexity of the instrumentation increases going from cw measurement, over frequency-resolved measurements, to time-resolved measurements.

5.3.1 Cw measurement instruments

Spatially resolved diffuse reflectance measurements (cf. Sect. 4.1.1) can be performed in either contact mode or as image reflectometry. As light sources, either halogen lamps or Xe lamps are often employed, or light from LEDs or diode lasers. Broadband lamps require the use of some spectroscopic filtering at the detection side, while diode lasers are intrinsically narrowband, but instead require the use of several units to cover many wavelengths. A diode-laser based, contact mode system was used in Paper II. The probe head in this case consists of a single source fiber in the center, and the detection is performed at different radial distances by means of concentrically arranged rings of optical fiber bundles. A technical description of this system can be found in Ref. 102.

Examples of other fiber probe contact mode systems are those designed by Wilson *et al*.[225] and by Sterenborg and co-workers[105], also intended for *in-vivo* measurements on the skin. These systems utilize a white light source, and a spectrometer/CCD camera for detection.

In image reflectometry, the surface is illuminated at one point, and a camera records the diffuse reflectance pattern around the light spot. Such a system is described in Ref. 107, where an imaging Fourier-transform interferometer was used to provide both imaging and spectral resolution. One possible advantage of image reflectometry over contact mode systems is that the surface is left undisturbed, which can be a problem for skin measurements because the blood flow is restricted by the pressure applied by the probe head. The drawback of image reflectometry is that it may be more difficult to keep the object still in relation to the instrument during the acquisition. To make image reflectometry more robust with respect to small inhomogeneities, it is also possible to illuminate the surface with a structured pattern instead of at a single point. The data evaluation then requires some additional processing which typically involves Fourier transformation of the image of the reflected pattern[226].

The general advantage of cw measurements is the simplicity and robustness of the instrumentation. The technique has some drawbacks as compared with frequency- or time-resolved measurements, as was discussed in Sect. 4.1.2. A thorough treatment on cw measurements can be found in Ref. 129.

5.3.2 Frequency-resolved instruments

Frequency-modulated diode lasers are the usual choice of light source for frequency-resolved instruments. The modulation is performed at radio frequencies up to around 1 GHz. Avalanche photodiodes are typically used as detectors. The light is most often delivered to the medium by means of a multimode optical fiber, and the detected light is guided to the detector by a similar fiber or a fiber bundle. Thanks to the inherent homodyne detection implemented by this scheme, frequency-resolved measurements can yield very low-noise signals. The low-noise data is advantage compared with time-resolved measurements, but on the other hand, the information content is lower unless the measurements are performed at many modulation frequencies. The maximum bandwidth is also usually lower for a frequency-resolved system than a time-resolved, which is important especially if the source and detector fibers are close. Close fiber spacing usually means <1 cm in biological tissues. A comparison between time-resolved and frequency-resolved systems can be found in Ref. 227. Frequency-resolved instruments for tissue optics measurements have been built by several groups[229-234].

5.3.3 Time-resolved instruments

Time-resolved measurements of turbid media were pioneered in the middle 1980s, and first utilized mode-locked Ar-ion lasers and dye lasers that produced picosecond pulses as light sources[235,236]. Since then, a multitude of pulsed lasers have been used, e.g., mode-locked Ti:sapphire lasers[237], fiber lasers[238], and diode lasers[136,141,142]. The requirement on the pulse length depends on the application, but for tissue, at short source-detector distances, better than 100 ps (corresponding to 10 GHz bandwidth) is usually necessary. At longer distances, approximately >2 cm, pulse lengths of up to 0.5 – 1 ns can be tolerated. The requirement is that the width of the temporal point-spread function (TPSF) is larger than the width of the injected pulses. (Here, the TPSF denotes the impulse response function of the medium. Often, the term TPSF is used for the actual measured curve, which here represents the TPSF convolved with the instrument response function).

The instrument response function is determined by the laser pulse length, and the broadening in the instrument: mode dispersion in optical fibers, broadening in the detector, time resolution and jitter in the electronics, etc. If long fibers are used, approximately > 1 m, they should be of gradient index type to eliminate pulse broadening by mode dispersion. Time-resolved detection can be achieved in a number of ways. The most common detector is probably a high-bandwidth photomultiplier tube (PMT). These can have impulse response times down to about 0.5 ns. With direct sampling electronics or boxcar integrators, time-resolution of this order can be achieved. Kerr shutters have also been employed, but suffer from

poor dynamic range[239]. The most common technique, however, is time-correlated single-photon counting (TCSPC). This method, illustrated in Fig. 5.8, is based on single photon statistics. The TCSPC method works at very low intensity levels, where individual photons are detected. It has advantages in terms of increased time resolution, dynamic range, and sensitivity.

When a pulse from the detector arrives, corresponding to one detected photon, this serves as a trigger pulse for the time-to-amplitude converter. When the pulse triggers the converter, an internal clock is started. The clock stops when the photodiode gives an electric pulse directly from the input light pulses, or a corresponding synchronizing signal from the laser driver. The time difference is converted to an electric pulse with an amplitude that is directly proportional to the time difference. This pulse is fed to a multichannel analyzer which converts the pulse amplitude to a channel number, which is then stored in a computer memory. The process is repeated, and each time a photon is detected it will add one count to one of the channels. Eventually, a histogram representing the shape in time of the signal forms. The probability of two or more photons reaching the detector at the same time must be low, since a second photon from the same laser pulse will not be counted. This would skew the distribution towards early times, the so-called pile-up effect. If the probability of detecting one photon per laser shot is kept below 1:30, the pile-up effect becomes negligible[240].

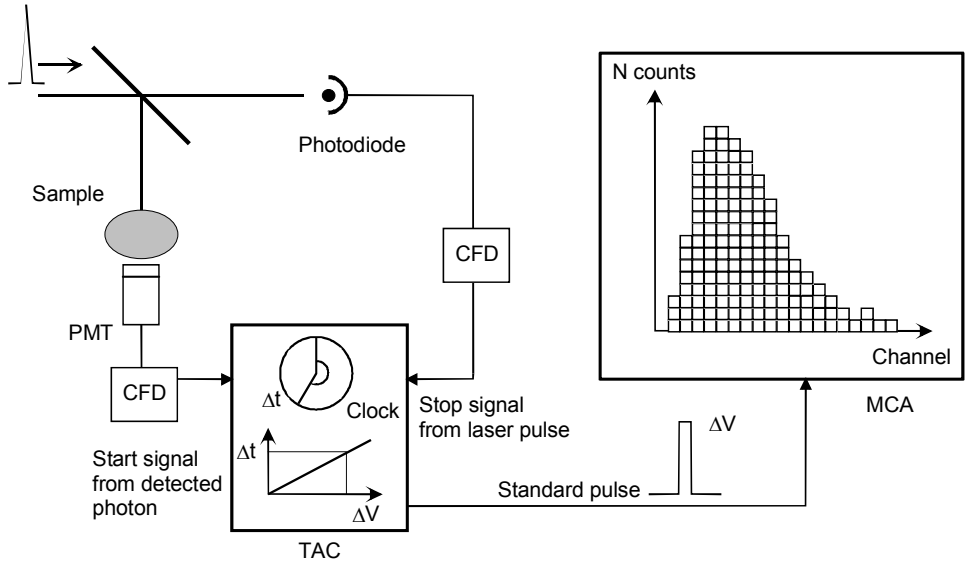

Fig. 5.8 The principle of time-correlated single-photon counting. Abbreviations used in the figure: PMT- photomultiplier tube, CFD – constant fraction discriminator, TAC – time-to-amplitude converter, MCA – multichannel analyzer. See the text for an explanation.

A typical mode-locked Ti:sapphire laser or pulsed diode laser may have a repetition rate of 80 MHz, so the count rate can easily exceed 1 MHz and the system is still in the single-photon counting mode. Since the measurement is reduced to binary mode (photon or no photon), the dynamic range of the detector is not an issue. In the same way, it is only necessary to know when in time the pulses arrive, which renders the shape of the pulses largely irrelevant. A constant fraction discriminator is used to accurately determine the arrival times of the pulses, independently of their amplitude, and the temporal resolution of the measurement can be 1/10 that of the rise time of the detector, or a few tens of picoseconds.

To be able to keep count rates as high as 1 MHz or above, the dead time of the detection system is an important parameter. The dead time for a PMT is largely determined by the transit time of the electrons. To minimize the transit time, special PMTs are often used which are equipped with a microchannel plate to shorten the distances the electrons have to travel inside the detector.

The sensitivity of the TCSPC method is limited mainly by the dark count rate of the detector. If the limit is defined as an signal-to-noise (SN) ratio of 1, the sensitivity can be written as

$$S = \frac{1}{Q}\sqrt{\frac{R_d N_c}{T}} \tag{5.5}$$

where R_d is the dark count rate, N_c is the number of time channels, T is the overall measurement time, and Q is the quantum efficiency of the detector[241]. The detector is often cooled to reduce the dark count rate and thus obtain a better sensitivity. The accuracy of the measurement is directly determined by the counting statistics, where the noise per time channel is given by the usual expression $N^{1/2}$ for N counts. Since it is usually important to keep the acquisition time to a minimum, the SN ratio is often worse than for frequency-resolved measurements. Instruments based on the TCSPC technique have been developed by several groups[136,141,238], and was also used in Papers II and III.

Detection in the NIR region is a problem for TCSPC measurements, at least above 900 nm. Standard multialkali photocathodes have good sensitivity up to ~800 nm, but it drops off rapidly at longer wavelengths[242]. Ag-O-Cs (S-1) cathodes are available, which are sensitive up to 1200 nm, but their sensitivity is, at best, an order of magnitude lower at shorter wavelengths. The latest InP/InGaAs cathodes expand the sensitivity out to 1700 nm, but the detector requires liquid nitrogen cooling, have a short life span, and is also considerably more expensive[242]. The region 900 – 1000 nm is interesting in tissue optics because of the potential of measuring lipid and water content in the tissue (cf. Sect. 5.1.8). At present, GaAs

cathode detectors sensitive in this region are available, but the instrument response function of a TCSPC system with such a detector is not better than in the order of 0.5 ns[141].

Avalanche photodiodes are another option, but they too have a poor time resolution. The region above 1000 nm is virtually unexplored with time-resolved measurements, and is an interesting object for future research. An interesting potential detector type for TCSPC systems are the emerging superconducting detectors[243,244]. This detector type is based on a superconducting material, which heats up slightly upon absorbing photons, and momentarily induces a detectable electrical resistance. These detectors function at NIR wavelengths, have a high bandwidth, and negligible dark counts, i.e., TCSPC measurements with virtually unlimited sensitivity would be possible. The superconducting detectors are, however, at present too small (10×10 μm) to be practical for TCSPC instruments.

Another option to reach very good time-resolution is the streak camera[240,245,246]. Time-resolution better than 1 ps can be achieved, but the dynamic range of the streak camera is not as good as for TCSPC systems. Streak cameras are often combined with spectrometers, and by using white-light pulses spectroscopic information can be obtained[246].

Gated CCD cameras have also been used to obtain a time-resolved detection system, and have the advantage of yielding parallel measurements. The time-resolution is not great, however, in the order of 0.5 ns[247].

5.3.4 Optical tomography instruments

Instruments for optical tomography are essentially parallel, or scanning, versions of one of the instrument types described in the previous sections. The practical difficulties of constructing such a system can be great, and the number of free parameters is large. The design must be a compromise between engineering considerations, patient comfort, and the optimal measurement in terms of reconstruction. An early optical tomograph, based on cw measurements and intended for optical mammography (breast cancer detection, cf. Sect. 5.4), was built at Philips[248]. Other cw systems have been built more recently[249,250], and have the advantage of being relatively simple, and that large quantities of data can be acquired in short time. The drawback of cw systems is that image reconstruction is hampered by the limited information in the intensity measurement (cf. Sect. 4.5).

Frequency-resolved optical tomography was initiated by Gratton *et al*.[251]. An early commercial attempt of a scanning, frequency-resolved optical mammography system was built at Carl Zeiss[252,253]. A contemporary instrument was designed at

Siemens, but details and results have not been widely published. Both companies have now abandoned development in the area. Other systems have later been built by several groups[230-234], and designs for new generation systems are presently being pursued by many groups, primarily in the United States. Some of these systems are combined cw/frequency-resolved instruments. Bevilaqua *et al*. used a white cw light source to provide additional spectral information[230]. Another advantage of the combined instrument is that dynamic changes can be monitored thanks to the short acquisition time and simple reconstruction of cw data, while the frequency-resolved data yields information of the absolute optical properties[231].

Time-resolved scanning mammographs, intended for transillumination of breasts, have been built for clinical use[136,141,254]. Currently, these systems are not used for true reconstruction of the optical properties, but the measurement protocol could in principle be modified to accommodate a wider range of projections which would allow tomographic reconstruction. A time-resolved 32-channel optical tomography system has been constructed by the group of Delpy[238], and has been used for monitoring of oxygen saturation in neonatal brain[255], the forearm[154], optical mammography for detection of breast cancer[256], and extensive phantom studies[151,152,155,257]. Another fully tomographic system, allowing parallel detection in eight channels, has been built by Chance and collaborators[258,259].

5.4 Optical mammography – a diagnostic application

Early on, breast cancer detection was identified as one of the most promising goals of optical tomography in medicine[142]. The female breast is easily accessed for a tomography system, and although the tissue structure is by no means homogeneous, it is still more homogeneous than many other organs. A major motivation for optical mammography is that current diagnostic modalities are less than perfect in many respects. Conventional x-ray mammography suffers from poor contrast, and physicians are forced to look for subtle morphological variation or secondary effects such as microcalcification. The efficacy of screening programs has been debated, and there is also a real statistical risk of inducing cancer in a small number of cases due to the ionizing nature of x-rays. Sonographic examinations have been proposed, but have so far emerged rather as a complement to x-rays than as an alternative. Magnetic resonance imaging is a perfect method for structural imaging, but without injected contrast agents to provide functional information it has proved difficult to distinguish malignant and benign lesions. It is also a costly technique.

Simple schemes for transillumination of the breast using lamps and photographic film or video cameras have been tried since the 1920s, but all these attempts

proved to be inferior to conventional x-ray mammography[260]. In terms of resolution, optical mammography can never hope to compete with x-rays. It expected that the best obtainable resolution for deep tissue structures is in the order of 0.5 – 1 cm. The advantage is instead hoped to be better contrast, and the ability to provide functional imaging, e.g., a different oxygen saturation in malignant lesions can serve as a distinct marker.

Many of the optical tomography systems described in the previous section were designed with optical mammography as a primary objective[136,141,231,233,248,251,253,254]. In addition to technical developments, an important area of research is understanding the scattering and absorption properties of various tissue types, and how these are linked to physiological parameters influenced by for example age and hormonal cycle. Clinical trials are ongoing in both Europe and the United States[141,231,256,261-267]. One company specializing in development of optical mammography is active in Fort Lauderdale, Florida[268], but their results have not been widely published in the scientific literature.

5.5 Atmospheric optics – remote sensing of trace gases

The primary application of spectroscopic techniques in atmospheric optics is remote sensing of trace gases in the atmosphere. Remote sensing techniques can be either passive, utilizing the natural light directly or indirectly from the sun, or active, utilizing for example lasers as light sources. Passive techniques are attractive because of the simplicity of the instrumentation, but having control of the natural light source can be problematic. Among the important trace gases from a remote sensing perspective we find SO_2, NO_2, O_3, and numerous hydrocarbons. Hydrocarbons have strong characteristic absorption bands in the infrared, where the scattering in the atmosphere usually is negligible. Spectroscopy of the other gases, however, is performed at shorter wavelengths, in the visible region for NO_2, and UV for SO_2 and O_3. In this region, both the Rayleigh scattering from the air and scattering from dispersed aerosols can be significant.

In Paper VII, both passive and active techniques were applied to measure the emission of SO_2 from the volcano Mt. Etna in Italy. The passive instruments were a differential absorption spectroscopy (DOAS) system[240,269], and a correlation spectroscopy (COSPEC) instrument[240,270]. A lidar system (light detection and ranging) was used to provide active measurements, using a pulsed dye laser as the light source. A differential absorption lidar (DIAL) measurement scheme was applied, in which the absorption on and off one absorption peak of the gas is measured[240,271]. Passive systems can operate in either up-looking or sun-tracking mode. In the former mode, the light is provided by the blue sky above the

instrument, and the trace gas is assumed to linger between the detector and the scattering volume in the atmosphere. In the latter mode, the sun disc directly provides the light. Passive instruments usually have to be calibrated for each measurement, due to the variation in solar elevation, background absorption, cloud formation etc.

The passive instruments operate at around 300 nm, where the atmospheric scattering is strong enough to disqualify the assumption of a clear medium between the light source and the detector, especially in the up-looking mode. This mode is preferred because of the simplicity. The path-length of the detected light through the gas is then no longer trivial to predict. If a line-of-sight path-length is assumed (the Beer-Lambert law), the measured gas concentration will be systematically offset; usually it is overestimated due to a longer actual path-length in the scattering medium.

The scattering in the atmosphere can be divided in two parts, Rayleigh-type scattering from the air molecules and Mie-type scattering from aerosols. The Rayleigh contribution is determined by the well-known expression for the scattered energy *I*:

$$I = \frac{16\pi^4 c}{3\lambda^4}\alpha^2 \mathbf{E}_0{}^2, \tag{5.6}$$

where α is the polarizability of the molecule and $\mathbf{E}_0$ is the amplitude of the electric field. The real atmosphere deviates slightly from this theoretical formula. An empirical formula for the Rayleigh cross section in the region 200 – 550 nm was given by Nicolet[272]:

$$\sigma_R = 4.02 \cdot 10^{-32} \lambda^{4+x} \ \mathrm{m}^2$$

$$x = 0.389\lambda + \frac{0.09426}{\lambda} - 0.3228, \tag{5.7}$$

where λ is expressed in μm. To obtain the scattering coefficient, the number density of air molecules is needed. This depends on the air density which is a function of air pressure and the altitude. One can assume that it follows the standard atmosphere model[273]. This calculation was performed to obtain the scattering coefficients in Paper VII.

The contribution of aerosols to the scattering is high in the lowest layers of the troposphere. The exact composition of the aerosol layer varies strongly depending on climate zone, weather conditions, the ground conditions, and is also significantly influenced by anthropogenic factors in densely populated areas. The

measurements in Paper VII were carried out at sea, where the aerosol layer mostly consists of water droplets relatively close to the sea surface, usually with a radius < 1 μm. If the composition of particles is known, it is possible to calculate the scattering coefficient by means of Mie theory. However, because the aerosols were not sampled and characterized during the measurements, the scattering was instead estimated with the formula

$$\mu_s = \left[\frac{3.912}{V} - \mu_s^R(550) \right] \cdot \left(\frac{\lambda}{0.55} \right)^q \quad \text{km}^{-1}$$

$$q = 0.585 V^{1/3}, \tag{5.8}$$

where V is the observed visibility [km], $\mu_s^R(550)$ is the Rayleigh scattering coefficient at 550 nm [km^{-1}], and the wavelength λ is expressed in μm[274]. The observed visibility is hardly an exact quantity, so the scattering coefficient calculated by Eq. (5.8) is a very approximate estimate. However, the model developed in Paper VII turned out to be fairly insensitive to variations in the scattering coefficient at lower altitudes, so the approximations seem warranted.

The Monte Carlo model applied in Paper VII was based on reciprocal computation of the detected light (cf. Sect. 3.2.4; Reciprocity). Since the passive instruments were essentially point detectors with a narrow angle of collection, the computational photon economy was improved enormously by launching the photons at the detector and tracing them backwards. By recording the path-length through the volcanic plume, it was possible to derive correction factors for the systematic effects of the passive instruments. Considering the approximations made in the model, the corrections agreed well with measurements of the SO_2 concentration performed with the active lidar system.

Systematic effects due to scattering in passive instrument readings have been modeled previously by Millán for low-altitude gas plumes[275]. The Monte Carlo model presented in Paper VII extends those results to more general conditions. Emission of SO_2 has important environmental implications, and is a major source of acidic rain. It is also believed that SO_2 can be converted to sulfate aerosols, which can have an impact on cloud formation, and thus in the long run, on the climatic systems[276]. Volcanic and anthropogenic emissions are two major sources of SO_2. Routine monitoring of SO_2 emissions must be performed using the relatively simple, inexpensive and robust passive instruments, and it is thus important to be able to quantify the systematic effects due to scattering in the readings.

Acknowledgements

I am grateful for all the help and support from a large number of people, including colleagues and staff at the Atomic Physics division, and all our collaborators at other institutions. Working with physics and technology, so closely related to direct applications in medicine and health care, has been truly inspiring.

Först av allt vill jag tacka min handledare Stefan Andersson-Engels för hans vetenskapliga ledarskap, och även som en god vän på jobbet, på alla våra resor världen över till olika konferenser och möten, och inte minst olika aktiviteter utanför jobbet. Att välta med racekanoten på Ringsjön varje år har blivit något av en klassiker... Jag är också mycket tacksam för samarbetet med min ”vice” handledare Sune Svanberg, som var den som fick mig att börja på Atomfysikavdelningen tack vare hans kombination av pedagogisk förmåga, entusiasm och förmåga att kunna inspirera sina medarbetare. Flera andra seniora forskare, post-docs, administrativ personal och doktorander har också bidragit till den fina atmosfären på avdelningen. Jag vill särskilt tacka tidigare och nuvarande medlemmar av medicingruppen. Några har stått särskilt nära mig, och jag vill tacka Thomas Johansson för att han har hållit sin halva av vårt arbetsrum lika oorganiserad som jag har hållit min. Sara Pålsson, Marcelo Soto Thompson, Christoffer Abrahamsson och Petter Weibring för fin vänskap och samarbete. Jag vill också tacka Annika Enejder – som jag står i tacksamhetsskuld till för att hon har dragit igång mycket av arbetet den här avhandlingen bygger på – Claes af Klinteberg, Jan Sørensen Dam och Ulf Gustafsson.

I also wish to thank the people involved in the Optimamm project. In particular, I've always felt welcome at the research group of Rinaldo Cubeddo at Politecnico di Milano. A special thank you to Antonio Pifferi for our nice collaboration.

Ett stort varmt tack till alla mina vänner, och särskilt grabbarna på BK Smittans mejlinglista.

Jag är särskilt tacksam för allt stöd från mina föräldrar och familj under de här åren.

Till sist vill jag tacka Anette, för att du har stått ut med mig, och för att du är den underbaraste i världen.

Summary of papers

Paper I — New computational methods for prediction of fluorescence signals in layered turbid structures, based on Monte Carlo simulations, were developed and tested. The problem was divided in two parts: one computation for the excitation light, and one for the emitted fluorescence light. These two computations could then be convolved to provide the solution. The computation time could be reduced by up to two orders of magnitude by reversing the photon trajectories when computing the emitted light. The theoretical foundation for this procedure, based on the reciprocity theorem in transport theory, was also treated.

Paper II-III — In these papers, various systems for diffuse-reflectance measurements of turbid media were used to determine the optical properties. In paper II, systems based on spatially resolved cw measurements, time-resolved measurements, and an integrating sphere, were compared with the help of phantom measurements. In paper III, two time-resolved systems were first characterized using phantom measurements, and then used to measure the optical properties of breast tissue.

Paper IV — The integrating sphere technique was used to measure the optical properties of myocardium that had been subjected to radio-frequency ablation therapy. The results could aid the development of an optical probe to guide such therapy in real-time.

Paper V-VI — The integrating sphere technique was used to measure the optical properties of whole blood flowing through an optical cuvette. The results were compared with T-matrix computations of the scattering from single red blood cells, and then discussed in terms of the effects of changes in the cell shapes, orientation, and aggregation. In paper VI, polarized light was used to yield additional information. The limits of singe-scattering theory for the case of whole blood were also explored.

Paper VII — A Monte Carlo model was developed to simulate light propagation in the atmosphere and through a volcanic plume. The model could successfully explain systematic errors in the readings of passive remote sensing instruments used to measure sulfur dioxide emissions, which arise due to light scattering. Reversed photon trajectories based on the reciprocity principle were employed to accelerate the computations.

Contribution by the author to the papers

Paper I Substantial part of theoretical development, model coding, performing and evaluating simulations, and manuscript preparation.

Paper II Major part of integrating sphere measurements and evaluation, phantom preparation, and manuscript preparation. Substantial part of spatially resolved and time-resolved measurements. Contribution to evaluation of spatially resolved and time-resolved data.

Paper III Substantial part of construction of the diode-laser based system and measurements using this system, and manuscript preparation. Contribution to evaluation.

Paper IV Contribution to *in-vivo* experiments. Major part of integrating sphere measurement and evaluation. Substantial part of manuscript preparation.

Paper V Substantial part of experiments, evaluation and manuscript preparation.

Paper VI Substantial part of experiments, evaluation and manuscript preparation.

Paper VII Major part of Monte Carlo model and simulations. Substantial part of manuscript preparation. Contribution to evaluation.

References

1. D. K. Cheng, *Field and wave electromagnetics*, (Addison-Wesley, Reading, MA, 1989).
2. H. C. van de Hulst, *Light scattering by small particles*, (Wiley, New York, NY, 1957).
3. C. F. Bohren and D. R. Huffman, *Absorption and scattering of light by small particles*, (John Wiley & Sons, Inc., New York, NY, 1983).
4. A. Ishimaru, *Electromagnetic wave propagation, radiation, and scattering*, (Prentice-Hall, Inc., New Jersey, 1991).
5. M. I. Mishchenko, J. W. Hovenier, and L. D. Travis, eds., "Light scattering by nonspherical particles," (Academic Press, San Diego, CA, 2000).
6. Prahl, S. A., "Web based Mie scattering calculations," http://omlc.ogi.edu/calc/mie_calc.html (2002).
7. M. I. Mishchenko, L. D. Travis, and D. W. Mackowski, "*T*-matrix computations of light scattering by nonspherical particles: a review," J. Quantitative Spectroscopy & Radiative Transfer **55,** 535-575 (1996).
8. P. W. Barber and S. C. Hill, *Light scattering by particles: computational methods.*, (World Scientific Publishing Co. Pte. Ltd., Singapore, 1990).
9. A. M. K. Nilsson, P. Alsholm, A. Karlsson, and S. Andersson-Engels, "*T*-matrix computations of light scattering by red blood cells," Appl. Opt. **37,** 2735-2748 (1998).
10. M. I. Mishchenko and L. D. Travis, "T-matrix computations of light scattering by large spheroidal particles," Opt. Comm. **109,** 16-21 (1994).
11. K. A. Fuller, "Optical resonances and two-sphere systems," Appl. Opt. **30,** 4716-4731 (1991).
12. B. Gustafsson, H.-O. Kreiss, and J. Oliger, *Time-dependent problems and difference methods*, (John Wiley & Sons, New York, 1995).
13. "FDTD.org - Finite-Difference Time-Domain Literature Database," http://www.fdtd.org/ (2002).
14. A. Dunn, C. Smithpeter, A. J. Welch, and R. Richards-Kortum, "Finite-difference time-domain simulation of light scattering from single cells," J. Biomedical Optics **2,** 262-266 (1997).
15. R. Drezek, A. Dunn, and R. Richards-Kortum, "Light scattering from cells: finite difference time-domain simulations and goniometric measurements," Appl. Opt. **38,** 3651-3661 (1999).
16. R. Drezek, A. Dunn, and R. Richards-Kortum, "A pulsed finite-difference time-domain (FDTD) method for calculating light scattering from biological cells over broad wavelength ranges," Optics Express **6,** 147-157 (2000).
17. "EMAP - Finite element electromagnetic modeling codes," http://www.emclab.umr.edu/emap.html (2002).
18. "Student's Quickfield," http://www.quickfield.com/ (2002).
19. "FEMLAB by Comsol," http://www.comsol.com/ (2002).
20. "EMFLex - The Finite Element Solver For Maxwell's Electromagnetics Equations by Weidlinger Associates Inc.," http://www.wai.com/AppliedScience/Software/Emflex/index-em.html (2002).
21. R. F. Harrington, *Field computation by moment methods*, (Macmillan, New York, 1968).
22. "PCB-MoM by SP - Swedish National Testing and Research Institute," http://www.sp.se/electronics/RnD/software/eng/pcbMoM.htm (2002).
23. R. Coifman, V. Rokhlin, and S. Wandzura, "The fast multipole method for the wave equation: A pedestrian prescription," IEEE Antennas and Propagation Magazine **35,** 7-12 (1993).
24. M. F. Levy, "Parabolic wave equation techniques for radiowave propagation," Radio Science Bulletin **282,** 6-13 (1997).

25. H. Bremmer, "The W.K.B. approximation as the first term of a geometric-optical series," Comm. Pure Appl. Math. **4,** 105-115 (1951).
26. A. Ishimaru, *Wave propagation and scattering in random media*, (Academic Press, New York, NY, 1978).
27. V. Twersky, "Absorption and multiple scattering by biological suspensions," J. Opt. Soc. Am. **60,** 1084-1093 (1970).
28. J. M. Steinke and A. P. Shepard, "Role of light scattering in whole blood oximetry," IEEE Trans. Biomed. Eng. **BME-33,** 294-301 (1986).
29. K. M. Case and P. F. Zweifel, *Linear transport theory*, (Addison-Wesley Publishing Co., Reading, MA, 1967).
30. A. J. Welch and M. J. C. van Gemert, *Optical-Thermal Response of Laser-Irradiated Tissue*, (Plenum Press, New York, NY, 1995).
31. S. Chandrasekar, *Radiative transfer*, (Oxford University Press, London, England, 1960).
32. L. G. Henyey and J. L. Greenstein, "Diffuse radiation in the galaxy," Astrophys. J. **93,** 70-83 (1941).
33. L. O. Reynolds and N. J. McCormick, "Approximate two-parameter phase function for light scattering," J. Opt. Soc. Am. **70,** 1206-1212 (1980).
34. H. C. van de Hulst, *Multiple light scattering*, (Academic Press, London, 1980).
35. S. A. Prahl, "Simple and accurate approximations for reflectance from a semi-infinite turbid medium," in *OSA Biomedical Topical Meetings, OSA Technical Digest,* Proc. Optical Society of America, Washington DC OSA, (2002) pp. 613-615.
36. P. Kubelka and F. Munk, "Ein Beitrag zur Optik der Farbanstriche," Z. Tech. Phys. **12,** 593-601 (1931).
37. J. Dorsey and P. Hanrahan, "Digital materials and virtual weathering," Sci. Am. **282,** 46-53 (2000).
38. Y. Yang, E. J. Celmer, J. A. Koutcher, and R. R. Alfano, "DNA and protein changes caused by disease in human breast tissues probed by the Kubelka-Munk spectral function," Photochem. Photobiol. **75,** 627-632 (2002).
39. R. Graaff, J. G. Aarnoudse, F. F. M. de Mul, and H. W. Jentink, "Light propagation parameters for anisotropically scattering media based on a rigorous solution of the transport equation," Appl. Opt. **28,** 2273-2279 (1989).
40. S. A. Prahl, "The adding-doubling method," in *Optical-thermal response of laser-irradiated tissue,* A. J. Welch and M. J. C. van Gemert (eds.), (Plenum Press, New York, 1995), pp. 101-129. Note that an errata list for the adding-doubling chapter can be obtained from Scott Prahl, http://omlc.ogi.edu/software/ad/errata.pdf
41. W. J. Wiscombe, "On initialization, error and flux conservation in the doubling method," J. Quantitative Spectroscopy & Radiative Transfer **16,** 637-658 (1976).
42. S. A. Prahl, "Adding-Doubling software," http://omlc.ogi.edu/software/ad/index.html (2002).
43. G. Yoon, A. J. Welch, M. Motamedi, and M. J. C. van Gemert, "Development and application of three-dimensional light distribution model for laser irradiated tissue," IEEE J. Quant. Electr. **QE-23,** 1721-1733 (1987).
44. W. H. Press, S. A. Teukolsky, W. T. Vetterling, and B. P. Flannery, *Numerical recipes in C: The art of scientific computing*, (Cambridge University Press, New York, 1992).
45. D. Balsara, "Fast and accurate discrete ordinates methods for multidimensional radiative transfer. I. Basic methods," J. Quantitative Spectroscopy & Radiative Transfer **69,** 671-707 (2001).
46. J. E. Morel, "A synthetic acceleration method for discrete ordinates calculations with highly anisotropic scattering," Nucl. Sci. Eng. **82,** 34-46 (1982).
47. A. H. Hielscher, R. E. Alcouffe, and R. L. Barbour, "Comparison of finite-difference transport and diffusion calculations for photon migration in homogeneous and heterogeneous tissues," Phys. Med. Biol. **43,** 1285-1302 (1998).

48. A. D. Klose and A. H. Hielscher, "Iterative reconstruction scheme for optical tomography based on the equation of radiative transfer," Med. Phys. **26,** 1698-1707 (1999).
49. A. D. Klose, U. Netz, K. Beuthan, and A. H. Hielscher, "Optical tomography using the time-independent equation of radiative transfer. 1. Forward model," J. Quantitative Spectroscopy & Radiative Transfer **72,** 691-713 (2002).
50. S. R. Arridge, "Optical tomography in medical imaging," Inverse Problems **15,** R41-R93 (1999).
51. Y. Yamada, "Diffusion coefficient in the photon diffusion equation," in *Optical Tomography, Photon Migration, and Spectroscopy of Tissue and Model Media: Theory, Human Studies, and Instrumentation,* B. Chance, R. R. Alfano, and A. Katzir (eds.), Proc. SPIE **2389**, (SPIE, 1995), pp. 87-97.
52. T. Durduran, A. G. Yodh, B. Chance, and D. A. Boas, "Does the photon-diffusion coefficient depend on absorption?," J. Opt. Soc. Am. A **14,** 3358-3365 (1997).
53. T. J. Farrell, M. S. Patterson, and B. Wilson, "A diffusion theory model of spatially resolved, steady-state diffuse reflectance for noninvasive determination of tissue optical properties *in vivo*," Med. Phys. **19,** 879-888 (1992).
54. R. C. Haskell, L. O. Svaasand, T.-T. Tsay, T.-C. Feng, M. S. McAdams, and B. J. Tromberg, "Boundary conditions for the diffusion equation in radiative transfer," J. Opt. Soc. Am. A **11,** 2727-2741 (1994).
55. M. S. Patterson, B. Chance, and B. C. Wilson, "Time resolved reflectance and transmittance for the non-invasive measurement of optical properties," Appl. Opt. **28,** 2331-2336 (1989).
56. A. Kienle and M. S. Patterson, "Improved solutions of the steady-state and the time-resolved diffusion equations for reflectance from a semi-infinite turbid medium," J. Opt. Soc. Am. A **14,** 246-254 (1997).
57. A. Kienle, M. S. Patterson, N. Dögnitz, R. Bays, G. Wagnières, and H. van den Bergh, "Noninvasive determination of the optical properties of two-layered turbid media," Appl. Opt. **37,** 779-791 (1998).
58. A. Kienle and T. Glanzmann, "In vivo determination of the optical properties of muscle with time-resolved reflectance using a layered model," Phys. Med. Biol. **44,** 2689-2702 (1999).
59. D. A. Boas, M. A. O'Leary, B. Chance, and A. G. Yodh, "Scattering of diffuse photon density waves by spherical inhomogeneities within turbid media: Analytic solution and applications," Proc. Natl. Acad. Sci. USA **91,** 4887-4891 (1994).
60. C. Lindquist, R. Berg, and S. Andersson-Engels, "Numerical diffusion modelling of interfering photon density waves for optical mammography," in *Photon Transport in Highly Scattering Tissue,* S. Avrillier, B. Chance, G. J. Müller, A. V. Priezzhev, and V. V. Tuchin (eds.), Proc. SPIE **2326**, (Soc. Photo-Opt. Instrum. Eng., Bellingham, WA, 1994), pp. 31-40.
61. A. H. Hielscher, A. D. Klose, and K. M. Hanson, "Gradient-based iterative image reconstruction scheme for time-resolved optical tomography," IEEE Trans. Med. Imaging **18,** 262-271 (1999).
62. J. C. Haselgrove, N. G. Wang, and B. Chance, "Investigation of the nonlinear aspects of imaging through a highly scattering medium," Med. Phys. **19,** 17-23 (1992).
63. S. R. Arridge, M. Schweiger, M. Hiraoka, and D. T. Delpy, "A finite element approach for modeling photon transport in tissue," Med. Phys. **20,** 299-309 (1993).
64. S. R. Arridge and M. Schweiger, "Direct calculation of the moments of the distribution of photon time of flight in tissue with a finite-element method," Appl. Opt. **34,** 2683-2687 (1995).
65. S. R. Arridge and M. Schweiger, "Photon-measurement density functions. Part 2: Finite-element-method calculations," Appl. Opt. **34,** 8026-8037 (1995).
66. M. Schweiger and S. R. Arridge, "Direct calculation with a finite-element method of the Laplace transform of the distribution of photon time of flight in tissue," Appl. Opt. **36,** 9042-9049 (1997).

67. H. Jiang, K. D. Paulsen, U. L. Osterberg, B. W. Pogue, and M. S. Patterson, "Simultaneous reconstruction of optical absorption and scattering maps in turbid media from near-infrared frequency-domain data," Opt. Lett. **20,** 2128-2130 (1995).
68. T. Johansson, M. Soto Thompson, M. Stenberg, C. af Klinteberg, S. Andersson-Engels, S. Svanberg, and K. Svanberg, "Feasibility study of a novel system for combined light dosimetry and interstitial photodynamic treatment of massive tumors," Appl. Opt. **41,** 1462-1468 (2002).
69. A. Ishimaru, "Diffusion of a pulse in densley distributed scatterers," J. Opt. Soc. Am. **68,** 1045-1050 (1978).
70. R. F. Bonner, R. Nossal, S. Havlin, and G. H. Weiss, "Model for photon migration in turbid biological media," J. Opt. Soc. Am. A **4,** 423-432 (1987).
71. R. Nossal, R. F. Bonner, and G. H. Weiss, "Influence of path length on remote optical sensing of properties of biological tissue," Appl. Opt. **89,** 2238-2244 (1989).
72. L. T. Perelman, J. Wu, I. Itzkan, and M. S. Feld, "Photon migration in turbid media using path integrals," Phys. Rev. Lett. **72,** 1341-1344 (1994).
73. L. T. Perelman, J. Wu, Y. Wang, I. Itzkan, R. R. Dasari, and M. S. Feld, "Time-dependent photon migration using path integrals," Phys. Rev. E: Statistical Physics **51,** 6134-6141 (1995).
74. L. T. Perelman, Jun-Wu, Kun-Chen, I. Itzkan, R. R. Dasari, and M. S. Feld, "Photon paths in turbid media: from smooth to random," in *OSA Trends in Optics and Photonics on Advances in Optical Imaging and Photon Migration. Vol.2 From the Topical Meeting. Opt. Soc. America,* Proc. OSA **2**, (1996), pp. 18-20.
75. S. K. Park and K. W. Miller, "Random number generators: good ones are hard to find," Communications of the ACM **31,** 1192-1201 (1988).
76. L. Wang and S. L. Jacques, "Monte Carlo modeling of light transport in multi-layered tissues in standard C," (Laser Biology Research Laboratory, M. D. Anderson Cancer Center, University of Texas, Houston, Texas, 1992).
77. L. Wang, S. L. Jacques, and L. Zheng, "MCML - Monte Carlo modeling of light transport in multi-layered tissues," Computer Methods and Programs in Medicine **47,** 131-146 (1995).
78. R. Berg, "Laser-based cancer diagnostics and therapy - Tissue optics considerations," (1995). Ph.D. Thesis, Lund Institute of Technology, Lund, Sweden.
79. P. Alsholm, "Light scattering by individual and groups of spheroidal particles," (1996). Lund, Sweden, Lund Institute of Technology.
80. A. Kienle and M. S. Patterson, "Determination of the optical properties of turbid media from a single Monte Carlo simulation," Phys. Med. Biol. **41,** 2221-2227 (1996).
81. A. Pifferi, P. Taroni, G. Valentini, and S. Andersson-Engels, "Real-time method for fitting time-resolved reflectance and transmittance measurements with a Monte Carlo model," Appl. Opt. **37,** 2774-2780 (1998).
82. M. H. Eddowes, T. N. Mills, and D. T. Delpy, "Monte Carlo simulations of coherent backscatter for identification of the optical coefficients of biological tissues in vivo," Appl. Opt. **34,** 2261-2267 (1995).
83. A. Pifferi, R. Berg, P. Taroni, and S. Andersson-Engels, "Fitting of time-resolved reflectance curves with a Monte Carlo model," in *Advances in optical imaging and photon migration,* R. R. Alfano and J. G. Fujimoto (eds.), Proc. Optical Society of America **2**, (Optical Society of America, Washington, D.C., 1996), pp. 311-314.
84. G. Yao and L. Wang, "Propagation of polarized light in turbid media: simulated animation sequences," Optics Express **7,** 198-203 (2000).
85. X. Wang and L. V. Wang, "Propagation of polarized light in birefringent turbid media: time-resolved simulations," Optics Express **9,** 254-259 (2001).
86. R. Richards-Kortum and E. Sevick-Muraca, "Quantitative optical spectroscopy for tissue diagnosis," Annu. Rev. Phys. Chem. **47,** 555-606 (1996).

87. S. Andersson-Engels, K. Svanberg, and S. Svanberg, "Fluorescence diagnostic imaging," in *Biomedical Optical Imaging*, J. G. Fujimoto, ed., (Oxford University Press, to appear, 2002).
88. J. C. Schotland, J. C. Haselgrove, and J. S. Leigh, "Photon hitting density," Appl. Opt. **32,** 448-453 (1993).
89. S. R. Arridge, "Photon-measurement density functions. Part I: analytical forms," Appl. Opt. **34,** 7395-7409 (1995).
90. S. T. Flock, B. C. Wilson, M. S. Patterson, and D. R. Wyman, "Monte Carlo modeling of light propagation in highly scattering tissues - I: Model predictions and comparison with diffusion theory," IEEE Trans. Biomed. Eng. **36,** 1162-1168 (1989).
91. J. Wu, F. Partovi, M. S. Feld, and R. P. Rava, "Diffuse reflectance from turbid media: an analytical model of photon migration," Appl. Opt. **32,** 1115-1121 (1993).
92. L. Wang and S. L. Jacques, "Hybrid model of Monte Carlo simulation and diffusion theory for light reflectance by turbid media," J. Opt. Soc. Am. A **10,** 1746-1752 (1993).
93. J. B. Fishkin and E. Gratton, "Propagation of photon density waves in strongly scattering media containing an absorbing semi-infinite plane bounded by a straight edge," J. Opt. Soc. Am. A **10,** 127-140 (1993).
94. S. Fantini, M. A. Franceschini, and E. Gratton, "Semi-infinite-geometry boundary problem for light migration in highly scattering media: a frequency-domain study in the diffusion approximation," J. Opt. Soc. Am. B **11,** 2128-2138 (1994).
95. A. Kienle and M. S. Patterson, "Determination of the optical properties of semi-infinite turbid media from frequency-domain reflectance close to the source," Phys. Med. Biol. **42,** 1801-1819 (1997).
96. G. Alexandrakis, T. J. Farrell, and M. S. Patterson, "Accuracy of the diffusion approximation in determining the optical properties of a two-layered turbid medium," Appl. Opt. **37,** 7401-7409 (1998).
97. T. J. Farrell, M. S. Patterson, and M. Essenpreis, "Influence of layered tissue architecture on estimates of tissue optical properties obtained from spatially resolved diffuse reflectometry," Appl. Opt. **37,** 1958-1972 (1998).
98. T. Spott and L. O. Svaasand, "Collimated light sources in the diffusion approximation," Appl. Opt. **39,** 6453-6465 (2000).
99. G. Alexandrakis, T. J. Farrell, and M. S. Patterson, "Monte Carlo diffusion hybrid model for photon migration in a two-layer turbid medium in the frequency domain," Appl. Opt. **39,** 2235-2244 (2000).
100. D. E. Hyde, T. J. Farrell, M. S. Patterson, and B. C. Wilson, "A diffusion theory model of spatially resolved fluorescence from depth-dependent fluorophore concentrations," Phys. Med. Biol. **46,** 369-383 (2001).
101. R. L. Fante, "Relationship between radiative-transport theory and Maxwell's equations in dielectric media," J. Opt. Soc. Am. **71,** 460-468 (1981).
102. J. S. Dam, C. B. Pedersen, T. Dalgaard, P. E. Fabricius, P. Aruna, and S. Andersson-Engels, "Fiber optic probe for non-invasive real-time determination of tissue optical properties at multiple wavelengths," Appl. Opt. **40,** 1155-1164 (2001).
103. M. G. Nichols, E. L. Hull, and T. H. Foster, "Design and testing of a white-light, steady-state diffuse reflectance spectrometer for determination of optical properties of highly scattering systems," Appl. Opt. **36,** 93-104 (1997).
104. J. R. Mourant, T. Fuselier, J. Boyer, T. M. Johnson, and I. J. Bigio, "Predictions and measurements of scattering and absorption over broad wavelength ranges in tissue phantoms," Appl. Opt. **36,** 949-957 (1997).
105. R. M. P. Doornbos, R. Lang, M. C. Aalders, F. W. Cross, and H. J. C. M. Sterenborg, "The determination of *in vivo* human tissue optical properties and absolute chromophore concentrations using spatially resolved steady-state diffuse reflectance spectroscopy," Phys. Med. Biol. **44,** 967-981 (1999).

106. R. L. P. van Veen, W. Verkruysse, and H. J. C. M. Sterenborg, "Diffuse-reflectance spectroscopy from 500 to 1060 nm by correction for inhomogeneously distributed absorbers," Opt. Lett. **27,** 246-248 (2002).
107. T. H. Pham, F. Bevilacqua, T. Spott, J. S. Dam, B. J. Tromberg, and S. Andersson-Engels, "Quantifying the absorption and reduced scattering coefficients of tissue-like turbid media over a broad spectral range using a non-contact Fourier interferometric, hyperspectral imaging system," Appl. Opt. **39,** 6487-6497 (2000).
108. R. Cubeddu, A. Pifferi, P. Taroni, A. Torricelli, and G. Valentini, "Experimental test of theoretical models for time-resolved reflectance," Med. Phys. **23,** 1625-1633 (1996).
109. M. S. Patterson, J. D. Moulton, B. C. Wilson, K. W. Berndt, and J. R. Lakowicz, "Frequency-domain reflectance for the determination of the scattering and absorption properties of tissue," Appl. Opt. **30,** 4474-4476 (1991).
110. S. J. Madsen, P. Wyss, L. O. Svaasand, R. C. Haskell, Y. Tadir, and B. J. Tromberg, "Determination of the optical properties of the human uterus using frequency-domain photon migration and steady-state techniques," Phys. Med. Biol. **39,** 1191-1202 (1994).
111. J. W. Pickering, C. J. M. Moes, H. J. C. M. Sterenborg, S. A. Prahl, and M. J. C. van Gemert, "Two integrating sphere with an intervening scattering sample," J. Opt. Soc. Am. **9,** 621-631 (1992).
112. J. W. Pickering, S. A. Prahl, N. van Wieringen, J. F. Beek, H. J. C. M. Sterenborg, and M. J. C. van Gemert, "Double-integrating-sphere system for measuring the optical properties of tissue," Appl. Opt. **32,** 399-410 (1993).
113. D. D. Royston, R. S. Poston, and S. A. Prahl, "Optical properties of scattering and absorbing materials used in the development of optical phantoms at 1064 nm," J. Biomedical Optics **1,** 110-116 (1997).
114. J. F. Beek, P. Blokland, P. Posthumus, M. Aalders, J. W. Pickering, H. J. C. M. Sterenborg, and M. J. C. van Gemert, "*In vitro* double-integrating-sphere optical properties of tissues between 630 and 1064 nm," Phys. Med. Biol. **42,** 2255-2261 (1997).
115. J. H. Torres, A. J. Welch, I. Cilesiz, and M. Motamedi, "Tissue optical property measurements: Overestimation of absorption coefficient with spectrophotometric techniques," Lasers Surg. Med. **14,** 249-257 (1994).
116. G. de Vries, J. F. Beek, G. W. Lucassen, and M. J. C. van Gemert, "The effect of light losses in double integrating spheres on optical properties estimation," IEEE Journal of Selected Topics in Quantum Electronics **5,** 944-947 (1999).
117. A. M. K. Nilsson, R. Berg, and S. Andersson-Engels, "Measurements of the optical properties of tissue in conjunction with photodynamic therapy," Appl. Opt. **34,** 4609-4619 (1995).
118. A. M. K. Nilsson, G. W. Lucassen, W. Verkruysse, S. Andersson-Engels, and M. J. C. van Gemert, "Changes in optical properties of human whole blood in vitro due to slow heating," Photochem. Photobiol. **65,** 366-373 (1997).
119. A. M. K. Nilsson, C. Sturesson, D. L. Liu, and S. Andersson-Engels, "Changes in spectral shape of tissue optical properties in conjunction with laser-induced thermotherapy," Appl. Opt. **37,** 1256-1267 (1998).
120. A. M. K. Enejder, "Light scattering and absorption in tissue - models and measurements," (1997). Ph.D. Thesis, Lund Institute of Technology, Lund, Sweden.
121. J. S. Dam, T. Dalgaard, P. E. Fabricius, and S. Andersson-Engels, "Multiple polynomial regression method for determination of biomedical optical properties from integrating sphere measurements," Appl. Opt. **39,** 1202-1209 (2000).
122. J. A. Jacquez and H. F. Kuppenheim, "Theory of the integrating sphere," J. Opt. Soc. Am. **45,** 460-470 (1955).
123. D. G. Goebel, "Generalized integrating-sphere theory," Appl. Opt. **6,** 125-128 (1967).
124. J. G. Symons, E. A. Christie, and M. K. Peck, "Integrating sphere for solar transmittance measurement of planar and nonplanar samples," Appl. Opt. **21,** 2827-2832 (1982).

125. K. Grandin and A. Roos, "Evaluation of correction factors for transmittance measurements in single-beam integrating sphere," Appl. Opt. **33,** 6098-6104 (1994).
126. L. Wang and S. L. Jacques, "Error estimation of measuring total interaction coefficients of turbid media using collimated light transmission," Phys. Med. Biol. **39,** 2349-2354 (1994).
127. M. Ozolinsh, I. Lacis, R. Paeglis, A. Sternberg, S. Svanberg, S. Andersson-Engels, and J. Swartling, "Electrooptic PLZT ceramics devices for vision science applications," Ferroelectrics **273,** 131-136 (2002).
128. M. Firbank, M. Hiraoka, M. Essenpreis, and D. T. Delpy, "Measurement of the optical properties of the skull in the wavelength range 650-950 nm," Phys. Med. Biol. **38,** 503-510 (1993).
129. J. S. Dam, "Optical analysis of biological media - continuous wave diffuse spectroscopy," (2000). Ph.D. Thesis, Lund Institute of Technology, Lund, Sweden.
130. A. Kienle, M. S. Patterson, L. Ott, and R. Steiner, "Determination of the scattering coefficient and the anisotropy factor from laser Doppler spectra of liquids including blood," Appl. Opt. **35,** 3404-3412 (1996).
131. R. J. Hunter, M. S. Patterson, T. J. Farrell, and J. E. Hayward, "Haemoglobin oxygenation of a two-layer tissue-simulating phantom from time-resolved reflectance: Effect of top layer thickness," Phys. Med. Biol. **47,** 193-208 (2002).
132. J. Ripoll, V. Ntziachristos, J. P. Culver, D. N. Pattanayak, A. G. Yodh, and M. Nieto-Vesperinas, "Recovery of optical parameters in multiple-layered diffusive media: theory and experiments," J. Opt. Soc. Am. A **18,** 821-830 (2001).
133. A. H. Hielscher, M. Azeez-Jan, and S. Bartel, "Tomographic reconstruction of layered tissue structures," in *Photon Migration, Optical Coherence Tomography, and Microscopy,* S. Andersson-Engels and M. F. Kaschke (eds.), Proc. SPIE **4431**, (SPIE, Belligham, WA, 2001), pp. 126-133.
134. D. A. Boas, M. A. O'Leary, B. Chance, and A. G. Yodh, "Detection and characterization of optical inhomogeneities with diffuse photon density waves: a signal-to noise analysis," Appl. Opt. **36,** 75-92 (1997).
135. S. Fantini, S. A. Walker, M. A. Franceschini, M. Kaschke, P. M. Schlag, and K. T. Moesta, "Assessment of the size, position, and optical properties of breast tumors *in vivo* by noninvasive optical methods," Appl. Opt. **37,** 1982-1989 (1998).
136. D. Grosenick, H. Wabnitz, H. H. Rinneberg, K. T. Moesta, and P. M. Schlag, "Development of a time-domain optical mammograph and first in vivo applications," Appl. Opt. **38,** 2927-2943 (1999).
137. S. A. Walker, D. A. Boas, and E. Gratton, "Photon density waves scattered from cylindrical inhomogeneities: theory and experiments," Appl. Opt. **37,** 1935-1944 (1998).
138. Y. Yamashita, A. Maki, and H. Koizumi, "Measurement system for noninvasive dynamic optical topography," J. Biomedical Optics **4,** 414-417 (1999).
139. M. A. Franceschini, V. Toronov, M. E. Filiaci, E. Gratton, and S. Fantini, "On-line optical imaging of the human brain with 160-ms temporal resolution," Optics Express **6,** 49-57 (2000).
140. M. A. Franceschini, J. Thompson, J. P. Culver, G. Strangman, and D. A. Boas, "Looking for the fast signal: Neuronal and hemodynamic evoked responses of the sensory-motor cortex," in *OSA Biomedical Topical Meetings, OSA Technical Digest,* Proc. Optical Society of America, Washington DC OSA, (2002) pp. 208-210.
141. R. Cubeddu, G. M. Danesini, E. Giambattistelli, F. Messina, L. Pallaro, A. Pifferi, P. Taroni, and A. Torricelli, "Time-resolved optical mammograph for clinical studies beyond 900 nm," in *OSA Biomedical Topical Meetings, OSA Technical Digest,* Proc. Opitcal Society of Ametica, Washington DC OSA, (2002) pp. 674-676.
142. R. Berg, O. Jarlman, and S. Svanberg, "Medical transillumination imaging using short-pulse diode lasers," Appl. Opt. **32,** 574-579 (1993).

143. J. R. Singer, F. A. Grünbaum, P. Kohn, and J. P. Zubelli, "Image reconstruction of the interior of bodies that diffuse radiation," Science **248,** 990-993 (1990).
144. S. R. Arridge and W. R. B. Lionheart, "Nonuniqueness in diffusion-based optical tomography," Opt. Lett. **23,** 882-884 (1998).
145. Y. Pei, H. L. Graber, and R. L. Barbour, "Influence of systematic errors in reference states on image quality and on stability of derived information for dc optical imaging," Appl. Opt. **40,** 5755-5769 (2001).
146. Y. Xu, X. Gu, T. Khan, and H. Jiang, "Absorption and scattering images of heterogeneous scattering media can be simultaneously reconstructed by use of dc data," Appl. Opt. **41,** 5427-5437 (2002).
147. D. A. Boas, "A fundamental limitation of linearized algorithms for diffuse optical tomography," Optics Express **1,** 404-413 (1997).
148. S. R. Arridge, "Methods for the inverse problem in optical tomography," in *Proceedings of Waves and Imaging Through Complex Media,* P. Sebbah and J.-M. Tualle (eds.), (Kluwer, 2001), pp. 307-329 .
149. J. P. Culver, A. Siegel, M. A. Franceschini, J. J. Marota, J. B. Mandeville, and D. A. Boas, "Which hemodynamic contrast best localizes neuronal activity? A diffuse optical tomography study," in *OSA Biomedical Topical Meetings, OSA Technical Digest,* Proc. Optical Society of America, Washington DC OSA, (2002) pp. 41-43.
150. S. R. Arridge and M. Schweiger, "A gradient-based optimisation scheme for optical tomography," Optics Express **2,** 213-226 (1998).
151. S. R. Arridge, J. C. Hebden, M. Schweiger, F. E. W. Schmidt, M. E. Fry, E. M. C. Hillman, H. Dehghani, and D. T. Delpy, "A method for three-dimensional time-resolved optical tomography," Int. J. Imag. Syst. Tech. **11,** 2-11 (2000).
152. J. C. Hebden, F. E. W. Schmidt, M. E. Fry, M. Schweiger, E. M. C. Hillman, D. T. Delpy, and S. R. Arridge, "Simultaneous reconstruction of absorption and scattering images by multichannel measurement of purely temporal data," Opt. Lett. **24,** 534-536 (1999).
153. E. M. C. Hillman, J. C. Hebden, F. E. W. Schmidt, S. R. Arridge, M. Schweiger, H. Dehghani, and D. T. Delpy, "Calibration techniques and datatype extraction for time-resolved optical tomography," Rev. Sci. Instrum. **71,** 3415-3427 (2000).
154. E. M. C. Hillman, J. C. Hebden, M. Schweiger, H. Dehghani, F. E. W. Schmidt, D. T. Delpy, and S. R. Arridge, "Time resolved optical tomography of the human forearm," Phys. Med. Biol. **46,** 1117-1130 (2001).
155. J. C. Hebden, H. Veenstra, H. Dehghani, E. M. C. Hillman, M. Schweiger, S. R. Arridge, and D. T. Delpy, "Three-dimensional time-resolved optical tomography of a conical breast phantom," Appl. Opt. **40,** 3278-3287 (2001).
156. Schweiger, M. and Arridge, S. R., "TOAST - Time-resolved Optical Absorption and Scatter Tomography," http://www.medphys.ucl.ac.uk/~martins/toast/index.html (2002).
157. A. D. Klose and A. H. Hielscher, "Optical tomography using the time-independent equation of radiative transfer. 2. Inverse model," J. Quantitative Spectroscopy & Radiative Transfer **72,** 715-732 (2002).
158. M. Firbank, S. R. Arridge, M. Schweiger, and D. T. Delpy, "An investigation of light transport through scattering bodies with non-scattering regions," Phys. Med. Biol. **41,** 767-783 (1996).
159. J. Riley, H. Dehghani, M. Schweiger, S. R. Arridge, J. Ripoll, and M. Nieto-Vesperinas, "3D optical tomography in the presence of void regions," Optics Express **7,** 462-467 (2000).
160. H. Dehghani, S. R. Arridge, M. Schweiger, and D. T. Delpy, "Optical tomography in the presence of void regions," J. Opt. Soc. Am. A **17,** 1659-1670 (2000).
161. F. P. Bolin, L. E. Preuss, R. C. Taylor, and R. J. Ference, "Refractive index of some mammalian tissue using a fiber optic cladding method," Appl. Opt. **28,** 2297-2303 (1989).

162. B. Beauvoit, S. M. Evans, T. W. Jenkins, E. E. Miller, and B. Chance, "Correlation between the light scattering and the mitochondrial content of normal tissues and transplantable rodent tumors," Anal. Biochem. **226,** 167-174 (1995).
163. J. R. Mourant, T. M. Johnson, V. Doddi, and J. P. Freyer, "Angular dependent light scattering from multicellular spheroids," J. Biomedical Optics **7,** 93-99 (2002).
164. J. Beuthan, O. Minet, J. Helfmann, M. Herrig, and G. Müller, "The spatial variation of the refractive index in biological cells," Phys. Med. Biol. **41,** 369-382 (1996).
165. J. R. Mourant, M. Canpolat, C. Brocker, O. Esponda-Ramos, T. M. Johnson, A. Matanock, K. Stetter, and J. P. Freyer, "Light scattering from cells: the contribution of the nucleus and the effects of proliferative status," J. Biomedical Optics **5,** 131-137 (2000).
166. F. K. Forster, A. Kienle, and R. Hibst, "Determination of the optical parameters of dentin from spatially resolved reflectance and transmittance measurements," in *Diagnostic Optical Spectroscopy in Biomedicine,* T. G. Papazoglou and G. A. Wagnières (eds.), Proc. SPIE **4432**, (SPIE, Washington, DC, 2001), pp. 103-109.
167. J. R. Mourant, T. M. Johnson, S. Carpenter, A. Guerra, T. Aida, and J. P. Freyer, "Polarized angular dependent spectroscopy of epithelial cells and epithelial cell nuclei to determine the size scale of scattering structures," J Biomed Opt **7,** 378-387 (2002).
168. V. Sankaran, J. T. Walsh, Jr., and D. J. Maitland, "Comparative study of polarized light propagation in biologic tissues," J Biomed Opt **7,** 300-306 (2002).
169. A. H. Hielscher, J. R. Mourant, and I. J. Bigio, "Influence of particle size and concentration on the diffuse backscattering of polarized light from tissue phantoms and biological cell suspensions," Appl. Opt. **36,** 125-135 (1997).
170. A. H. Hielscher, A. A. Eick, J. R. Mourant, D. Shen, J. P. Freyer, and I. J. Bigio, "Diffuse backscattering Mueller matrices of highly scattering media," Optics Express **1,** 441-453 (1997).
171. L. T. Perelman, V. Backman, M. Wallace, G. Zonios, R. Manoharan, A. Nusrat, S. Shields, M. Seiler, C. Lima, T. Hamano, I. Itzkan, J. van Dam, J. M. Crawford, and M. S. Feld, "Observation of periodic fine structure in reflectance from biological tissue: a new technique for measuring nuclear size distribution," Phys. Rev. Lett. **80,** 627-630 (1998).
172. D. Huang, E. A. Swanson, C. P. Lin, J. S. Schuman, W. G. Stinson, W. Chang, M. R. Hee, T. Flotte, K. Gregory, C. A. Puliafito, and J. G. Fujimoto, "Optical coherence tomography," Science **254,** 1178-1181 (1991).
173. L. Thrane, H. T. Yura, and P. E. Andersen, "Analysis of optical coherence tomography systems based on the extended Huygens-Fresnel principle," J. Opt. Soc. Am. A **17,** 484-490 (2000).
174. L. Thrane, H. T. Yura, and P. E. Andersen, "Calculation of the maximum obtainable probing depth of optical coherence tomography in tissue," in *Coherence Domain Optical Methods in Biomedical Science and Clinical Applications IV,* Proc. SPIE **3915**, (Washington, DC, 2000), pp. 2-11.
175. I. Hartl, X. D. Li, C. Chudoba, T. H. Ko, and J. G. Fujimoto, "Ultrahigh resolution OCT using continuum generation in an air-silica," in *Proceedings of the SPIE,* Proc. **4431**, (SPIE The International Society for Optical Engineering., 2001), pp. 25-29.
176. G. M. Hale and M. R. Querry, "Optical constants of water in the 200-nm to 200-μm wavelength region," Appl. Opt. **12,** 555-563 (1973).
177. S. A. Prahl, "Tabulated molar extinction coefficient for hemoglobin in water," http://omlc.ogi.edu/spectra/hemoglobin/index.html (1998).
178. E. Antonini and M. Brunori, *Hemoglobin and myoglobin in their reactions with ligands*, (North-Holland Publishing Company, Amsterdam, 1971).
179. M. F. Perutz and K. Imai, "Regulation of oxygen affinity of mammalian haemoglobins," J. Mol. Biol. **136,** 183-191 (1980).

180. A. E. Arai, C. E. Kasserra, P. R. Territo, A. H. Gandjbakhche, and R. S. Balaban, "Myocardial oxygenation in vivo: optical spectroscopy of cytoplasmic myoglobin and mitochondrial cytochromes," Am. J. Physiol. **277,** H683-H697 (1999).
181. C. Eker, "Optical characterization of tissue for medical diagnostics," (1999). Ph.D. Thesis, Lund Institute of Technology, Lund, Sweden.
182. S. L. Jacques and D. J. McAuliffe, "The melanosome: Threshold temperature for explosive vaporization and internal absorption coefficient during pulsed laser irradiation," Photochem. Photobiol. **53,** 769-775 (1991).
183. S. L. Jacques, "Optical absorption of melanin," http://omlc.ogi.edu/spectra/melanin/index.html (1998).
184. M. Cope, "The application of near infrared spectroscopy to non invasive monitoring of cerebral oxygenation in the newborn infant," (1991). Ph.D. Thesis, University College London, London, UK.
185. B. Beauvoit, T. Kitai, and B. Chance, "Contribution of the mitochondrial compartment to the optical properties of the rat liver: a theoretical and practical approach," Biophys. J. **67,** 2501-2510 (1994).
186. W. A. Bowes, III, B. C. Corke, and J. Hulka, "Pulse oximetry: A review of the theory, accuracy, and clinical applications," Obstet. Gynecol. **74,** 541-546 (1989).
187. K. K. Tremper and S. J. Barker, "Pulse oximetry," Anesthesiology **70,** 98-108 (1989).
188. M. Ferrari, D. A. Wilson, D. F. Hanley, J. F. Hartmann, M. C. Rogers, and R. J. Traystman, "Noninvasive determination of hemoglobin saturation in dogs by derivative near-infrared spectroscopy," Am. J. Physiol. **256,** H1493-H1499 (1989).
189. E. M. Sevick, B. Chance, J. Leigh, S. Nioka, and M. Maris, "Quantitation of time- and frequency-resolved optical spectra for determination of tissue oxygenation," Anal. Biochem. **195,** 330-351 (1991).
190. B. C. Wilson, E. M. Sevick, M. S. Patterson, and B. Chance, "Time-dependent optical spectroscopy and imaging for biomedical applications," Proc. IEEE **80,** 918-930 (1992).
191. S. Fantini, M. A. Franceschini-Fantini, J. S. Maier, S. A. Walker, B. Barbieri, and E. Gratton, "Frequency-domain multichannel optical detector for noninvasive tissue spectroscopy and oximetry," Opt. Eng. **34,** 32-42 (1995).
192. J. B. Fishkin, O. Coquoz, E. R. Anderson, M. Brenner, and B. J. Tromberg, "Frequency-domain photon migration measurements of normal and malignant tissue optical properties in a human subject," Appl. Opt. **36,** 10-20 (1997).
193. R. Cubeddu, A. Pifferi, P. Taroni, A. Torricelli, and G. Valentini, "Compact tissue oximeter based on dual-wavelength multichannel time-resolved reflectance," Appl. Opt. **38,** 3670-3680 (1999).
194. S. J. Matcher and C. E. Cooper, "Absolute quantification of deoxyhaemoglobin concentration in tissue near infrared spectroscopy," Phys. Med. Biol. **39,** 1295-1312 (1994).
195. B. Chance, "Near-infrared images using continuous, phase-modulated, and pulsed light with quantitation of blood and blood oxygenation.," Ann. N. Y. Acad. Sci. **838,** 29-45 (1998).
196. T. H. Pham, R. Hornung, H. P. Ha, T. Burney, D. Serna, L. Powell, M. Brenner, and B. J. Tromberg, "Noninvasive monitoring of hemodynamic stress using quantitative near-infrared frequency-domain photon migration spectroscopy," J Biomed Opt **7,** 34-44 (2002).
197. E. L. Heffer and S. Fantini, "Novel approach to quantitative oximetry of breast lesions using two *ad hoc* near-infrared wavelengths," in *OSA Biomedical Topical Meetings, OSA Technical Digest,* Proc. Optical Society of America, Washington DC OSA, (2002) pp. 99-101.
198. E. M. C. Hillman, S. R. Arridge, J. C. Hebden, and D. Delpy, "Oxygen saturation and blood-volume derivation from multi-wavelength time-resolved optical tomography data," in *OSA Biomedical Topical Meetings, OSA Technical Digest,* Proc. Optical Society of America, Washington DC OSA, (2002) pp. 599-601.

199. L. O. Svaasand, E. J. Fiskerstrand, G. Kopstad, L. T. Norvang, E. K. Svaasand, J. S. Nelson, and M. W. Berns, "Therapeutic response during pulsed laser treatment of port-wine stains: dependence on vessel diameter and depth in dermis," Lasers Med. Sci. **10,** 235-243 (1995).
200. W. Verkruysse, G. W. Lucassen, J. F. de Boer, D. J. Smithies, J. S. Nelson, and M. J. C. van Gemert, "Modelling light distributions of homogeneous versus discrete absorbers in light irradiated turbid media," Phys. Med. Biol. **42,** 51-65 (1997).
201. M. Firbank, E. Okada, and D. T. Delpy, "Investigation of the effect of discrete absorbers upon the measurement of blood volume with near-infrared spectroscopy," Phys. Med. Biol. **42,** 465-477 (1997).
202. A. Talsma, B. Chance, and R. Graaff, "Corrections for inhomogeneities in biological tissue caused by blood vessels," J. Opt. Soc. Am. A **18,** 932-939 (2001).
203. R. A. Meyer, "Light scattering from red blood cell ghosts: sensitivity of angular dependent structure to membrane thickness and refractive index," Appl. Opt. **16,** 2036-2038 (1977).
204. J. C. Lin and A. W. Guy, "A note on the optical scattering characteristics of whole blood," IEEE Trans. Biomed. Eng. **21,** 43-45 (1974).
205. G. J. Streekstra, A. G. Hoekstra, E.-J. Nijhof, and R. M. Heethaar, "Light scattering by red blood cells in ektacytometry: Fraunhofer versus anomalous diffraction," Appl. Opt. **32,** 2266-2272 (1993).
206. E. Evans and Y.-C. Fung, "Improved measurements of the erythrocyte geometry," Microvasc. Res. **4,** 335-347 (1972).
207. R. H. Phibbs and A. C. Burton, "Orientation and distribution of erythrocytes in blood flowing through medium-sized arteries," in *Hemorheology: Proceedings of the first international conference,* A. L. Copely (ed.), Proc. Pergamon Press Ltd., New York, 1968), pp. 617-632.
208. J. Goldstone, H. Schmid-Schönbein, and R. Wells, "The rheology of red blood cell aggregates," Microvasc. Res. **2,** 273-286 (1970).
209. H. L. Goldsmith and J. C. Marlow, "Flow behavior of erythrocytes II. Particle motions in concentrated suspensions of ghost cells," J. of Colloid and Interface Science **71,** 383-407 (1979).
210. H. Schmid-Schönbein and R. Wells, "Fluid drop-like transition of erythrocytes under shear," Science **165,** 288-291 (1969).
211. H. J. Klose, E. Volger, H. Brechtelsbauer, L. Heinich, and H. Schmid-Schönbein, "Microrheology and light transmission of blood. I. The photometric effects of red cell aggregation and red cell orientation," Pflügers Arch. **333,** 126-139 (1972).
212. H. Schmid-Schönbein, E. Volger, and H. J. Klose, "Microrheology and light transmission of blood. II. The photometric quantification of red cell aggregate formation and dispersion in flow," Pflügers Arch. **333,** 140-155 (1972).
213. P. L. Blackshear, R. J. Forstrom, F. D. Dorman, and G. O. Voss, "Effect of flow on cells near walls," Fed. Proc. **30,** 1600-1611 (1971).
214. H. L. Goldsmith, "Red cell motions and wall interactions in tube flow," Fed. Proc. **30,** 1578-1590 (1971).
215. M. D. Waterworth, B. J. Tarte, A. J. Joblin, T. van Doorn, and H. E. Niesler, "Optical transmission properties of homogenised milk used as a phantom material in visible wavelength imaging," Australasian Phys. Eng. Sci. Med. **18,** 39-44 (1995).
216. H. J. van Staveren, C. J. M. Moes, J. van Marle, S. A. Prahl, and M. J. C. van Gemert, "Light scattering in Intralipid-10 % in the wavelength range of 400-1100 nm," Appl. Opt. **30,** 4507-4514 (1991).
217. S. T. Flock, S. L. Jacques, B. C. Wilson, W. M. Star, and M. J. C. van Gemert, "Optical properties of Intralipid: A phantom medium for light propagation studies," Lasers Surg. Med. **12,** 510-519 (1992).

218. G. Wagnieres, S. Cheng, M. Zellweger, N. Utke, D. Braichotte, J. P. Ballini, and B. H. van den, "An optical phantom with tissue-like properties in the visible for use in PDT and fluorescence spectroscopy," Phys. Med. Biol. **42,** 1415-1426 (1997).
219. R. Cubeddu, A. Pifferi, P. Taroni, A. Torricelli, and G. Valentini, "A solid tissue phantom for photon migration studies," Phys. Med. Biol. **42,** 1971-1979 (1997).
220. S. J. Madsen, M. S. Patterson, and B. C. Wilson, "The use of india ink as an optical absorber in tissue-simulating phantoms," Phys. Med. Biol. **37,** 985-993 (1992).
221. M. Firbank and D. T. Delpy, "A design for a stable and reproducible phantom for use in near infra-red imaging and spectroscopy," Phys. Med. Biol. **38,** 847-853 (1993).
222. M. Firbank, M. Oda, and D. T. Delpy, "An improved design for a stable and reproducable phantom material for use in near-infrared spectroscopy and imaging," Phys. Med. Biol. **40,** 955-961 (1995).
223. U. Brackmann, *Lambdachrome laser dyes*, (Lambda Physik AG, Göttingen, 2000).
224. "American Dye Source, Inc.," http://www.adsdyes.com/ (2002).
225. B. C. Wilson, T. J. Farrell, and M. S. Patterson, "An optical fiber-based diffuse reflectance spectrometer for non-invasive investigation of photodynamic sensitizers in vivo," Proc. SPIE **IS-6**, (Soc. Photo-Opt. Instrum. Eng., 1990), pp. 219-232.
226. F. Bevilacqua, D. J. Cuccia, A. J. Durkin, and B. J. Tromberg, "Quantitative analysis and imaging of subsurface heterogeneities using spatially structured illumination," in *OSA Biomedical Topical Meetings, OSA Technical Digest,* Proc. Optical Society of America, Washington DC OSA, (2002) pp. 677-679.
227. J. J. Stott and D. A. Boas, "A practical comparison between time-domain and frequency-domain diffusive optical imaging systems," in *OSA Biomedical Topical Meetings, OSA Technical Digest,* Proc. Optical Society of America, Washington DC OSA, (2002) pp. 626-628.
228. T. I. Meresolv, E. Reciproca, E. Spcz, "On Low-Virtual Endomyonic Detection Reversing Under Light," Eng. Sci. SPC300, 660 - 785 (2002).
229. S. Fantini, D. Hueber, M. A. Franceschini, E. Gratton, W. Rosenfeld, P. G. Stubblefield, D. Maulik, and M. R. Stankovic, "Non-invasive optical monitoring of the newborn piglet brain using continuous-wave and frequency-domain spectroscopy," Phys. Med. Biol. **44,** 1543-1563 (1999).
230. F. Bevilacqua, A. J. Berger, A. E. Cerussi, D. Jakubowski, and B. J. Tromberg, "Broadband absorption spectroscopy in turbid media by combined frequency-domain and steady-state methods," Appl. Opt. **39,** 6498-6507 (2000).
231. T. J. Brukilacchio, Q. Zhang, J. J. Stott, A. Li, D. A. Boas, T. Wu, R. H. Moore, and D. B. Kopans, "Instrumentation for imaging of breast lesions based on co-registered diffuse optical and X-ray tomography," in *OSA Biomedical Topical Meetings, OSA Technical Digest,* Proc. Optical Society of America, Washington DC OSA, (2002) pp. 178-180.
232. G. Yu, T. Durduran, D. Furuya, R. Choe, J. H. Greenberg, and A. G. Yodh, "Frequency domain diffuse optical multiplexing system for rapid hemodynamics," in *OSA Biomedical Topical Meetings, OSA Technical Digest,* Proc. Optical Society of America, Washington DC OSA, (2002) pp. 184-186.
233. S. Jiang, B. W. Pogue, T. O. McBride, and K. D. Paulsen, "Dynamic hemoglobin concentration imaging using a simultaneous two wavelength near-infrared diffuse optical tomography system," in *OSA Biomedical Topical Meetings, OSA Technical Digest,* Proc. Optical Society of America, Washington DC OSA, (2002) pp. 190-192.
234. I. Nissilä, K. Kotilahti, T. Noponen, and T. Katila, "A method for the measurement of phase with high accuracy in intensity modulated optical imaging," in *OSA Biomedical Topical Meetings, OSA Technical Digest,* Proc. Optical Society of America, Washington DC OSA, (2002) pp. 683-685.

235. P. P. Ho, P. Baldeck, K. S. Wong, K. M. Yoo, D. Lee, and R. R. Alfano, "Time dynamics of photon migration in semiopaque random media," Appl. Opt. **28,** 2304-2304 (1989).
236. S. Andersson-Engels, R. Berg, O. Jarlman, and S. Svanberg, "Time-resolved transillumination for medical diagnostics," Opt. Lett. **15,** 1179-1181 (1990).
237. J. C. Hebden, M. Tziraki, and D. Delpy, "Evaluation of the temporally extrapolated absorbance method for dual-wavelength imaging through tissuelike scattering media," Appl. Opt. **36,** 3802-3810 (1997).
238. F. E. Schmidt, M. E. Fry, E. M. C. Hillman, J. C. Hebden, and D. T. Delpy, "A 32-channel time-resolved instrument for medical optical tomography," Rev. Sci. Instrum. **71,** 256-265 (2000).
239. J. C. Hebden, S. R. Arridge, and D. T. Delpy, "Optical imaging in medicine: I. Experimental techniques," Phys. Med. Biol. **42,** 825-840 (1997).
240. S. Svanberg, *Atomic and Molecular Spectroscopy – Basic Aspects and Practical Applications*, (Springer Verlag, Heidelberg, Germany, 2001).
241. "Data sheet for SPC-300, Becker & Hickl GmbH," http://www.becker-hickl.de/ (2000).
242. "Technical data sheet, Hamamatsu Photonics K.K.," http://usa.hamamatsu.com/ (2002).
243. G. N. Gol'tsman, O. Okunev, G. Chulkova, A. Lipatov, A. Semenov, K. Smirnov, B. Voronov, A. Dzardanov, C. Williams, and R. Sobolewski, "Picosecond superconducting single-photon optical detector," Appl. Phys. Lett. **79,** 705-707 (2001).
244. A. Verevkin, J. Zhang, R. Sobolewski, A. Lipatov, O. Okunev, G. Chulkova, A. Korneev, K. Smirnov, G. N. Gol'tsman, and A. Semenov, "Detection efficiency of large-active-area NbN single-photon superconducting detectors in the ultraviolet to near-infrared range," Appl. Phys. Lett. **80,** 4687-4689 (2002).
245. J. C. Hebden, R. A. Kruger, and K. S. Wong, "Time resolved imaging through a highly scattering medium," Appl. Opt. **30,** 788-794 (1991).
246. C. af Klinteberg, R. Berg, C. Lindquist, S. Andersson-Engels, and S. Svanberg, "Diffusely scattered femtosecond white light examination of breast tissue *in vitro* and *in vivo*," in *Photon Propagation in Tissues,* B. Chance, D. T. Delpy, and G. J. Müller (eds.), Proc. SPIE **2626**, (Soc. Photo-Opt. Instrum. Eng., Bellingham, WA., 1995), pp. 149-157.
247. C. D'Andrea, D. Comelli, G. Valentini, and R. Cubeddu, "Time-domain transmittance imaging in turbid media using an intensified CCD camera," in *Photon Migration, Optical Coherence Tomography, and Microscopy,* S. Andersson-Engels and M. F. Kaschke (eds.), Proc. SPIE **4431**, (Soc. Photo-Opt. Instrum. Eng., Bellingham, WA, 2001), pp. 255-259.
248. S. B. Colak, M. B. van der Mark, G. W. 't Hooft, J. H. Hoogenraad, E. S. van der Linden, and F. A. Kuijpers, "Clinical optical tomography and NIR spectroscopy for breast cancer detection," IEEE Journal of Selected Topics in Quantum Electronics **5,** 1143-1158 (1999).
249. C. H. Schmitz, M. Locker, J. M. Lasker, A. H. Hielscher, and R. L. Barbour, "Instrumentation for fast functional optical tomography," Rev. Sci. Instrum. **73,** 429-439 (2002).
250. A. M. Siegel, J. J. A. Marota, and D. A. Boas, "Design and evaluation of a continuous-wave diffuse optical tomography system," Optics Express **4,** 287-298 (1999).
251. E. Gratton, W. W. Mantulin, M. J. vandeVen, J. Fishkin, M. B. Maris, and B. Chance, "A novel approach to laser tomography," Bioimaging **1,** 40-46 (1993).
252. M. Kaschke, H. Jess, G. Gaida, J.-M. Kaltenbach, and W. Wrobel, "Transillumination imaging of tissue by phase modulation techniques," in *Advances in Optical Imaging and Photon Migration,* R. R. Alfano (ed.), Proc. OSA **21**, (Optical Society of America, Washington, DC, USA, 1994), pp. 88-92.
253. H. Jess, H. Erdl, K. T. Moesta, S. Fantini, M. A. Franceschini, E. Gratton, and M. Kaschke, "Intensity modulated breast imaging: technology and clinical pilot study results," in *OSA Trends in Optics and Photonics on Advances in Optical Imaging and Photon Migration,* R. R. Alfano and J. G. Fujimoto (eds.), Proc. Optical Society of America, Washigton DC OSA, (1996) pp. 126-129.

254. B. Wolfgang, A. Bergmann, H. Wabnitz, D. Grosenick, and A. Liebert, "High count rate multichannel TCSPC for optical tomography," in *Proceedings of the SPIE,* Proc. SPIE **4431**, (2001), pp. 249-254.
255. J. C. Hebden, E. M. C. Hillman, A. Gibson, N. Everdell, R. Md. Yusof, and D. Delpy, "Time resolved optical imaging of the newborn infant brain: initial clinical results," in *OSA Biomedical Topical Meetings, OSA Technical Digest,* Proc. Optical Society of America, Washington DC OSA, (2002) pp. 587-589.
256. J. C. Hebden, T. Bland, E. M. C. Hillman, A. Gibson, N. Everdell, and D. Delpy, "Optical tomography of the breast using a 32-channel time-resolved imager," in *OSA Biomedical Topical Meetings, OSA Technical Digest,* Proc. Optical Society of America, Washington DC OSA, (2002) pp. 187-189.
257. F. E. W. Schmidt, J. C. Hebden, E. M. C. Hillman, M. E. Fry, M. Schweiger, H. Dehghani, and D. T. Delpy, "Multiple-slice imaging of a tissue-equivalent phantom by use of time-resolved optical tomography," Appl. Opt. **39,** 3380-3387 (2000).
258. V. Ntziachristos, X. H. Ma, A. G. Yodh, and B. Chance, "Multichannel photon counting instrument for spatially resolved near infrared spectroscopy," Rev. Sci. Instrum. **10,** 193-201 (1999).
259. V. Ntziachristos, X. H. Ma, and B. Chance, "Time-correlated single photon counting imager for simultaneous magnetic resonance and near-infrared mammography," Rev. Sci. Instrum. **69,** 4221-4233 (1998).
260. O. Jarlman, "Diagnostic transillumination of the breast," (1991). M.D. Thesis, Department of Diagnostic Radiology, Lund University Hospital, Lund, Sweden.
261. D. Grosenick, H. Wabnitz, R. Macdonald, H. Rinneberg, J. Mucke, C. Stroszczynski, K. T. Moesta, and P. Schlag, "Determination of *in vivo* optical properties of breast tissue and tumors using a laser pulse mammograph," in *OSA Biomedical Topical Meetings, OSA Technical Digest,* Proc. Optical Society of America, Washington DC OSA, (2002) pp. 459-461.
262. R. L. Barbour, C. H. Schmitz, and H. L. Graber, "Dynamic functional imaging of the healthy and cancerous breast by optical tomography," in *OSA Biomedical Topical Meetings, OSA Technical Digest,* Proc. Optical Society of America, Washington DC OSA, (2002) pp. 456-458.
263. R. Choe, T. Durduran, J. P. Culver, L. Zubkov, J. M. Giammarco, X. Intes, B. Chance, and A. G. Yodh, "Bulk optical properties of normal breast with endogeneous and exogeneous contrast," Proc. Optical Society of America, Washington DC OSA, (2002) pp. 462-464.
264. X. Gu, N. Iftimia, Y. Xu, H. Jiang, and L. F. Fajardo, "A compact, parallel-detection diffuse optical tomography system: continued clinical studies," in *OSA Biomedical Topical Meetings, OSA Technical Digest,* Proc. Optical Society of America, Washington DC OSA, (2002) pp. 468-469.
265. N. Shah, A. Cerussi, D. Jakubowski, R. Lanning, and B. J. Tromberg, "Spatial variations in optical and physiological properties of healthy breast tissue," in *OSA Biomedical Topical Meetings, OSA Technical Digest,* Proc. Optical Society of America, Washington DC OSA, (2002) pp. 470-472.
266. B. W. Pogue, W. A. Wells, S. Jiang, S. P. Poplack, T. D. Tosteson, and K. D. Paulsen, "Validation of hemoglobin concentration imaging of breast tumors through comparison with pathological assessment," in *OSA Biomedical Topical Meetings, OSA Technical Digest,* Proc. Optical Society of America, Washington DC OSA, (2002) pp. 473-475.
267. V. E. Pera, E. L. Heffer, O. Schütz, H. Siebold, S. Heywang-Köbrunner, L. Götz, A. Heinig, and S. Fantini, "Second-derivative optical mammography," in *OSA Biomedical Topical Meetings, OSA Technical Digest,* Proc. Optical Society of America, Washington DC OSA, (2002) pp. 671-673.
268. "Imaging Diagnostic Systems, Inc," http://www.imds.com/ (2002).

269. H. Edner, P. Ragnarson, S. Spännare, and S. Svanberg, "A differential optical absorption spectroscopy (DOAS) system for urban atmospheric pollution monitoring," Appl. Opt. **32,** 327 (1993).
270. M. M. Millan and R. M. Hoff, "Remote sensing of air pollutants by correlation spectroscopy - instrumental response characteristics," Atmospheric Environment **12,** 853-864 (1978).
271. H. Edner, K. Fredriksson, A. Sunesson, S. Svanberg, L. Unéus, and W. Wendt, "Mobile remote sensing system for atmospheric monitoring," Appl. Opt. **26,** 4330 (1987).
272. M. Nicolet, "On the molecular scattering in the terrestrial atmosphere: an empirical formula for its calculation in the homosphere," Planetary and Space Science **32,** 1467-1468 (1984).
273. "International standard atmosphere," http://www.aeromech.usyd.edu.au/aero/atmos/atmos.html (2002).
274. E. M. Patterson and J. B. Gillespie, "Simplified ultraviolet and visible wavelength atmospheric propagation model," Appl. Opt. **28,** 425-429 (1989).
275. M. M. Millan, "Remote sensing of air pollutants. A study of some atmospheric scattering effects," Atmospheric Envir. **14,** 1241-1253 (1980).
276. R. J. Charlson and J. Heintzenberg, eds., "Aerosol forcing of climate," (John Wiley & Sons, Chichester, 1995).